

Electrical Impedance Tomography for Deformable Media

Camille Gómez-Laberge

A thesis submitted to the
Faculty of Graduate and Postdoctoral Studies
In partial fulfilment of the requirements
For the M.A.Sc. degree in Electrical Engineering

Ottawa-Carleton Institute for Electrical and Computer Engineering
School of Information Technology and Engineering
University of Ottawa

© Camille Gómez-Laberge, Ottawa, Canada, 2006

To my parents

The undersigned hereby recommends to
the faculty of Graduate Studies and Research
acceptance of this thesis,

**Electrical Impedance Tomography
for Deformable Media**

Submitted by
Camille Gómez-Laberge

In partial fulfillment of
the requirements for the degree of
Master of Applied Science
in
Electrical Engineering

Andy Adler, Ph.D.
(Thesis Supervisor)

Acknowledgements

My utmost gratitude and appreciation are extended to my supervisor, Dr. Andy Adler, for his judicious advice concerning scientific research, admirable availability, and generous financial support. I am also obliged for his genuine encouragement, inspiring creativity and objective criticism in my residence under his supervision.

I would also like to thank my colleagues at the University of Ottawa, Tao Dai, Richard Youmaran, Yednekachew Asfaw, Tatyana Dembinsky and Li Peng Xie for their resourceful suggestions and their energetic motivation. My M.A.Sc. experience is a memorable and happy one because of them. My special thanks are expressed to Li Peng for his assistance in experimental work and Tatyana for her kindness in proofreading this thesis.

Finally, I dedicate this thesis to my loving parents, who have privileged me with unconditional support, encouragement and enthusiasm in each of my endeavours. I reserve my deepest sentiments for them.

Camille Gómez-Laberge

August, 2006
Ottawa, Canada

Abstract

In Electrical Impedance Tomography (EIT), electrical energy is applied and measured at the boundary of a medium to produce an image of its internal conductivity distribution. When imaging pulmonary ventilation, rib cage expansion and body posture introduce severe image artefacts in the reconstructed images due to electrode position error.

This thesis proposes a method to reduce such artefacts by determining the net displacement of electrodes between measurement frames, and effectively, adjusting the geometry of the reconstruction model. A novel regularization method is proposed and validated using data acquired from simulation, phantom, and human *in vivo* measurements.

The proposed method reduces artefacts by more than 70% in simulated reconstructions and phantom experiments. The *in vivo* images reveal the various breathing manoeuvres and thoracic movements recorded.

Furthermore, the displacement of each electrode is calculated, indicating the deformed boundary shape. This thesis supports EIT for clinical diagnostics and monitoring of pulmonary ventilation.

Contents

Acknowledgements	iv
Abstract	v
Contents	vi
List of Figures	ix
List of Acronymns	xi
List of Symbols	xii
1 Introduction	1
1.1 Medical Imaging Applications	2
1.2 Thesis Objectives	3
1.3 Thesis Contributions	4
2 Background	6
2.1 Electrical Properties of Human Physiology	6
2.2 Electrical Impedance Tomography	10
2.3 Medical Applications of EIT	13
3 Inverse Problem Theory	17
3.1 Notations and Definitions	17
3.2 Statistical Inversion	21

3.3	Discrete Regularization Methods	25
4	Electrical Impedance Tomography	30
4.1	The EIT Inverse Problem	30
4.2	Finite Element Method	33
4.2.1	The Forward Problem	34
4.2.2	The Inverse Problem	35
4.3	MAP Image Reconstruction Algorithm	38
5	Image Variability from Boundary Deformation	43
5.1	Cause and Effect of Boundary Deformation	43
5.2	Simulation Methods	44
5.2.1	Forward and Inverse Models	44
5.2.2	Boundary Deformation and Electrode Displacement	46
5.2.3	Analysis of Conductivity Variability	47
5.3	Image Reconstructions	48
5.4	Discussion	51
6	Electrode Displacement Regularization	54
6.1	Electrode Displacement MAP Algorithm	54
6.1.1	System model	55
6.1.2	Forward calculations	56
6.1.3	Inverse calculations	57
6.1.4	Artefact amplitude measure	62
6.2	Performance Analysis	62
6.3	Discussion	65
7	Imaging of Deformable Media	69
7.1	Acquired EIT Data	69
7.2	Reconstructed Conductivity Images	72

7.2.1	Simulated Reconstructions	72
7.2.2	Phantom Reconstructions	76
7.2.3	In Vivo Reconstructions	78
7.3	Discussion	81
8	Conclusion	88
8.1	EIT for Deformable Media	89
8.2	Future Directions	90
	Bibliography	92
A	Data Acquisition Records	97
A.1	Phantom Experiment	97
A.2	In Vivo Experiment	101
B	Underdamped Reconstruction Artefact	104
C	Software Code	107
C.1	Electrode Displacement	107
C.2	Performance Analysis	113
C.3	Artefact Analysis	118

List of Figures

2.1	Let-go current	8
2.2	EIT block diagram	10
2.3	Linear basis functions	13
2.4	Lung perfusion imaging	14
2.5	Stroke volume estimation	15
2.6	Encephalographic imaging	16
3.1	Abstract inverse problem	18
3.2	Radon transform diagram	19
3.3	Example of the Radon transform	20
3.4	Singular value spectrum of the Radon transform example	28
3.5	Regularized Radon transform example	29
4.1	FEM meshes	34
4.2	EIT system matrix sparse plot	36
4.3	EIT Jacobian matrix singular value spectrum	37
4.4	Wiener filter block diagram	40
5.1	Variability simulation using same boundary	45
5.2	Variability simulation using circular boundary	48
5.3	Variability simulation with two displaced electrodes	49
5.4	Variability simulation with left-right displacements	50
5.5	Variability simulation with anterior-posterior displacements	51

5.6	Conductivity variation plot	52
6.1	Illustration of the implementation of the R and J matrices.	61
6.2	Blur radius plotted versus hyperparameter λ	64
6.3	AAM plotted versus boundary deformation	65
6.4	AAM gain factor plotted versus boundary deformation	66
7.1	Saline phantom	71
7.2	Simulated 2D image reconstructions	73
7.3	3D FEM simulation model	74
7.4	Simulated 3D image reconstructions	75
7.5	Phantom 2D image reconstruction	76
7.6	Phantom simulation of breathing reconstructions	77
7.7	<i>In vivo</i> tidal breathing in rest state	79
7.8	<i>In vivo</i> tidal breathing in stress state	80
7.9	<i>In vivo</i> TLC/RC breathing in rest state	82
7.10	<i>In vivo</i> TLC/RC breathing in stress state	83
7.11	<i>In vivo</i> paradoxical breathing in rest state	84
7.12	<i>In vivo</i> paradoxical breathing in stress state	85
B.1	Underdamped artefact	105
B.2	Fitting the underdamped artefact to a second order function	105
B.3	Plot of the fitted second order function parameters	106

List of Acronyms

AAM	Artefact Amplitude Measure
AMD	Advanced Micro Devices
AWGN	Additive White Gaussian Noise
CEM	Complete Electrode Model
CM	Conditional Mean
CT	Computed Tomography
ECG/EKG	Electrocardiograph
EIDORS	Electrical Impedance and Diffuse Optics Reconstruction Software
EIT	Electrical Impedance Tomography
FEM	Finite Element Method
fMRI	functional Magnetic Resonance Imaging
GNU	GNU's Not UNIX
IEEE	Institute of Electrical and Electronics Engineers
MAP	<i>Maximum A Posteriori</i>
MRI	Magnetic Resonance Imaging
PEM	Point Electrode Model
PET	Positron Emission Tomography
PSF	Point Spread Function
SNR	Signal to Noise Ratio
SPECT	Single Photon Emission Computed Tomography
SVD	Singular Value Decomposition
TLC/RC	Total Lung Capacity / Residual Capacity

List of Symbols

A	system matrix
\mathbf{B}	magnetic flux density field
d	observation data
\mathbf{D}	electric displacement field
\mathfrak{D}	observation manifold
\mathcal{D}	observation manifold point
E_j	electrode j
\mathbf{E}	electric field
G	forward operator
G^{-1}	inverse operator
\mathbf{H}	magnetic field
I	excitation current
J	Jacobian matrix
J_E	electrode displacement Jacobian matrix
J_σ	conductivity Jacobian matrix
\mathbf{J}	current density field
m	model parameter
\mathfrak{M}	model manifold
\mathcal{M}	model manifold point
n	noise vector
N_d	number of spatial dimensions
N_e	number of electrodes
N'_e	number of electrodes per ring
N_k	number of elements
N_p	number of nodes
N_r	number of rings
N_v	number of independent measurements

\mathbf{r}	position vector
R	<i>a priori</i> image matrix
R_E	<i>a priori</i> electrode displacement matrix
R_σ	<i>a priori</i> conductivity matrix
\mathbf{v}	difference voltage measurement data
\mathbf{v}_h	homogeneous difference voltage measurement
V	voltage measurement data
w_E	<i>a priori</i> electrode displacement amplitude
w_σ	<i>a priori</i> conductivity amplitude
W	<i>a priori</i> noise matrix
x_{MAP}	<i>maximum a posteriori</i> image estimate
x_λ	Tikhonov regularized solution
\mathbf{x}	conductivity-displacement image
$\mathbf{x}_{\lambda\mu}$	conductivity-displacement regularized image
z	contact impedance
γ	admittivity distribution
$\Delta\sigma$	conductivity change image
ζ	damping ratio
η	normal vector
$\kappa(A)$	condition number
λ	Tikhonov hyperparameter
μ	electrode displacement hyperparameter
σ	conductivity distribution
σ_h	homogeneous conductivity distribution
Σ_σ	conductivity covariance matrix
Σ_n	noise covariance matrix
ϕ	electric potential
ω_n	natural frequency
Ω	medium space
$\partial\Omega$	medium boundary

Chapter 1

Introduction

Since the invention of the photograph, images have been employed to capture fractions of reality in countless forms. Our interpretation of the physical world is mostly determined by what we see around us. Consequently, one could say that imagery is the richest source of information available to our senses. Science and medicine of the twenty-first century use exotic forms of image acquisition to explore the frontiers of our known universe and to confirm postulates that until today were only conceivable by the mind's eye. The welfare of human health in particular is perhaps the largest beneficiary of imagery since today, non-invasive methods allow the physician to visualize fundamental mechanisms of the body that are otherwise inaccessible.

A clearer understanding of the anatomy and function of our organism has improved clinical diagnosis, disease prevention, and surgery efficacy—overall enhancing our quality of life. However, this enlightenment has also unravelled the discovery of new phenomena, suggesting an ever-more elaborate design of the human body. Thus, persistent efforts stimulate the research and development of new tools, pacing forwards to reveal the portrait that nature has set before us.

1.1 Medical Imaging Applications

Modern applications of medical imaging are typically categorized as *modalities*, each of which provide distinct information about the body being observed. All modalities, however, adhere to the concept that the observed body is imaged by measuring the body's response to some form of energy. For example, in photography, light is reflected on the object, focused by the camera lens, and captured by the photo-sensitive film or CCD array.

One of the oldest modalities in practice today is the radiograph, which uses emitted 20-150 keV X-ray photons that project the body's skeletal structure and denser tissues onto a detector. From this concept, *Computed Tomography* (CT) uses X-rays projected around a single axis of rotation to calculate tomographic images of the body. CT is used to render 3D *anatomical* maps for the diagnosis of many regions of the body. Typical modern performance standards of CT are sub-millimeter resolution and an average 64 slice scan time of 10 seconds.

The dynamics of hydrogen nuclei in water under magnetic fields are useful to image internal living tissues. This is possible by observing the magnetic resonance relaxation process of polarized nuclei subjected to short radio frequency pulses. This modality was originally named Nuclear Magnetic Resonance; however, it is typically called *Magnetic Resonance Imaging* (MRI) due to the negative connotations with the word "Nuclear". MRI also renders 3D anatomical maps, sensitive to different tissues and is capable of higher contrast resolution than CT. An adapted *functional* imager called fMRI is capable of imaging perfusion and diffusion of fluids, indirectly providing images of brain activity. The modern MRI instrument operates over 1-3 Tesla magnetic flux density fields, with 3 mm resolution at an average 8 minute full body scan time.

Other nuclear phenomena have also lead to useful functional modalities that image radioisotope-labelled nutrients consumed in metabolic processes of the body. *Single Photon Emission Computed Tomography* (SPECT) and *Positron Emission Tomography* (PET) track decaying isotopes to visualize the level of energy consumed by tissues. For example, PET radioactive isotopes emit positrons e^+ that eventually annihilate with electrons in the body. The annihilation produces two oppositely propagating high energy photons that exit the

body and are captured by an event detector. Unfortunately, only small doses of radioactive material can be administered to limit patient exposure. In addition, fundamental physical limits and very short flight times of emitted photons result in almost centimeter resolution. Nonetheless, SPECT and PET are useful in oncology diagnostics and in assessing myocardium viability in the treatment of coronary artery disease.

The focus of this thesis is a recent modality based on the propagative nature of electrical current through a conductive medium. *Electrical Impedance Tomography* (EIT) refers to medical instrumentation that images the conductivity distribution of a body using electrical measurements made on the boundary. Analogous to CT, a sequence of excitation currents is introduced *via* surface electrodes placed along the body perimeter. For each excitation current, electric potential measurements are made on the surface and are used to reconstruct the internal conductivity distribution satisfying those data. Thus, modern EIT instruments are capable of monitoring flow and perfusion of internal fluids with a relatively fast temporal resolution of on average 10 frames per second (Frerichs, 2000). The spatial resolution is, however, low and on average can be estimated at 12% of the medium diameter (Metherall, 1998). Similar to fMRI or PET, EIT is considered a functional modality since the movement of bodily fluids is indicative of physiological function. EIT is useful in cardiopulmonary, encephalographic, and mammography diagnostic imaging.

Pioneer EIT implementations are accredited to David C. Barber and Brian H. Brown of the United Kingdom in the late 1970's (Barber & Brown, 1998). EIT is currently in the late experimental stage as its challenges reside mostly in non-linear modelling and inverse problems. Researchers in the United Kingdom, South Korea, the United States, Finland, Germany and Canada are active in the development EIT.

1.2 Thesis Objectives

One major complication of EIT is the significant degradation of the conductivity image due to changes in boundary shape and electrode position during measurement. Similar to other modalities, EIT incurs artefacts in image reconstruction when patient movement disturbs

the measurement environment. The occurrence of these errors leads to reduced repeatability and reliability in diagnostic imaging, which is unacceptable for clinical use.

Boundary movement occurs mostly in thoracic measurement due to posture change and respiration. The former causes a shifting of the rib cage under the skin, and the latter causes the expansion and contraction. The difficulty arises since EIT measurements are projected onto a geometric reconstruction model that approximates the topology of the body being observed. The displacement of electrodes reduces the accuracy of the reconstruction model, producing misrepresentative images. Related are initial errors from inadequate geometric models and inconsistent electrode placement. These problems are well known in the literature and have been addressed by Adler *et al.* (1996), Blott *et al.* (1998), Lionheart (1998), and Kolehmainen *et al.* (2005).

This thesis synthesizes aspects of the literature pertaining to the fundamentals of EIT and inverse problems. The objective is the assessment of solving the inverse conductivity problem over a deformable boundary and the development of a solution to this problem. Such a solution must then be validated across various types of measurement data and performance ranked with appropriate figures of merit.

1.3 Thesis Contributions

The novel contributions of this thesis are as follows. An adaptable reconstruction model is designed to accommodate boundary deformations and electrode displacement. This deformable boundary model is cast into the regularization scheme to solve the inverse conductivity problem with variable electrode position. The algorithm is applied to 2D and 3D models subjected to boundary deformation using simulation, phantom, and human *in vivo* acquired data. Performance figures of merit are designed to quantify the image resolution, position accuracy, and artefact presence. These measures are compared to a standard reconstruction algorithm that is also subjected to boundary deformation.

These results have been published in one refereed journal from the Institute of Physics on *Physiological Measurement* (Soleimani *et al.*, 2006) , presented in the *Institute of Electri-*

cal and Electronics Engineers (IEEE) proceedings of the *Canadian Conference of Electrical and Computer Engineering* (Gómez-Laberge & Adler, 2006) and at the *International Conference on Biomedical Applications of Electrical Impedance Tomography* (McLeod *et al.*, 2006). The author has collaborated with scientists in the United Kingdom, at the universities of Manchester and Oxford Brookes. Finally, the implementation of these algorithms, with some acquired phantom and human *in vivo* data, have been contributed to the *Electrical Impedance and Diffuse Optics Reconstruction Software* (EIDORS) collaboration (Adler & Lionheart, 2006) under the GNU General Public License.

Chapter 2

Background

A review of topics, that are pertinent to this thesis, is presented here. The general electrical properties of biological tissue and physiology are discussed with a primary concern for safety and, secondly, as a basis for the interpretation of measurement data. The basic concepts of EIT and some commercial instruments are described in terms of hardware and performance. The chapter is closed with a review of recent applications of EIT described in the literature.

2.1 Electrical Properties of Human Physiology

The safety of the person being observed by any medical device is paramount to any clinical study. Unfortunately, safety cannot be considered in absolute terms and the growing use of medical devices results in a growing number of accidents. For example, it is reported that about ten-thousand device-related patient injuries occur in the United States each year (Webster, 1998). The World Health Organization's guide on Medical Device Regulations states that the clinical engineering community believes that at least half of medical device-related injuries and deaths result from user error. Therefore, users must be aware of the intended use and must also be responsible for the maintenance of certified medical devices (WHO, 2003). Secondly, the interpretation of any electrical energy recovered from *in vivo* measurement requires the understanding of the electrical properties of biological tissue and human physiology.

Material	Species	Frequency				
		1 kHz	10 kHz	100 kHz	1 MHz	10 MHz
Brain (grey matter)	B	0.1	0.13	0.15	0.2	0.3
Liver	B	0.04	0.05	0.09	0.2	0.3
Kidney	B	0.12	0.15	0.2	0.3	0.5
Muscle (across)	B	0.3	0.35	0.4	0.5	0.6
Muscle (along)	B	0.5	0.5	0.5	0.6	0.7
Lung (inflated)	B	0.05	0.06	0.08	0.10	0.20
Uterus	H	0.4	0.4	0.4	0.5	0.6
Skin [†]	H	0.0007	0.004	0.06	0.3	0.4
Adipose	H	0.022	0.023	0.023	0.24	0.25

Table 2.1: Conductivity (Sm) of *in vitro* biological tissues at various frequencies. Species B and H refer to Bovine and Human tissues, respectively. [†]From *in vivo* measurements (adapted from Metherall (1998)).

Human biological tissue consists primarily of water. Consequently, the human body can be generally thought of as a conductive medium. Table 2.1, adapted from Metherall (1998), shows *in vitro* conductivity of biological tissues, measured in Siemens (Sm), at various current frequencies. Although some of the tissues used were not human, they had very similar electrical characteristics. Another important observation is that tissues exhibit anisotropic structural and electrical behaviour. For example, table 2.1 shows that skeletal muscle is more conductive along the fibrous structure than perpendicularly to it. This provides the central nervous system an efficient recruitment of myofibrils by propagating action potentials along the conductive fibres. A similar anisotropic conductive material is the myocardium, which propagates current in a specialized way to produce an efficient ejection of blood from the heart into the circulatory system. These mechanisms are regulated by somatic and autonomous processes in the brain that communicate with the body by electrical means. Hence, the body consists of both electrically passive and active tissues. Therefore, any external electrical energy source must, in no way, interfere with these sensitive processes.

The physiological effects of electricity can be deadly within seconds when vital processes are disturbed or irreversibly damaged. The protection mechanism of the body is the low conductivity of the skin, as seen in table 2.1. Nevertheless, once the body becomes part of an electric circuit, several dangerous phenomena can immediately occur (Webster, 1998):

1. unregulated stimulation of active tissues (e.g., the nerves and muscle),

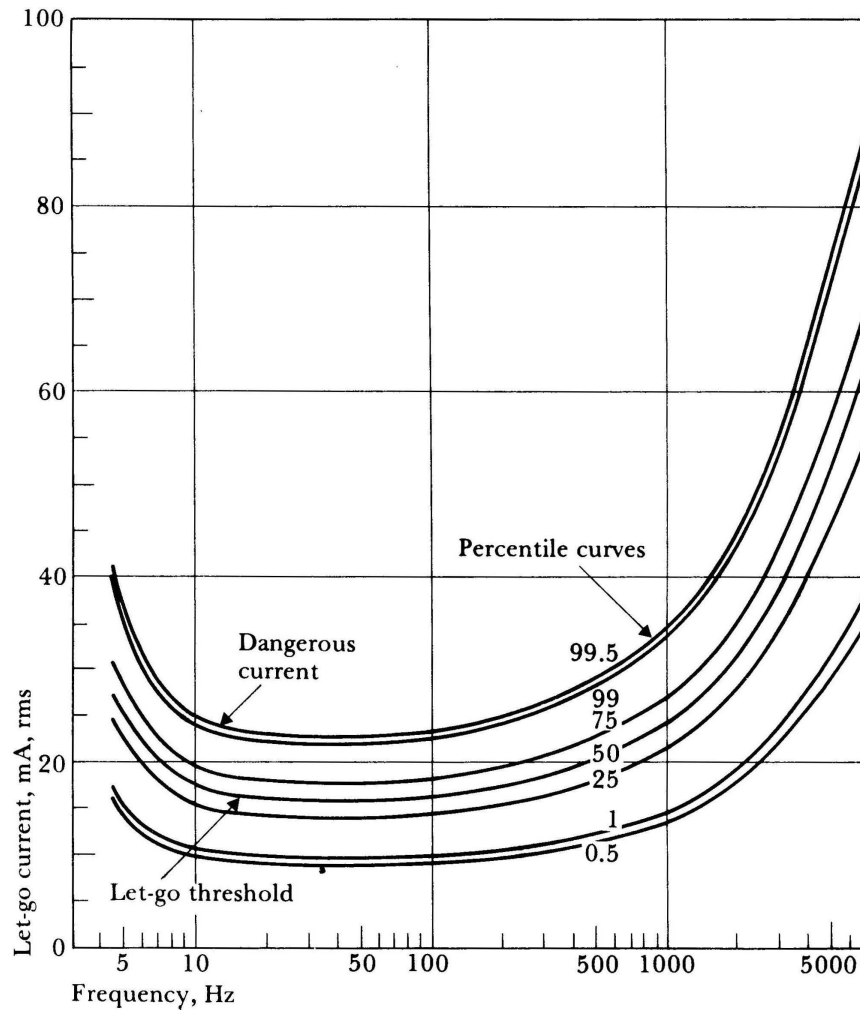


Figure 2.1: Plot of *Let-go* current rms amplitude (mA) versus frequency (log Hz). Percentile values represent the variability of let-go current among individuals (reproduced from Webster (1998)).

2. heating of tissues with high resistance (e.g., the skin), and
3. electrochemical burns and irreversible tissue damage.

The physiological effects worsen with increasing amplitude and frequency of the applied current. Beyond the *threshold of perception*, the victim will experience involuntary contraction of muscles and stimulation of nerves. If the current level is greater than 10 mA, the victim may be incapable of voluntarily breaking the circuit, e.g., by dropping the wire or object relaying the charge. This is referred to as the *let-go current*. At this stage, the victim may also suffer respiratory paralysis, pain, and fatigue. Ventricular fibrillation may occur should

the current path traverse the heart. This can cause death within seconds if the current is not interrupted, and a regular heart beat is not re-initiated. Current levels greater than 1 A cause sustained myocardial contraction, severe burns, and the physical disintegration of nervous tissue and muscle (Webster, 1998). A current level beyond the threshold of perception is considered dangerous in any diagnostic medical device; currents rendering the patient incapable of movement are considered unacceptable (WHO, 2003). Figure 2.1, reproduced from Webster (1998), plots the let-go current root-mean-square (rms) amplitude versus frequency. The percentile values represent the variability of let-go current among individuals.

Medical EIT instruments operate with imperceptible currents on the order of 1–5 mA at frequencies of 15–50 kHz, which are well below the 0.5 percentile curve in figure 2.1. The Goe-MF II EIT instrument (*Viasys Healthcare*, Höchberg, Germany) in this study uses currents of 5 mA (rms) at a frequency of 50 kHz and is certified by the *Conformité Européenne* (CE) as a class IIa active medical device (Viasys Healthcare, 2004). Given the above description of electrical properties and these design specifications, some considerations during data interpretation must be made.

- Tissue exhibits an *anisotropic* conduction of current. Therefore, accurate conductivity images require comprehensive information about the structure and location of all tissue types. This has not been realized in EIT since these data are inaccessible without an accurate anatomical modality.
- Physiological processes manifest electrical activity. Cardiac activity produces body surface potentials in the order of 0.1 mV at 1–10 Hz. Myoelectrical activity produces potentials with the same order of magnitude except at a higher and broader frequency range, 50 Hz–5 kHz. Encephalic signals are smaller, in the order of 25–100 μ V at frequencies of 0.1–100 Hz (Webster, 1998). Hence, EIT equipment requires a narrowband filter to block signals outside the instrument operating frequency. These processes can still introduce variability in the filtered measurements.

Other considerations involve signal interference from power supplies and electronic equipment, and the capacitive effects of the *electrode-skin* interface. In general, commercialized

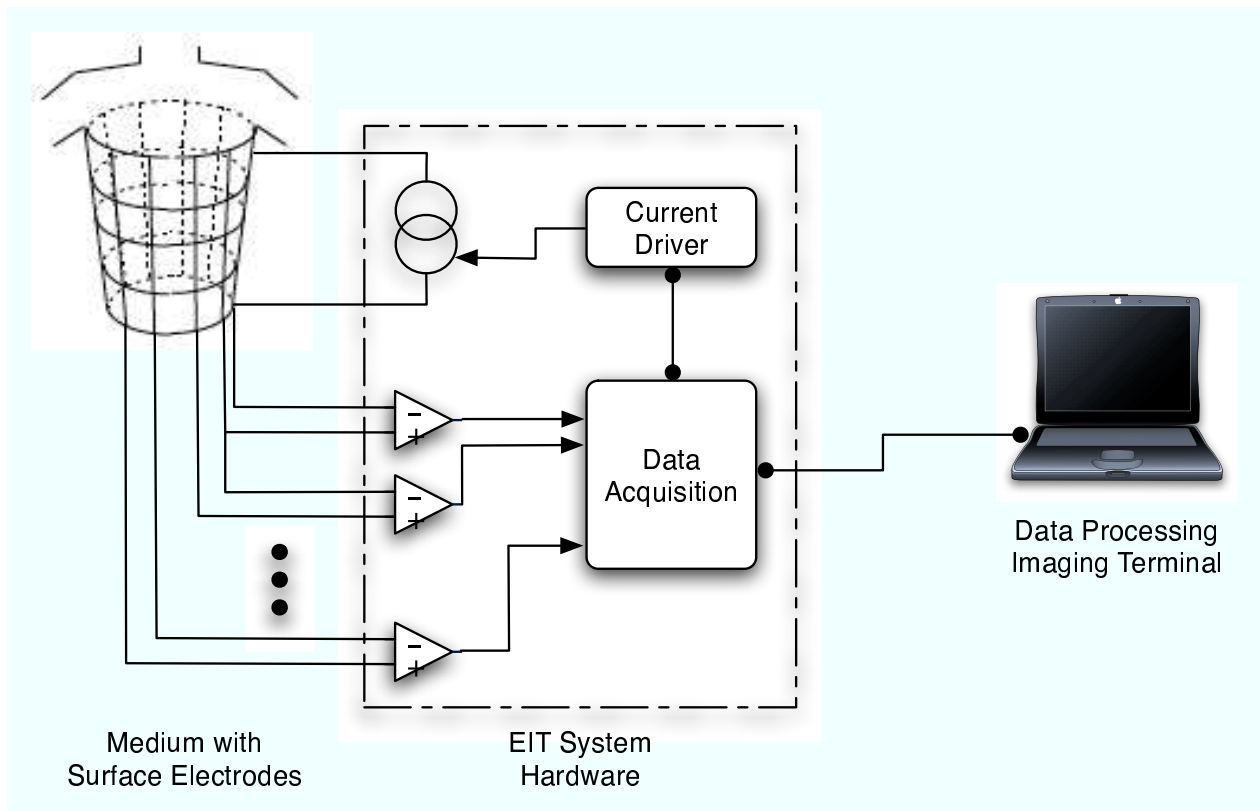


Figure 2.2: Conceptual diagram of a typical EIT system. The three main compartments are: (*left*) the patient connected by a network of electrodes, (*middle*) the EIT hardware with driver and acquisition units, and (*right*) a data processing and imaging terminal.

EIT instruments have integrated solutions for these issues and require little additional effort from the user.

2.2 Electrical Impedance Tomography

An elaboration of the brief description and terminology of EIT in section 1.1 is given here. Figure 2.2 is a diagram of a typical EIT setup. The patient is connected with the EIT hardware *via* a series of Ag/AgCl electrodes such that the region of interest is contained within the electrode grid. The EIT hardware consists mainly of a data acquisition unit, a current driver unit, and a central processing unit. Together, the EIT instrument executes the sequence of *excitation currents* and voltage measurements. For each excitation current, a pair of electrodes is chosen as the anode and the cathode. Their relative position can be *adjacent*, *opposite*, or of any other configuration. Simultaneously, the *voltage difference*

between adjacent pairs of remaining electrodes is measured, amplified, and digitized. Note that this implies the existence of some signal reference electrode, usually placed far from the region of interest. All measurements are collected as a *frame* and transmitted in matrix form to a data processing terminal which computes the conductivity images and displays tomographic images.

The *tomography* term in EIT refers to a slice-wise collection of data. Hence, the electrode grid is divided into *electrode rings*. Usually only intra-ring excitation currents and voltage measurements are used to stimulate the body. Other configurations are possible; although, rings are the most common (Graham & Adler, 2006a). Therefore, adjacent and opposite excitation currents with N_e electrodes for each of the N_r electrode rings have a total number of independent voltage difference measurements N_v , given by

$$N_v = \begin{cases} \frac{1}{2}N_eN_r(N_eN_r - 3) & \text{(adjacent),} \\ \frac{1}{4}N_eN_r(N_eN_r - 4) & \text{(opposite).} \end{cases} \quad (2.1)$$

We immediately see that N_v depends only on the product N_eN_r . Therefore, we need only consider the *total* number of electrodes which we rewrite simply as N_e . Also note that $2N_v$ measurements are possible with these patterns. However, only half of them are linearly independent due to the reciprocity property (Geselowitz, 1971). In many EIT calculations, all $2N_v$ voltage measurement data are used regardless of linear dependence. For example, our studies use a 16-electrode EIT instrument (*Viasys Healthcare*, Höchberg, Germany). From equation (2.1), adjacent and opposite excitation currents yield datasets of 208 and 96 voltage measurements, respectively. Although adjacent excitation currents yield more than twice as much data than opposite currents, some groups claim the latter is more representative of the internal conductivity since currents must flow across the body. This is discussed by Metherall (1998).

The EIT problem is satisfied by the solution of a partial differential equation with boundary values. Consider the body $\Omega \subset \mathbb{R}^3$ with C^2 -smooth boundary $\partial\Omega$. The conductivity distribution $\sigma = \sigma(x, y, z)$ and the electric potential distribution $\phi = \phi(x, y, z)$ are defined

over Ω . They must satisfy the generalized Laplace equation

$$\nabla \cdot \sigma \nabla \phi = 0 \quad (2.2)$$

where

$$\nabla = \mathbf{i} \frac{\partial}{\partial x} + \mathbf{j} \frac{\partial}{\partial y} + \mathbf{k} \frac{\partial}{\partial z}$$

is the vector differential operator. The boundary conditions represent the excitation currents applied to electrodes placed on $\partial\Omega$. The *Complete Electrode Model* (CEM) proposed by Cheng *et al.* (1989) analytically models finite area electrodes E_i numbered $i = 1, 2, \dots, N_e$ with contact impedance z_i such that, the excitation current I_i and corresponding voltage V_i are given by

$$\begin{aligned} I_i &= \int_{E_i} \sigma \frac{\partial \phi}{\partial \eta} dS, \\ V_i &= \phi + z_i \sigma \frac{\partial \phi}{\partial \eta}, \end{aligned}$$

where η is the inward normal vector of the boundary $\partial\Omega$. It is later shown, in chapter 4, that equation (2.2) is derived from Maxwell's equations of electromagnetism.

In order to solve equation (2.2) analytically, functions ϕ and σ are derived over the geometry of Ω . This can be analytically done for simple geometries such as spheres and cylinders (Kleinermaun *et al.*, 2000). However, for arbitrary geometries this task becomes daunting as closed form solutions are either enormous or non-existent. An approximate solution over a discretized Ω can be readily computed in these cases using the *Finite Element Method* (FEM) (Polydorides, 2002). The most commonly used discretizing *elements* are triangles and tetrahedrons; however, quadrilaterals and hexahedrons are also used in implementations by Blott *et al.* (1998), Cheney *et al.* (1999), Mueller *et al.* (2002), and Kolehmainen *et al.* (2005). The approximate solution requires that σ and ϕ be defined discretely for each element and each *node*, respectively. For example, the triangular elements shown in figure 2.3, taken from Asfaw (2005), are used for 2D discretization. Each node has a linear basis function used

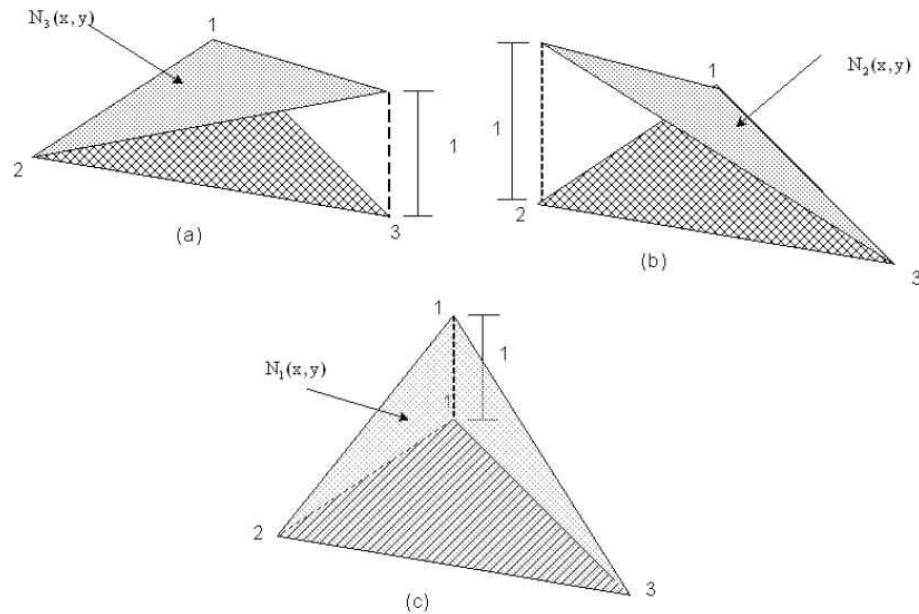


Figure 2.3: The linear basis functions of a triangular element used to measure the electric potential ϕ at each node and the conductivity σ for the element (reproduced from Asfaw (2005)).

to measure the electric potential ϕ and interpolate the average conductivity value σ for the enclosed element (Asfaw, 2005).

EIT instruments have been designed and built worldwide. Table 2.2 chronologically lists various EIT instruments used in published studies. Most of these instruments are listed in (Frerichs, 2000). This list is not exhaustive since some of these instruments have also been commercialized and used in other applications of EIT.

2.3 Medical Applications of EIT

A common medical application of EIT is the study of pulmonary function. Frerichs (2000) reviews most of these studies which were concerned with lung pathologies such as chronic obstructive pulmonary disease, bronchial carcinoma, plural effusions, embolism, pneumothorax, emphysema, sarcoidosis, atelectasis, and pneumonia. Other studies of lung function, such as plethysmography and regional lung perfusion, were researched by Adler *et al.* (1996), Kunst *et al.* (1998), and Frerichs *et al.* (2002). Figure 2.4 shows lung perfusion images using a conductive contrast in a normal bovine subject. Images are compared with electron

Model Used	Principle Investigator(s)	Publication Year	Sampling rate [†] (Hz)	Multi-frequency
Sheffield APT Mk 1	Brown and Seagar	1987	10	no
Rensselaer ACT 2	Newell	1988	?	no
Sheffield APT Mk 2	Smith	1990	25	no
Sheffield APT DAS-01P	Brown	1990	1	no
Montréal EIT	Guardo	1991	5	no
Cardiff EIT	Griffiths	1992	?	no
Göttingen EITS	Osypka	1993	s.m.	yes
Sheffield EITS	Brown	1994	33	yes
Rensselaer ACT 3	Cook	1994	?	no
Moscow EIT	Cherepin	1995	3.3	no
Stuttgart EIT	Li	1996	10	no
Keele Mk 1b	Taktak	1996	10	no
PulmoTrace-CardioInspect	Zlochiver	2005	20	no
Goe-MF II EIT	Adler	2006	12.5	no

Table 2.2: List of EIT instruments used in published EIT studies. [†]The ‘Sampling rate’ column refers to the data acquisition rate reported in studies published using this instrument (s.m. = single measurements). The ‘Multi-frequency’ column indicates whether the instrument is capable of generating multi-frequency excitation currents.

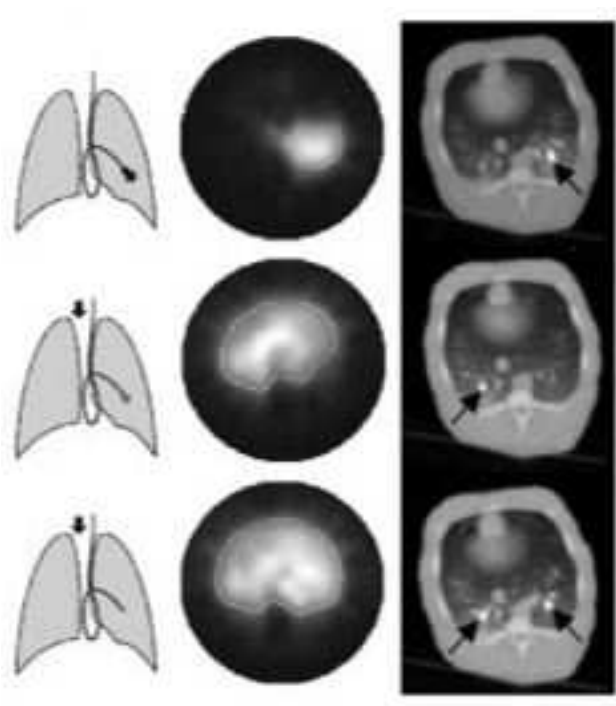


Figure 2.4: Lung perfusion imaging using a conductive contrast in normal bovine subject. *Left:* Sketch of perfusion catheter location. *Centre:* EIT images showing conductive contrast in white. *Right:* Electron beam CT with arrows indicating region of contrast injection (reproduced from Frerichs *et al.* (2002)).

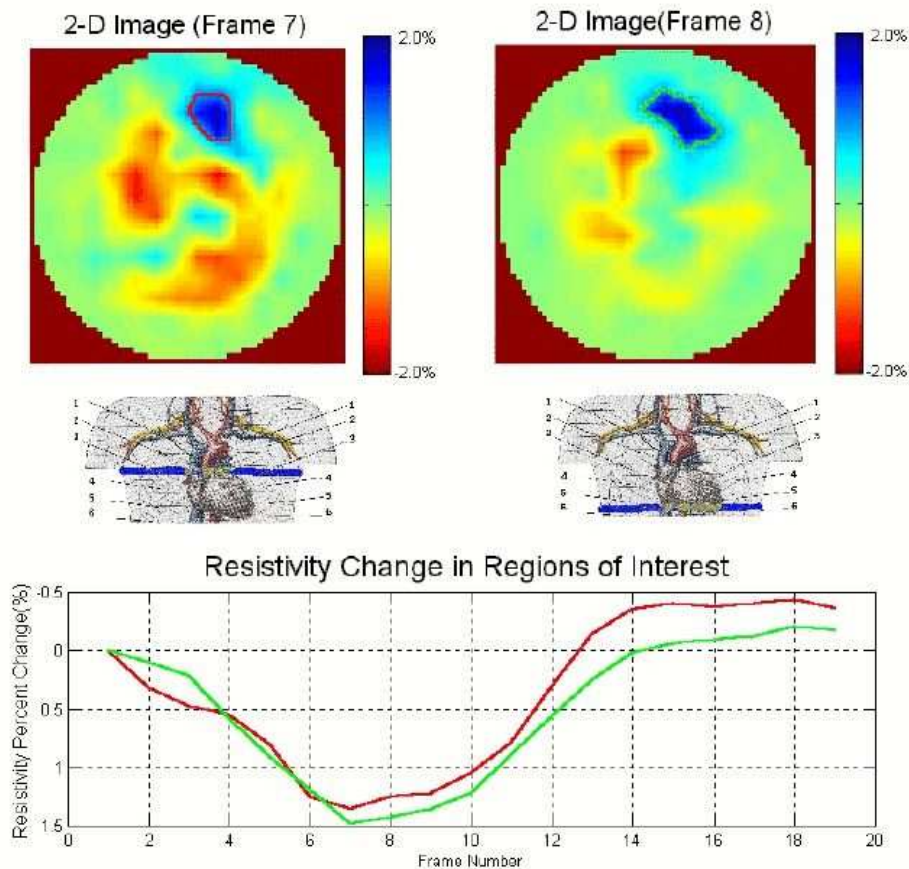


Figure 2.5: Estimation of stroke volume by measuring resistivity change in region of interest. EIT measurements were gated with an ECG and compared with MRI (reproduced from Patterson *et al.* (2001)).

beam CT (Frerichs *et al.*, 2002). Other EIT applications are mammography by Cherepenin *et al.* (2002), heart function by Patterson *et al.* (2001) (figure 2.5) and Zlochiver *et al.* (2006) Ongoing encephalography work by the London EIT group, supervised by Dr. D. Holder, is shown in figure 2.6.

As mentioned in section 1.3, a recurrent problem in medical EIT applications is the degradation of reconstructed images during measurement due to boundary deformation and poorly known electrode position. The following chapters describe EIT from a theoretical framework and address the problem of imaging deformable media.

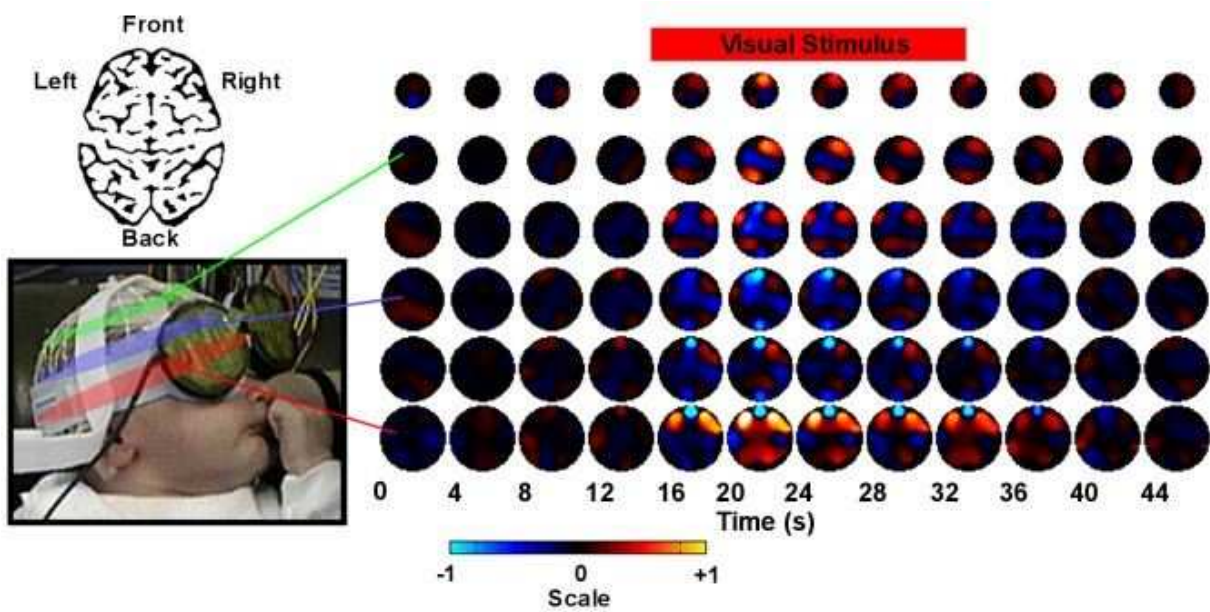


Figure 2.6: A visual evoked response of a neonate. Activity is reported as due to changes in blood flow (reproduced from the London EIT group website, 2006).

Chapter 3

Inverse Problem Theory

This chapter presents the mathematical theory that underlies EIT. We begin with some basic notations and definitions necessary to discuss the inversion of non-trivial systems. The second section formulates the general solution of an inverse problem using the Bayesian statistics of random variables. Although this probabilistic formulation does not directly provide applicable solutions, the insight from this paradigm is important in understanding the nature of all inverse problems. The final section presents some practical regularization methods used in discrete linear inverse problems. This material is used in next chapter to formally define EIT as an inverse problem.

3.1 Notations and Definitions

The branch of applied mathematics called “inverse problem theory” deals with interpreting observations from a poorly understood physical system to gain information about the system state. Specifically, an inverse problem infers the set of *model parameters* $\{m_1, m_2, \dots, m_n\}$ that describe the system from acquired set of *observation data* $\{d_1, d_2, \dots, d_n\}$. Figure 3.1 illustrates in an abstract sense the components of the inverse problem according to Tarantola (2005). The model parameters can be thought of as the coordinates of points on an abstract space termed the model manifold \mathfrak{M} . Hence, we only assume that \mathfrak{M} is a collection of points $\mathcal{M} = \mathcal{M}(m_1, m_2, \dots, m_n)$, but its structure can be otherwise arbitrary. Similarly,

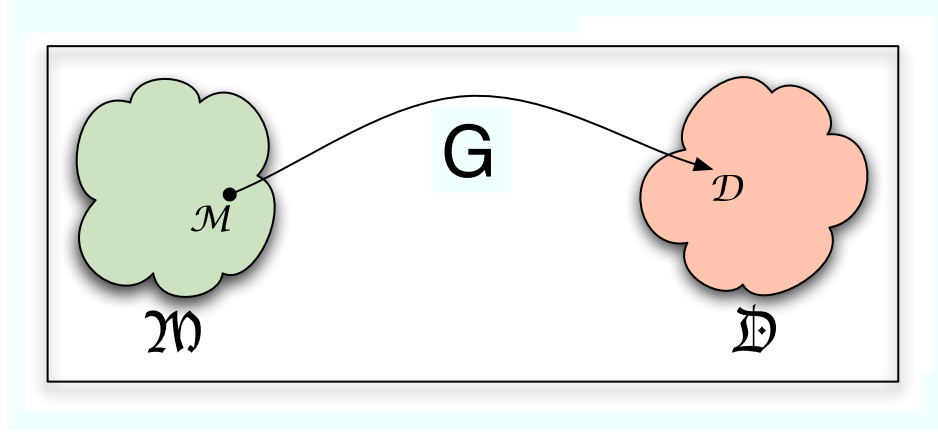


Figure 3.1: Abstract components of the inverse problem. Model parameters in the manifold \mathfrak{M} are mapped by the operator G to observation data in the manifold \mathfrak{D} .

the observation data are coordinates of points \mathcal{D} belonging to the observation manifold \mathfrak{D} . A particular value $\mathcal{M} \in \mathfrak{M}$ is mapped by the operator G to the corresponding $\mathcal{D} \in \mathfrak{D}$. Therefore, $G : \mathcal{M} \mapsto \mathcal{D}$ and $\mathcal{D} = G(\mathcal{M})$ is termed the *forward* problem; it represents the physical system that realizes the observable data. The general solution to the inverse problem is to find the operator G^{-1} such that $G^{-1}(G(\mathcal{M})) = \mathcal{M}$ for all $\mathcal{M} \in \mathfrak{M}$. Typically, “inverse problems” consist of the systems where finding G^{-1} is not trivial. Jacques Hadamard, in 1902, defined these cases as being *ill-posed* by the following.

Definition 1 (Hadamard). *Consider the operator system*

$$G(\mathcal{M}) = \mathcal{D}, \quad \mathcal{M} \in \mathfrak{M}, \quad \mathcal{D} \in \mathfrak{D} \quad (3.1)$$

where \mathfrak{M} and \mathfrak{D} are manifolds. The system is said to be well-posed if the following three conditions hold:

1. for each $\mathcal{D} \in \mathfrak{D}$ there exists a solution $\mathcal{M} \in \mathfrak{M}$,
2. for each $\mathcal{D} \in \mathfrak{D}$ there is a unique solution $\mathcal{M} \in \mathfrak{M}$, and
3. the operator G^{-1} is defined over \mathfrak{D} and is continuous. Therefore, the solution is stable under perturbations of the right-hand side of equation (3.1).

If the system is not well-posed then it is ill-posed.

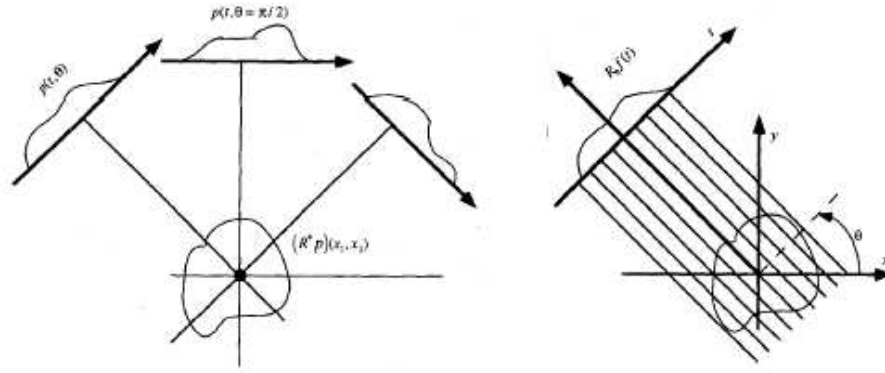


Figure 3.2: The axial projection process of the Radon transform (Unser & Alroubi, 1996).

In general, recasting an ill-posed problem into a well-posed representation is known as a *regularization* of the problem.

A further division is made on the linearity of G . Linear inverse problems can be formulated in terms of Hilbert space rather than manifolds. The system can be digitized and expressed in matrix form; and the problem can be solved with linear algebra. A very common example of a linear inverse problem is the Radon transform used in Computed Tomography imaging, which consists of an integral function over the set of all lines on a plane. The Radon transform is used to produce a collection of axial tomographic projections of a body $f(x, y)$ as shown in figure 3.2 taken from Unser & Alroubi (1996).

Consider a compact and bounded function $f(x, y)$ defined in \mathbb{R}^2 . The Radon transform of $f(x, y)$ is given by

$$\mathcal{R}_\theta[f](t) = \int_{-\infty}^{\infty} f(t \cos \theta - \xi \sin \theta, t \sin \theta + \xi \cos \theta) d\xi.$$

Then, $f(x, y)$ is represented by the projected data $\mathcal{R}_\theta[f]$ for $\theta \in [0, \pi)$.

The inverse problem consists of inferring $f(x, y)$ from $\mathcal{R}_\theta[f]$. In this example, $f(x, y)$ is chosen to be two rectangular objects of high contrast on a circular background. This image is shown on the left hand side of figure 3.3. The problem is discretized by taking twelve axial projections of this function, each separated by $\pi/12$ radians. The system matrix $A \in \mathbb{R}^{492 \times 1681}$ approximates the Radon transform as a weighted projection mask with a bilinear

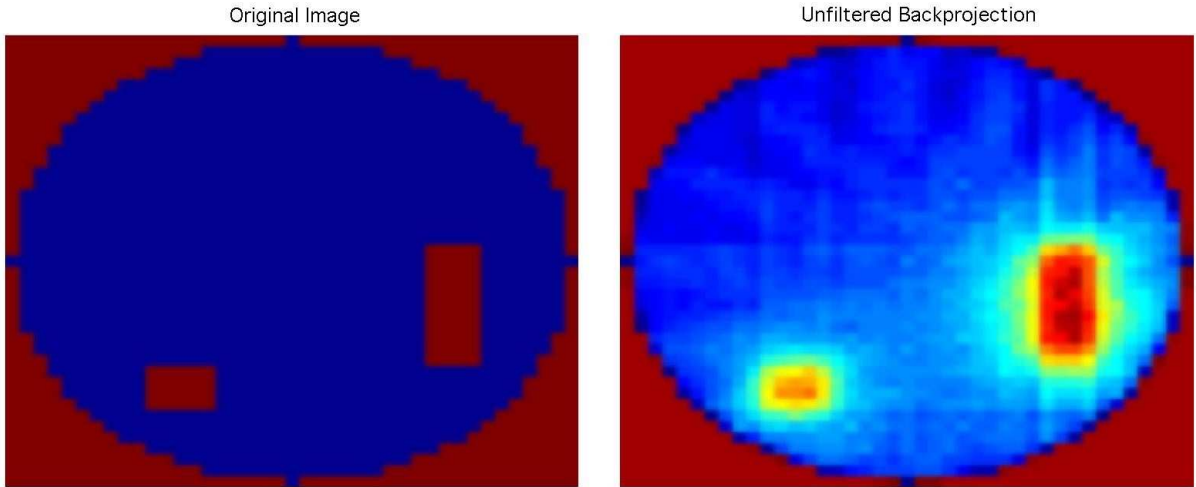


Figure 3.3: Numerical example of the Radon inverse problem. Twelve evenly spaced axial projections are taken forming the ill-conditioned system matrix A . *Left:* the original image $f(x, y)$. *Right:* the inverse image inferred from A^{-1} illustrated in a blue-white-red spectrum.

interpolation of pixels adjacent to the projection rays. The system matrix is underdetermined and is called *ill-conditioned*. When inverted, it produces the reconstructed image shown on the right hand side of figure 3.3.

Although the main features of the original are recovered in example 1, streaking artefacts due to the back-projection effect and smeared edges have deteriorated the reconstruction. These effects, as suggested in the third condition of the Hadamard definition, are due to the instability of the inverse problem. The system matrix A is rank-deficient and has some numerically linear-dependent rows. In order to remove these instabilities, well-known discrete regularization techniques, discussed later in section 3.3, can be used.

Non-linear inverse problems are considerably more complex. In this class of problems, the operator G is non-linear and obviously cannot be modelled with linear algebra. Since no general regularization techniques exist for this class, each problem must be individually studied. First, the Hadamard conditions must be theoretically examined, and only later can specific regularization methods be developed to solve the problem.

Other complicating effects arise when a system responds in a *non-local* or an *acausal* manner. *Non-local* means that the value of the function being inferred depends not only on the operator and its derivatives at that point, but rather depends from many points. *Acausal*

means that the occurrence of events depend not only on previous and current events, but also future ones. Physical inverse problems involving time always suffer from acausality. An illustrative example of this is heat diffusion in some material. Small changes in the initial heat distribution are smeared out in time over the entire body, having a very small influence on the final temperature. Trying to recover the initial distribution for measurements of the final temperature, i.e., the acausal direction, is more likely influenced by the resolution limits of the thermometer than the small changes in the initial heat distribution (Kaipio & Somersalo, 2005).

The following section provides insight into the nature of inverse problems. Next, a probabilistic model is formulated based on the ideas discussed.

3.2 Statistical Inversion

The objective of approaching the problem from a statistical paradigm is to extract information from observable quantities and assess their uncertainty using *i*) knowledge about the measurement process, *ii*) a physical model of the system, and *iii*) *a priori* knowledge about the solution.

The principles of statistical inversion can be summarized into three items (Kaipio & Somersalo, 2005):

1. the model parameters are considered *random variables*,
2. the randomness of each parameter reflects our *confidence* concerning their realizations, and
3. the solution of the inverse problem is the *posterior probability distribution*.

Consider the system model from equation (3.1) where we treat both \mathcal{M} and \mathcal{D} as random

vectors¹ $\mathbf{X} \in \mathbb{R}^n$, and $\mathbf{Y} \in \mathbb{R}^m$. Then we write

$$\mathbf{Y} = G(\mathbf{X}), \quad (3.2)$$

where $G : \mathbb{R}^n \rightarrow \mathbb{R}^m$ is some forward operator.

Suppose the *joint probability density* of \mathbf{X} and \mathbf{Y} , written as $f_{\mathbf{XY}}(x, y)$, is obtained from analysis of the system and measurement process. That is, $f_{\mathbf{XY}}(x, y)$ can be constructed using experimental information obtained from many forward problem simulations. Then the information that we can gather about the realizations of \mathbf{X} , in the inverse problem, can be expressed as a probability density.

Definition 2 (Prior density). *Given the joint probability $f_{\mathbf{XY}}(x, y)$ for \mathbf{X} and \mathbf{Y} in equation (3.2), the a priori probability density is defined as*

$$\rho_{\text{prior}}(x) = \int_{\mathbb{R}^m} f_{\mathbf{XY}}(x, y) dy. \quad (3.3)$$

Equation (3.3) quantifies which model parameters are most probable from the realizations of $G^{-1}(\mathbf{Y})$. Practically speaking, $\rho_{\text{prior}}(x)$ may also be empirical knowledge about the problem. For example, if \mathcal{M} represents some sort of image, then a priori information may be available describing the structure of the image, its smoothness, and how it changes in time. From our Radon transform example in section 3.1, $\rho_{\text{prior}}(x)$ gives us insight about the projection data $\mathcal{R}_\theta[f]$. For example, the projection data cannot be negative, the data variation for small θ will also be small, and $\mathcal{R}_\theta[f]$ is periodic for $\theta + k\pi$, $k \in \mathbb{Z}$.

Similarly, another probability density which can be constructed from experiment is the *likelihood* function, defined as follows.

Definition 3 (Likelihood function). *Given the joint probability $f_{\mathbf{XY}}(x, y)$ and a realization*

¹In general, \mathcal{M} and \mathcal{D} are *sets* of random variables and not *vectors* since \mathfrak{M} and \mathfrak{D} are not to be thought of as linear spaces. This terminology is used for convenience.

$\mathbf{X} = x$, the likelihood function is defined as

$$\rho(y | x) = \frac{f_{\mathbf{X}\mathbf{Y}}(x, y)}{\rho_{\text{prior}}(x)}, \quad \text{if } \rho_{\text{prior}}(x) \neq 0. \quad (3.4)$$

From the forward problem, equation (3.4) represents what realizations of \mathbf{Y} are most likely to be generated from $G(\mathbf{X})$.

From these definitions, the relation between the posterior probability, the *a priori* knowledge, and the likelihood function is stated in Bayes' theorem (Kaipio & Somersalo, 2005).

Theorem 1 (Bayes). *Assume that the random vector $\mathbf{X} \in \mathbb{R}^n$ has a known a priori probability density $\rho_{\text{prior}}(x)$ and the data consist of the realization $\mathbf{Y} = y$ of an observable random vector $\mathbf{Y} \in \mathbb{R}^m$ such that*

$$\rho(y) = \int_{\mathbb{R}^n} f_{\mathbf{X}\mathbf{Y}}(x, y) dx > 0.$$

Then, the posterior probability distribution of \mathbf{X} , given the data $\mathbf{Y} = y$, is

$$\rho_{\text{post}}(x) = \rho(x | y) = \frac{\rho_{\text{prior}}(x) \rho(y | x)}{\rho(y)}. \quad (3.5)$$

Tarantola (2005) states that equation (3.5) is the complete solution to the inverse problem. The function $\rho_{\text{post}}(x)$ considers all \mathcal{M} in \mathfrak{M} and contains information about the most probable solution, the confidence we have about that solution, the effect of errors due to poorly understood factors (i.e., noise), the measurement instrument's accuracy and precision, and its resolution limitations. In order to produce an actual set of model parameters \mathcal{M} from $\rho_{\text{post}}(x)$, an estimator is needed to quantitatively choose a specific solution.

The four estimators considered here answer distinct probabilistic questions. The realization of \mathbf{X} which is most probable of being obtained, given $\mathbf{Y} = y$ is termed the *maximum a posteriori* (MAP) estimator.

Definition 4 (Maximum a posteriori). *Given the posterior probability density $\rho_{\text{post}}(x)$ of the*

random vector $\mathbf{X} \in \mathbb{R}^n$, the maximum a posteriori estimate x_{MAP} satisfies

$$x_{\text{MAP}} = \arg \max_{x \in \mathbb{R}^n} \rho_{\text{post}}(x), \quad (3.6)$$

provided such a maximum exists.

Finding the MAP estimator is in itself an optimization problem and can also be challenging if $\rho_{\text{post}}(x)$ is not smooth.

The mean value of \mathbf{X} conditioned on our observation data $\mathbf{Y} = y$ is termed the *conditional mean* (CM) estimator.

Definition 5 (Conditional mean). *Given the posterior probability density $\rho_{\text{post}}(x) = \rho(x | y)$ of the random vector $\mathbf{X} \in \mathbb{R}^n$ and a realization $\mathbf{Y} = y$ of the random vector $\mathbf{Y} \in \mathbb{R}^m$, the conditional mean estimate is defined as*

$$x_{\text{CM}} = \int_{\mathbb{R}^n} x \rho(x | y) dx,$$

provided that the integral converges.

The CM estimator is an integration problem since $\rho_{\text{post}}(x)$ is usually defined over a high dimensional space. In statistical terms, the conditional mean is the expectation $\mathcal{E}\{x | y\}$.

Using the CM estimator, the second conditional moment can be calculated to estimate the “spread” of the posterior probability density about x_{CM} .

Definition 6 (Conditional covariance). *Given the posterior probability density $\rho_{\text{post}}(x) = \rho(x | y)$ and the conditional mean x_{CM} , the conditional covariance is defined as*

$$\text{cov}(x | y) = \int_{\mathbb{R}^n} (x - x_{\text{CM}})(x - x_{\text{CM}})^T \rho(x | y) dx,$$

provided that the integral converges.

Similar to the CM estimator, this is an integration problem over \mathbb{R}^n .

Another common statistical estimator is the *maximum likelihood*. However, we exclude it from inverse problem theory as it corresponds to an unregularized solution.

These estimators allow us to extract important features of the posterior probability density function. Furthermore, in simpler cases when the randomness of \mathbf{X} and \mathbf{Y} is Gaussian, the calculation of these estimators can be done without optimization or integration. A direct analysis of $\rho_{\text{post}}(x)$ is usually impractical since it is defined over a high dimensional space. Monte Carlo sampling methods exist, e.g., based on the Metropolis-Hastings and Gibbs sampling algorithms, that efficiently represent the posterior density with fewest sample points (West *et al.*, 2004). These methods are useful in studying particular inverse problems or their statistics in depth.

3.3 Discrete Regularization Methods

Suppose the system from equation (3.1) is linear and discretized so that

$$Ax = y, \quad x \in \mathbb{R}^n, \quad y \in \mathbb{R}^m, \quad (3.7)$$

and $A \in \mathbb{R}^{m \times n}$ is a linear operator representing G . The matrix A can be decomposed by two orthonormal bases where each base vector is scaled by the *singular values* of A . Then the *singular value decomposition* (SVD) of $A \in \mathbb{R}^{m \times n}$ is written as

$$A = U\Sigma V^T = \sum_{i=1}^n u_i \sigma_i v_i^T$$

where

$$U = (u_1, u_2, \dots, u_n) \in \mathbb{R}^{m \times n},$$

$$V = (v_1, v_2, \dots, v_n) \in \mathbb{R}^{n \times n},$$

$$\Sigma = \text{diag}(\sigma_1, \sigma_2, \dots, \sigma_n).$$

The sequence of singular values $\{\sigma_i\}_1^n$ is monotonic, non-negative, non-increasing, and converge to zero absolutely. The measure of numerical tractability of a linear system is given by its *condition number*, denoted by $\kappa(\cdot)$. The full rank matrix $A \in \mathbb{R}^{m \times n}$ has a condition number given by $\kappa(A) = \|A\| \|A^{-1}\|$ if A^{-1} exists. In general $\kappa(\cdot)$ can be computed by using the so-called pseudoinverse A^\dagger

$$\kappa(A) = \|A\| \|A^\dagger\| = \frac{\sigma_1}{\sigma_{\text{rank}(A)}} \quad (3.8)$$

where A^\dagger is the Moore-Penrose generalized inverse

$$A^\dagger = \sum_{i=1}^{\text{rank}(A)} v_i \sigma_i^{-1} u_i^T.$$

Note that the condition number is the ratio of the maximum, i.e., the first, singular value and the singular value corresponding to the numerical rank index. Ill-conditioned matrices have a correspondingly high condition number. The condition number is essentially the error amplification factor applied to y in equation (3.7).

The ill-conditioned system matrix will inherit the behaviour of two types of problems according to Hansen (1998).

1. *Rank-deficient problems* exhibit a redundancy of information by having numerically linear-dependent rows of A . The SVD of A reveals a cluster of small singular values separated by a distinct gap from the larger singular values. These problems can be regularized by extracting the linearly independent information to yield a well-conditioned, full rank matrix.
2. *Discrete ill-posed problems* arise when the original problem in equation (3.1) is ill-posed. The numerical rank equals the number of columns of A and no gap is visible in the singular value spectrum. These problems may be regularized if an equilibrium exists between the residual norm $\|y - Ax\|$ and the observed solution $\|y\|$.

The inverse of A cannot be directly computed since the small singular values grow without

bound, amplifying the noise components of the solution associated with the numerical null space of A . Equivalently, small measurement perturbations $y \approx y + \epsilon$ produce large variations in x such that the 2-norm *residual error* $\|Ax - y\|_2$ is unbounded.

To address these issues, a regularization of the problem can be applied. Many techniques are proposed mainly in a *heuristic* framework. Andrey Nikolayevich Tikhonov originally proposed the minimization of a constrained least-squares functional by *ad hoc* variation of a single regularization parameter, termed the *hyperparameter* λ

$$x_\lambda = \arg \min_{\lambda} \left\{ \|Ax - y\|_2^2 + \lambda W(x) \right\}, \quad (3.9)$$

where $W(x)$ is some penalty function also referred to as the *regularization error*. From this, direct methods have emerged such as Total Variation, Modified Singular Value Decomposition, and Maximum Entropy. Iterative methods such as Conjugate Gradient, Bidiagonalization, and the ν -Method are worthy alternatives to direct methods when dealing with large systems that are too time consuming to factorize (Hansen, 1998).

Since the regularization parameter is heuristically selected in direct methods, selection criteria are designed to provide the optimal solution. Four such criteria are the discrepancy principle, generalized cross-validation, quasi-optimality, and the L-curve presented by Hansen (1998). These attempt to incorporate whatever prior knowledge is available about the system to discriminate against parameter values that produce meaningless solutions. In the best situation, the error residual is well known and its mean can easily be calculated *a priori*. Unfortunately, this is seldom the case and little is known about the sources of error that are often collectively referred to as noise.

Recall the Radon transform example in section 3.1. The system matrix is ill-conditioned and has a condition number given by equation (3.8) of $\kappa(A) = 419.17$. Its singular value spectrum, shown in figure 3.4, shows a distinct gap in singular values beyond σ_{462} , corresponding to the numerical rank of A . This problem is regularized using the Tikhonov method where the error function is based on the identity matrix $W(x) = \|I_n x\|$.

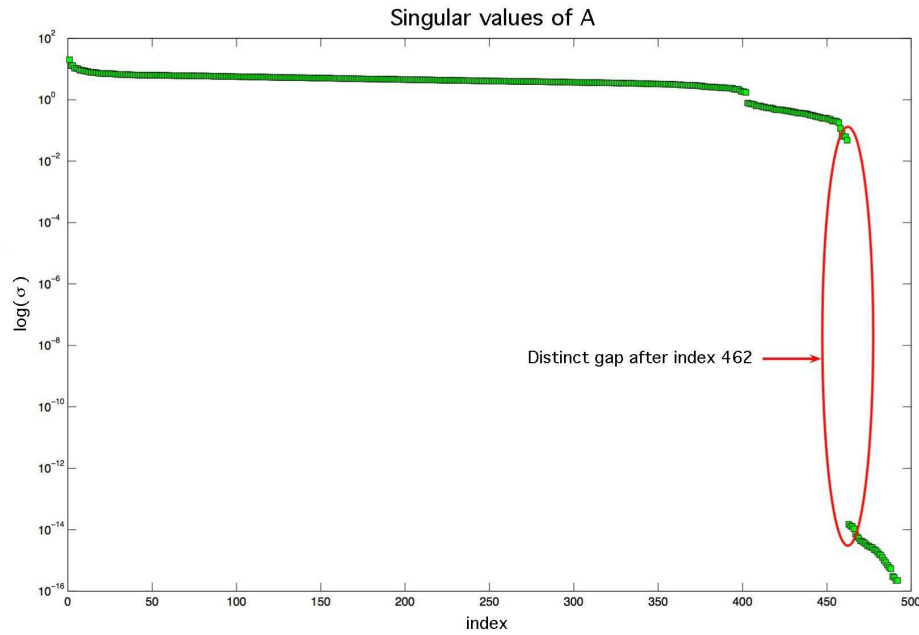


Figure 3.4: The singular value spectrum of the Radon transform example in section 3.1. A distinct gap is visible after the σ_{462} , which corresponds to the numerical rank of A . The condition number of A is $\kappa(A) = 419.17$.

In matrix form, equation (3.9) becomes

$$x_\lambda = (A^T A + \lambda I_n)^{-1} A^T y.$$

The optimal value for the hyperparameter corresponds to the minimum total error $\|Ax - y\| + \|I_n y\|$ and is found to be $\lambda \approx 0.066$ in this case. This method is yet another way of finding a good value for the hyperparameter apart from those mentioned above by Hansen (1998). Figure 3.5 shows the regularized image to the right of the unfiltered one, originally shown in figure 3.3. The streaking artefacts and blurring of edges are reduced at the expense of introducing some background noise. The resulting image from unfiltered backprojection can also be achieved by Tikhonov regularization using a very large hyperparameter, in this case $\lambda > 1$.

Regularization must be carefully used since it creates bias based on the *a priori* information given. In computed simulations, particularly, it is easy to introduce practically inaccessible *a priori* information which renders the inverse solution unrealistically accurate. This is referred in the literature as the *inverse crime* and is documented and discussed in

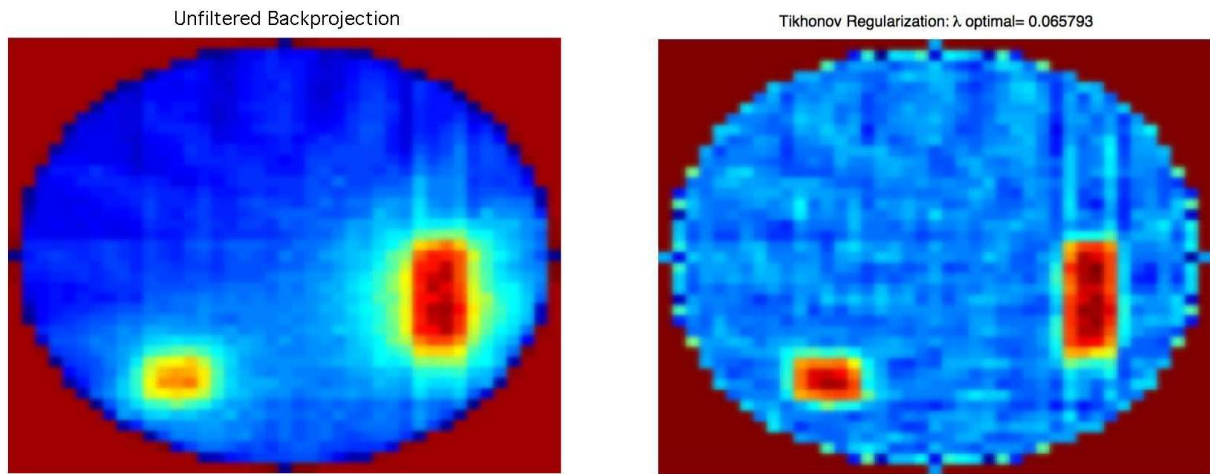


Figure 3.5: Revisited numerical example of the Radon inverse problem. Twelve evenly spaced axial projections are taken forming the ill-conditioned system matrix A . *Left:* The unfiltered image reconstruction from A^{-1} . *Right:* The Tikhonov regularized image reconstruction with $\lambda = 0.066$.

depth, along with other forms of misinterpretation of data, by Adler & Lionheart (2006).

Chapter 4

Electrical Impedance Tomography

This chapter formally introduces EIT as an inverse problem. The formulation derived here is the foundation of EIT and serves as the basis for the study of the deformable media problem. The first section defines the EIT inverse problem in terms of the physical laws of electromagnetics. The second section formulates the linearization of EIT using the Finite Element Method (FEM) and defines the linear systems implemented for the forward and inverse problems. The final section describes the image reconstruction algorithms used to obtain images from frames of measurement data acquired over time. The problem is considered in 3D and the 2D problem can be derived as its subset.

4.1 The EIT Inverse Problem

The partial differential equation (2.2) governing the electrodynamics of the EIT problem is derived from Maxwell's equations based on three major assumptions about the medium under investigation. Consider the medium $\Omega \subset \mathbb{R}^3$ with C^2 -smooth boundary $\partial\Omega$ with the following properties.

1. *Isotropic conductor*: the admittivity $\gamma(x)$ for $x \in \Omega$ is a scalar function

$$\gamma(x) = \sigma(x) + j\omega\epsilon(x).$$

2. *Quasi-static*: the excitation current frequency ω is low enough to allow the medium to return to equilibrium such that the induced electric displacement field \mathbf{D} and the magnetic flux density \mathbf{B} are constant

$$\frac{\partial \mathbf{D}}{\partial t} = \frac{\partial \mathbf{B}}{\partial t} = 0, \quad (4.1)$$

and the reactive component of the material is negligible $\gamma(x) \approx \sigma(x)$.

3. *Linear conductor*: the current density field \mathbf{J} is linearly related to the electric field \mathbf{E} such that

$$\mathbf{J} = \gamma \mathbf{E}. \quad (4.2)$$

Maxwell's equations are

$$\begin{aligned} \nabla \cdot \mathbf{D} &= \rho \\ \nabla \cdot \mathbf{B} &= 0 \\ \nabla \times \mathbf{E} &= -\frac{\partial \mathbf{B}}{\partial t} \end{aligned} \quad (4.3)$$

$$\nabla \times \mathbf{H} = \frac{\partial \mathbf{D}}{\partial t} + \mathbf{J} \quad (4.4)$$

where \mathbf{H} is the magnetic field. The divergence of Ampère's law (4.4) under a quasi-static system (4.1) yields the conservation of charge law such that ρ is constant.

$$\nabla \cdot \mathbf{J} = \nabla \cdot \nabla \times \mathbf{H} = 0 \quad (4.5)$$

Faraday's law (4.3) under the quasi-static system (4.1) states that the electric field is irrotational $\nabla \times \mathbf{E} = 0$ and is, therefore, completely described by the electric potential gradient.

$$\mathbf{E} = -\nabla \phi \quad (4.6)$$

Our result is obtained by combining equations (4.5), (4.2) and (4.6).

$$\nabla \cdot \mathbf{J} = \nabla \cdot \sigma \mathbf{E} = \nabla \cdot \sigma \nabla \phi = 0 \quad (4.7)$$

Equation (4.7) is a generalized form of Laplace's equation, which governs the conductivity and electric potential quantities in the EIT problem. It is subject to mixed Dirichlet and Neumann boundary conditions proposed by Cheney *et al.* (1999) in the Complete Electrode Model (CEM). We require that the inward normal component of the current density $\mathbf{J} \cdot \boldsymbol{\eta} \in \partial\Omega$ is non-zero only where the electrodes are attached. Hence, the Neumann condition for equation (4.7) is

$$\sigma \frac{\partial \phi}{\partial \boldsymbol{\eta}} = \begin{cases} \mathbf{J} & \text{on electrodes} \\ 0 & \text{elsewhere.} \end{cases}$$

The excitation current I_i for each electrode $\{E_i \mid i = 1, \dots, N_e\}$ is given by the surface integral

$$\int_{E_i} \sigma \frac{\partial \phi}{\partial \boldsymbol{\eta}} dS = I_i \quad (4.8)$$

and the voltage V_i measured at each electrode is modelled by mixed Dirichlet and Neumann conditions

$$\left(\phi + z_i \sigma \frac{\partial \phi}{\partial \boldsymbol{\eta}} \right) \Big|_{E_i} = V_i. \quad (4.9)$$

Equations (4.7), (4.8), and (4.9) are subject to Kirchoff's current and voltage laws $\sum^{N_e} I_i = \sum^{N_e} V_i = 0$ and make up the CEM.

The existence of solutions with the CEM is proven by Somersalo *et al.* (1992). Uniqueness questions are investigated by Lionheart (1997) and show that unique solutions exist for both isotropic and anisotropic conductivities with restrictions on the latter. The third Hadamard condition however is violated, classifying EIT as an ill-posed problem. The inverse problem is the recovery of $\sigma \in \Omega$ given $V = \{V_i \mid 1, \dots, N_v\}$, where N_v is the number of independent measurements given by equation (2.1). This relation is governed by a non-linear, ill-posed operator $G^{-1} : V \mapsto \sigma$. This operator also has the property of being non-local, i.e., $\sigma(x)$ for a particular $x \in \Omega$ will significantly affect the measurements at most of the

electrodes. Therefore, *all* measurements must be related to *all* $x \in \Omega$ and simultaneously solved. In addition, the system is underdetermined since only a finite number of independent measurements is available to solve an internal conductivity distribution of arbitrary complexity. Without regularization, small changes in V produce large variations of σ and unrecognizable image reconstructions. To rectify this instability, *a priori* information about the system and the expected solution is introduced by regularizing the problem. The problem is, first, discretized using the FEM and, second, solved as a linear approximation. The practical applications of EIT are implemented based on FEM techniques described in the following section.

4.2 Finite Element Method

A discretized version of the medium is represented using the FEM such that Ω is partitioned into a mesh of N_k tetrahedral elements and N_p nodes representing the element vertices. The FEM meshes are computed using NETGEN (Schöberl, 1997) using the EIDORS suite. Figure 4.1 shows two FEM mesh types used to discretize cylindrical and circular media. The left side shows a 828 tetrahedral element mesh with 252 nodes and the right side shows a 576 triangular element mesh with 313 nodes.

In the FEM model, nodes are associated with the electric potential value $\phi = \phi(x)$ corresponding to a point $x \in \Omega$. In matrix form, the node potentials are written as the column vector $\Phi = (\phi_1, \phi_2, \dots, \phi_{N_p})^T \in \mathbb{R}^{N_p}$. Similarly, the electrode voltages are also written as a column vector $V \in \mathbb{R}^{N_e}$ and are defined by equation (4.9). The EIT forward problem is to calculate V given the internal conductivity distribution, which is also represented in vector form as $\sigma = (\sigma_1, \sigma_2, \dots, \sigma_{N_k})^T \in \mathbb{R}^{N_k}$. The forward problem is stated in another way as to include the *complete* excitation current pattern and the FEM mesh structure into the problem.

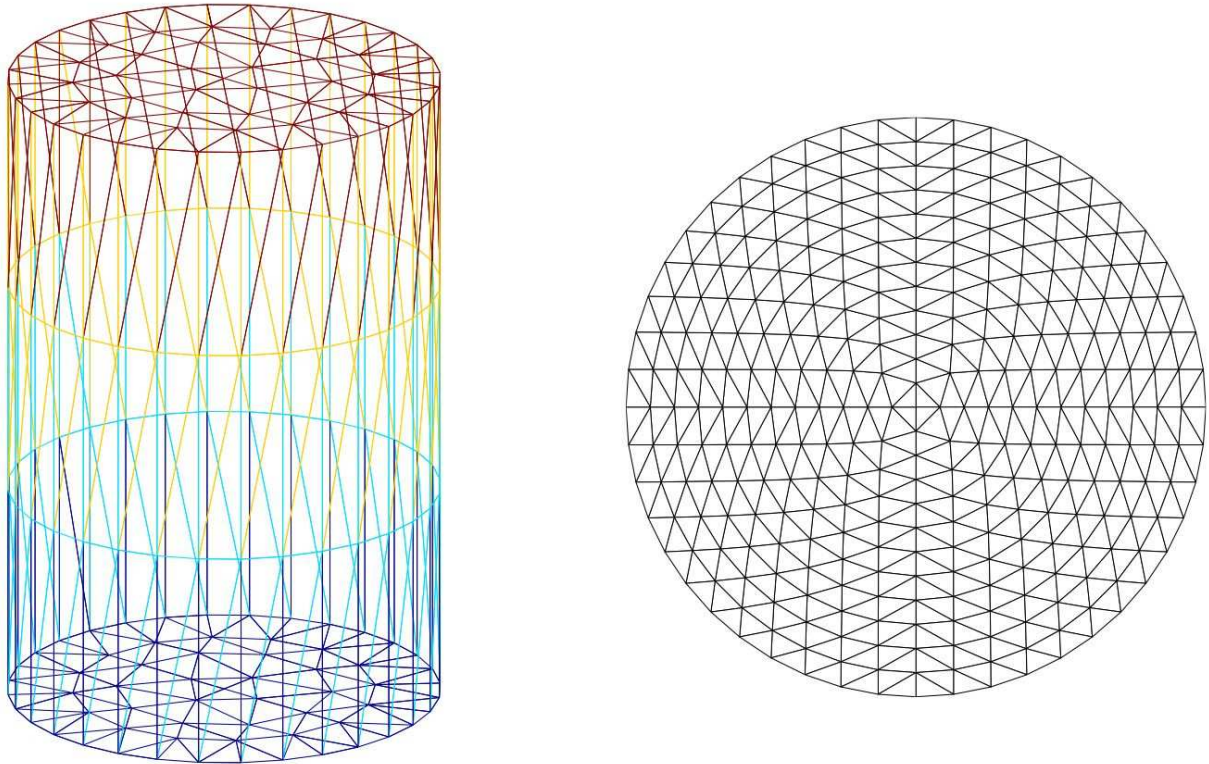


Figure 4.1: FEM meshes generated using EIDORS. *Left:* cylindrical mesh of 828 elements and 252 nodes. *Right:* circular mesh of 576 elements and 313 nodes.

4.2.1 The Forward Problem

The above formulations, including equations (4.8) and (4.9), are described in the context of a single excitation current. However, in the general problem, we consider the complete excitation pattern that produces a *frame* of measurement data at a particular time. Hence, we consider the complete set of independent voltage measurements expressed in matrix form as $V \in \mathbb{R}^{N_e \times N_e}$, containing exactly N_v independent measurements. Correspondingly, the pattern of excitation currents is given by the matrix $I \in \mathbb{R}^{N_e \times N_e}$. Thus, each column of V corresponds with a single excitation current.

The FEM model requires a linear operator A to map the node potentials Φ and the electrode voltages V to the excitation currents I . This is accomplished by solving equation (4.7) in a weaker form due to the introduction of node basis functions that are not differentiable. The calculations are done by Polydorides (2002) and implement the CEM using an augmented conductivity matrix A ; it is obtained from the FEM node basis functions

$\{\psi_1, \dots, \psi_{N_p}\}$ such that ψ_i is unity for node i and zero elsewhere.

$$\begin{bmatrix} A_\alpha + A_\beta & A_\gamma \\ A_\gamma^T & A_\delta \end{bmatrix} \begin{bmatrix} \Phi \\ V \end{bmatrix} = \begin{bmatrix} 0 \\ I \end{bmatrix} \quad (4.10)$$

The submatrices are numerically calculated from the weak solution of equation (4.7):

$$\begin{aligned} A_\alpha(i, j) &= \sigma \int_{\Omega} \nabla \psi_i \cdot \nabla \psi_j dV, & i, j = 1, \dots, N_p. \\ A_\beta(i, j) &= \sum_{k=1}^{N_e} \frac{1}{z_k} \int_{E_k} \psi_i \psi_j dS, & \text{for nodes } i, j \text{ on } E_k. \\ A_\gamma(i, j) &= -\frac{1}{z_j} \int_{E_j} \psi_i dS, & \text{for nodes } i \text{ on } E_j. \\ A_\delta &= \text{diag} \left(\frac{1}{z_k} \int_{E_k} dS \right), & k = 1, \dots, N_e. \end{aligned}$$

The CEM is implemented as A_β , A_γ , and A_δ . Hence, these matrices are only computed over the electrodes. The *system matrix* A is symmetric positive-definite and depends on σ and the FEM mesh structure. Figure 4.2 shows a sparse plot of the system matrix A and its components from equation (4.10). The forward problem is then

$$\begin{bmatrix} \Phi \\ V \end{bmatrix} = A^{-1} \begin{bmatrix} 0 \\ I \end{bmatrix}$$

and is efficiently computed using a Cholesky factorization of A .

4.2.2 The Inverse Problem

The forward problem establishes the ohmic relationship between the currents and the potentials in the system. The inverse problem is the one encountered in applications of EIT where the conductivity distribution σ and the internal electric potentials Φ are unknown. A general solution of the ill-posed non-linear operator $G^{-1} : V \mapsto \sigma$ remains unresolved in the literature. However, Siltanen *et al.* (2000) have solved the 2D problem. A linearization of

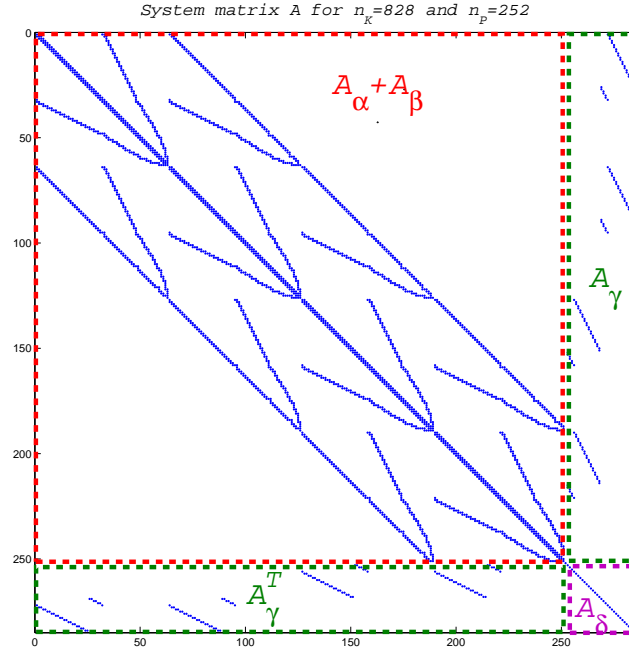


Figure 4.2: Sparse plot of the 284×284 system matrix A and its submatrices from EIDORS. The FEM model is cylindrical with 828 elements, 252 nodes and two 16-electrode rings. The excitation currents use the adjacent protocol and the condition number is $\kappa(A) = 15,876$.

the problem is implemented by computing the *Jacobian* of G , assuming that the operator is differentiable over σ . Since the Jacobian is the matrix-equivalent to the derivative of a scalar function, then J is the best linear approximation near a point σ_0

$$G(\sigma) \approx J(\sigma - \sigma_0). \quad (4.11)$$

Hence, for $G : \mathbb{R}^{N_k} \rightarrow \mathbb{R}^{N_v}$, there are N_v functions of the form $V_i = V_i(\sigma_1, \dots, \sigma_{N_k})$. Therefore, the Jacobian J of G is

$$J = \begin{bmatrix} \frac{\partial V_1}{\partial \sigma_1} & \dots & \frac{\partial V_1}{\partial \sigma_{N_k}} \\ \vdots & \ddots & \vdots \\ \frac{\partial V_{N_v}}{\partial \sigma_1} & \dots & \frac{\partial V_{N_v}}{\partial \sigma_{N_k}} \end{bmatrix}. \quad (4.12)$$

The Jacobian also quantifies the *sensitivity* of V with respect to σ and is calculated based on marginal changes of $\phi \rightarrow \phi + \delta\phi$, $V \rightarrow V + \delta V$, and $\sigma \rightarrow \sigma + \delta\sigma$ in equation (4.7). This is termed the *perturbation method* of calculating the Jacobian. Each member $[J]^{ij}$ is computed

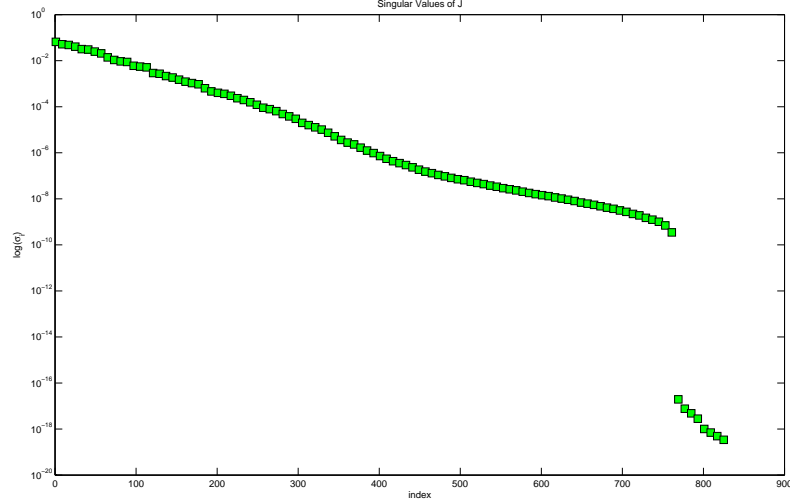


Figure 4.3: The singular value spectrum of the 928×828 Jacobian matrix J of the system, shown in figure 4.2. A distinct gap occurs after σ_{765} corresponding to the numerical rank. The condition number is $\kappa(J) = 4.24 \times 10^8$. Only every eighth singular value σ_i is shown.

by integrating over element Ω_j for each independent measurement $i = (d, m)$ from electrode E_m and excitation current I_d (Polydorides, 2002)

$$\frac{\partial V_i}{\partial \sigma_j} = \int_{\Omega_j} \nabla \phi_d \cdot \nabla \varphi_m dV. \quad (4.13)$$

Here φ_m represents the electric potential calculated in terms of the voltage measurement at electrode E_m . The Jacobian is a very ill-conditioned matrix and requires regularization to solve the inverse problem. For example, the Jacobian matrix calculated from the 284×284 system matrix A shown in figure 4.2 is a 928×828 matrix. The Jacobian has a rank of 765 and, therefore, is rank deficient. Its condition number, given by (3.8), is $\kappa(J) = 4.24 \times 10^8$. As expected, the singular value spectrum of J reveals a gap after the 765th singular value in figure 4.3. In order to solve the inverse problem, we require the inverse of $J^T J$ to obtain the desired conductivity distribution $\sigma \in \mathbb{R}^{N_k}$. In the final section of this chapter, the EIT inverse problem is solved by the *maximum a posteriori* (MAP) regularization technique formulated in section 3.2.

4.3 MAP Image Reconstruction Algorithm

The MAP solution is derived for the EIT model parameters in terms of the inverse problem theory from chapter 3. In the simplest case, when a Gaussian *a priori* density $\rho_{\text{prior}}(\sigma)$ is used, the corresponding Gaussian posterior distribution $\rho_{\text{post}}(\sigma)$ can be analytically calculated in closed form. These matching distributions are termed *Bayesian conjugates*, and such a situation can occur when system parameters describe some combination of many smaller random variables. It becomes very difficult (perhaps impossible) to express these parameters analytically with a probability density function. However, the central limit theorem states that as the number of random factors affecting the variable becomes large, its distribution becomes Gaussian. Therefore, the posterior distribution can be written in analytic form.

Consider the linearized EIT problem from equation (4.12) in the presence of an additive noise vector $n \in \mathbb{R}^{N_v}$ affecting each measurement

$$V = J\sigma + n. \quad (4.14)$$

Since J is not necessarily a square matrix, we must use the least-squares form to solve for the conductivity distribution such that our estimate σ_{LS} is

$$\sigma = (J^T J)^{-1} J(V - n).$$

Regularization is required to obtain an accurate estimate of σ since J and, therefore, $J^T J$ are ill-conditioned. We assume as *a priori* information that σ is characterized by a Gaussian probability density

$$\rho_{\text{prior}}(\sigma) \propto \exp\left(-\frac{1}{2}(\sigma - \sigma_{\text{prior}})^T \Sigma_{\sigma}^{-1}(\sigma - \sigma_{\text{prior}})\right)$$

where σ_{prior} and Σ_{σ} are the *a priori* value and covariance matrix of σ , respectively. In the simplest form, we choose $\sigma_{\text{prior}} = \mathcal{E}\{\sigma\}$. We further assume that $n = V - J\sigma$ is additive

Gaussian noise with covariance Σ_n such that the *likelihood* function is

$$\rho(V | \sigma) \propto \exp \left(-\frac{1}{2} (V - J\sigma)^T \Sigma_n^{-1} (V - J\sigma) \right).$$

Then, from the MAP estimate equation (3.6),

$$\begin{aligned} \sigma_{\text{MAP}} &= \arg \max_{\sigma} \{k \rho_{\text{prior}}(\sigma) \rho(V | \sigma)\} \\ &= \arg \max_{\sigma} \left\{ \exp \left(-\frac{1}{2} [(V - J\sigma)^T \Sigma_n^{-1} (V - J\sigma) + (\sigma - \sigma_{\text{prior}})^T \Sigma_{\sigma}^{-1} (\sigma - \sigma_{\text{prior}})] \right) \right\} \end{aligned}$$

where k is a constant. The maximum is obtained by minimizing the exponential term in a quadratic form

$$\begin{aligned} &\arg \min_{\sigma} \{ (V - J\sigma)^T \Sigma_n^{-1} (V - J\sigma) + (\sigma - \sigma_{\text{prior}})^T \Sigma_{\sigma}^{-1} (\sigma - \sigma_{\text{prior}}) \} \\ \implies 0 &= (J^T \Sigma_n^{-1} J + \Sigma_{\sigma}^{-1}) \sigma - (J^T \Sigma_n^{-1} V + \Sigma_{\sigma}^{-1} \sigma_{\text{prior}}) \end{aligned}$$

Therefore the MAP estimate of the conductivity is given by

$$\sigma_{\text{MAP}} = (J^T \Sigma_n^{-1} J + \Sigma_{\sigma}^{-1})^{-1} (J^T \Sigma_n^{-1} V + \Sigma_{\sigma}^{-1} \sigma_{\text{prior}}). \quad (4.15)$$

It has been shown by Aster *et al.* (2005) that equations of the form (4.15) reduce to another standard linear least-squares problem

$$\sigma_{\text{MAP}} = \arg \min_{\sigma} \left\| \begin{bmatrix} J/\sqrt{\Sigma_n} \\ 1/\sqrt{\Sigma_{\sigma}} \end{bmatrix} \sigma - \begin{bmatrix} (V - J\sigma)/\sqrt{\Sigma_n} \\ \sigma_{\text{prior}}/\sqrt{\Sigma_{\sigma}} \end{bmatrix} \right\|^2. \quad (4.16)$$

Note that equations (4.15) and (4.16), when coupled with a broad or zero prior, produces the unregularized least-squares or *maximum likelihood* solution. The prior information creates a bias on each parameter element such that a particular solution seems more attractive than another mathematically admissible solution. Hence, the desired information from the regularized solution should be emphasized by the prior selected.

Another interesting perspective of the MAP solution is from signal filter theory in

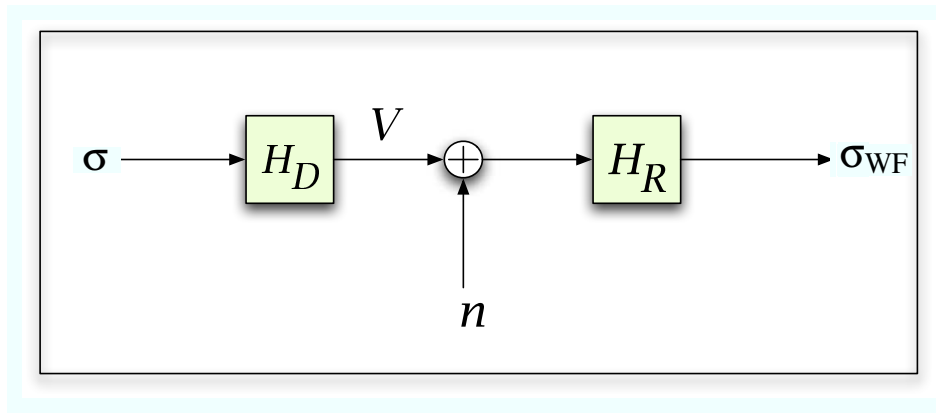


Figure 4.4: Block diagram of the Wiener filter applied to the EIT problem. The blocks H_D and H_R are the degradation and reconstruction processes, respectively.

electrical engineering. The Wiener filter is often used in image processing applications when the original image is degraded by some process. The essential concept is to use a *reconstruction process* to block the frequency spectrum of the noise and a *degradation process* to recover a reasonable estimate of the original image. Figure 4.4 shows a block diagram of the filter applied to the EIT problem. σ is the original image, n is additive noise, and the blocks H_D and H_R are the degradation and reconstruction processes, respectively. The Wiener filter estimate σ_{WF} is formulated in terms of H_D , H_R , and the *signal-to-noise ratio* (SNR). The SNR is equal to the ratio of power spectrum densities of the noise S_n and image S_σ , respectively

$$H_R = \frac{H_D^*}{H_D H_D^* + S_n / S_\sigma}.$$

In signal processing terms, H_D and H_R are the Fourier domain transfer functions of the degradation and reconstruction processes. That is,

$$\begin{aligned} H_D = \mathcal{F}\{h_D\} &\implies \sigma * h_D = J\sigma \\ H_R = \mathcal{F}\{h_R\} &\implies (V + n) * h_R = L(V + n) \end{aligned}$$

where L is the matrix form of the reconstruction process. To find L , we minimize the square error term $\epsilon^2 = \|\sigma - \sigma_{WF}\|^2$ over σ_{WF} . Since the reconstruction process operates on the

arbitrary input V , we also require that $\mathcal{E}\{\epsilon^2\}$ be minimized.

$$\begin{aligned}
\mathcal{E}\{\epsilon^2\} &= \mathcal{E}\{(\sigma - \sigma_{\text{WF}})(\sigma - \sigma_{\text{WF}})^T\} \\
&= \mathcal{E}\{\sigma\sigma^T - 2\sigma\sigma_{\text{WF}}^T + \sigma_{\text{WF}}\sigma_{\text{WF}}^T\} \\
&= \Sigma_\sigma - 2\mathcal{E}\{\sigma(\sigma^T J^T L^T + n^T L^T)\} + \mathcal{E}\{L(J\sigma(J\sigma)^T + n(J\sigma)^T + J\sigma n^T + nn^T)L^T\} \\
&= \Sigma_\sigma - 2\Sigma_\sigma J^T L^T + L(J\Sigma_\sigma J^T + \Sigma_n)L^T
\end{aligned}$$

This quadratic form has the single minimum

$$\frac{\partial}{\partial L}\mathcal{E}\{\epsilon^2\} = 0 \iff L = \Sigma_\sigma J^T (J\Sigma_\sigma J^T + \Sigma_n)^{-1}.$$

The above expression for L can be rewritten in the form of the MAP regularization factor on V of equation (4.15).

$$\begin{aligned}
L &= (J^T \Sigma_n^{-1} J + \Sigma_\sigma^{-1})^{-1} (J^T \Sigma_n^{-1} J + \Sigma_\sigma^{-1}) \cdot \Sigma_\sigma J^T (J\Sigma_\sigma J^T + \Sigma_n)^{-1} \\
&= (J^T \Sigma_n^{-1} J + \Sigma_\sigma^{-1})^{-1} J^T \Sigma_n^{-1}
\end{aligned}$$

Therefore, the Wiener filter also *selectively* blocks components of the degraded noisy signal based on *a priori* information Σ_σ and Σ_n . To show that, indeed, the MAP estimator and the Wiener filter are equivalent regularization techniques, one can derive H_R from equation (4.15) in the discrete Fourier domain assuming that J is a circulant matrix.

This chapter is closed with the Tikhonov form of the MAP solution from equation (4.15). This form is the basis used to solve the boundary motion and electrode movement problem discussed in the next chapter. Consider the inverse covariances in equation (4.15) written in a weighted matrix form

$$\Sigma_\sigma^{-1} = \frac{1}{w_\sigma^2} R, \quad \Sigma_n^{-1} = \frac{1}{w_n^2} W. \quad (4.17)$$

Substituting these into the MAP estimate yields

$$\begin{aligned}\sigma_{\text{MAP}} &= \left(J^T \frac{1}{w_n^2} W J + \frac{1}{w_\sigma^2} R\right)^{-1} \left(J^T \frac{1}{w_n^2} W V + \frac{1}{w_\sigma^2} R \sigma_{\text{prior}}\right) \\ &= \left(J^T W J + \left(\frac{w_n}{w_\sigma}\right)^2 R\right)^{-1} \left(J^T W V + \left(\frac{w_n}{w_\sigma}\right)^2 R \sigma_{\text{prior}}\right)\end{aligned}$$

The matrix R is weighted by the positive quantity $\lambda^2 = (w_n/w_\sigma)^2$, and they are termed the *regularization matrix* and *hyperparameter*, respectively. The Tikhonov MAP regularization solves the EIT inverse problem (4.14) yielding the estimate σ_{MAP} . This solution is regularized by: *i*) the conductivity distribution *a priori* R and σ_{prior} and *ii*) the noise *a priori* W . The conductivity distribution *a priori* are scaled by the hyperparameter λ , and the estimate is written as

$$\sigma_{\text{MAP}} = (J^T W J + \lambda^2 R)^{-1} (J^T W V + \lambda^2 R \sigma_{\text{prior}}). \quad (4.18)$$

Chapter 5

Image Variability from Boundary Deformation

The variability in EIT images due to the deformation of the medium boundary was simulated and analysed as part of this thesis. A discussion of EIT applications prone to boundary deformation is presented first, with references to the challenges reported in the literature. The second section presents the methods used to simulate and quantify this effect. The third section illustrates and quantifies the simulated effects of deformation on the reconstruction model. Finally, an analysis of the results is discussed in the fourth section.

5.1 Cause and Effect of Boundary Deformation

The literature of medical EIT applications documents the negative effects of reconstructing conductivity distribution imagery with poorly known electrode position. These shortcomings are virtually inevitable when the medium boundary deforms during measurement. In this case, the reconstruction model used to display images roughly approximates the medium boundary and the position of the electrodes.

During the early days of EIT research, it was observed that electrode movement is a significant source of errors and artefacts in images. In order to partially address this issue, EIT *difference* imaging was proposed to reconstruct changes in the conductivity distribution

due to changes in subsequent measurements. Barber & Brown (1998) showed that difference imaging is less sensitive to electrode position uncertainty when the electrodes do not move between measurements. Unfortunately, for medical applications of EIT, the electrodes do move. For example, electrode movement due to chest expansion during breathing and to changes in posture has a significant affect on measurements (Harris *et al.*, 1988), (Adler *et al.*, 1996), (Patterson *et al.*, 2001), and (Coulombe *et al.*, 2005).

The effect of postural changes on EIT measurements has been studied by Harris *et al.* (1988), Lozano *et al.* (1995), and Coulombe *et al.* (2005). In each study, participants were asked to assume different postures between measurements and, consequently, significant differences in EIT images were observed. It was found that, for EIT images of the thorax, the primary cause of electrode movement was due to posture changes and breathing. Frerichs (2000) reported that electrode movement during breathing is caused primarily by the expansion of the rib cage. Simulation studies of this effect were conducted by Adler *et al.* (1996) and by Patterson *et al.* (2001). Finite Element Method (FEM) models of the chest were constructed, and EIT measurements were simulated due to changes in lung conductivity and electrode movement with breathing. Both studies reported a broad central image artefact whose amplitude was proportional to the EIT image due to the conductivity change.

5.2 Simulation Methods

The EIDORS suite was used in the MATLAB (v.14 sp.3) environment on a 32-bit SuSE Linux platform. This section includes the description of the forward and inverse models, the implementation methods of boundary deformation, and the formulation of an image variability figure of merit.

5.2.1 Forward and Inverse Models

The forward model is implemented as an elliptical FEM model with an axis ratio of 1.2 and a 30 cm major axis. The forward model, seen on left side of figures 5.1–5.5, is constructed

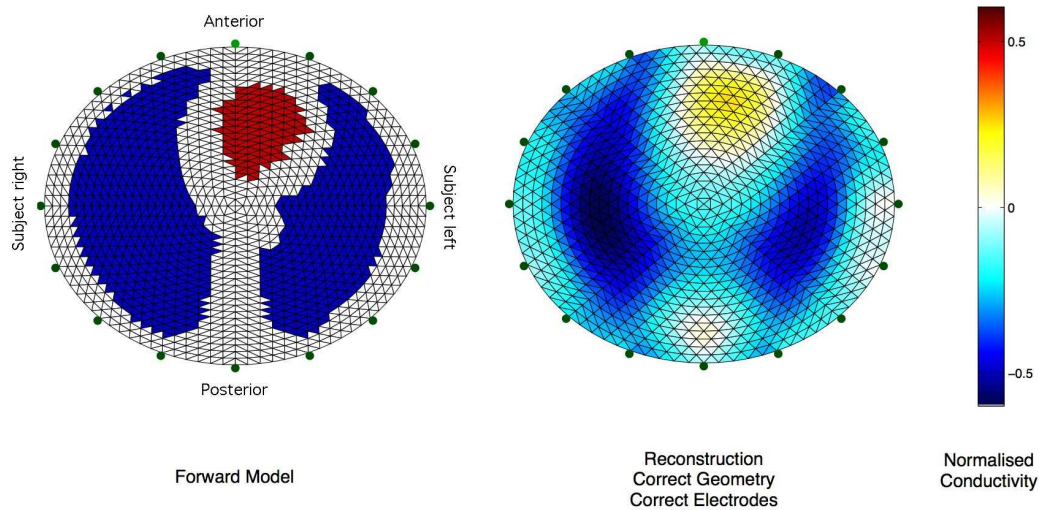


Figure 5.1: *Left:* the 2304 element forward model; a 30 cm major-axis ellipse with 1.2 major/minor axis ratio. *Right:* the reference reconstruction σ_{ref} computed over an inverse model of same boundary and electrode position with 1600 elements ($\lambda = 0.06$).

from 2304 triangular elements. Sixteen nodes on the boundary are selected to represent electrodes with a contact impedance of 200Ω . The elements are associated with a normalized conductivity value; the nodes are associated with voltages referenced to a signal ground (not shown in figures).

The conductivity values are shown as normalized values with respect to the background conductivity, which is set to zero. Inhomogeneities are designed to resemble a typical thoracic measurement. Certain elements are selected to represent lung tissue, shown in blue with normalized conductivity of -0.5 . Other elements represent heart tissue, shown in red with normalized conductivity of $+0.5$. Two inverse models, each with 1600 elements, are used.

1. A 30 cm diameter, circular boundary model with evenly spaced electrodes.
2. An 30 cm major axis, elliptical boundary model with unevenly spaced electrodes.

Both models have their inter-element connectivity pattern rotated by 45° compared to the forward model. Inverse models with a different element layout than the forward model are chosen to avoid the *inverse crime*.

All image reconstructions are computed using the *maximum a posteriori* regularized inverse in equation (4.18) and the forward measurement data. *Additive white Gaussian noise* (AWGN) is injected in the measurement data and modelled by W . The prior σ_{prior} is taken as the mean of the conductivity distribution, and the solution is regularized based on the Laplacian smoothness constraints in R .

5.2.2 Boundary Deformation and Electrode Displacement

The effect of boundary deformation is simulated by using an inverse model with a different boundary than in the forward model. Displaced electrodes are simulated by a tangential translation along the inverse model's boundary, of each electrode.

The simulations test the reconstruction fidelity to the forward model distribution when incorrect inverse models are used. That is, when either boundary deformation or electrode displacement is present.

One reconstruction is made with the first circular inverse model described above, and shown in figure 5.2. In this case, the boundary shape is wrong at the upper and lower ends of the model, but the electrodes are evenly placed, as in the forward problem. The remaining reconstructions are made with the second elliptical inverse model. Reconstructions are calculated with electrode displacements of four size categories: 0.75, 1.50, 2.25 and 3.00 cm. For each category, the selected electrodes are shifted along the boundary with the constraint that they do not cross over neighbouring electrodes, as this would be readily noticeable in practice. Selected electrodes are displaced according to three patterns:

1. a custom pattern where the size and direction of displacement, as well as the number of electrodes selected, are chosen by the user,
2. an *anterior-posterior* pattern where all electrodes on the anterior and posterior semi-circles migrate towards the y -axis, and

3. a *left-right* pattern where all electrodes on the left and right semicircles migrate towards the x -axis.

These erroneous reconstructions are compared to reconstructions made with a correct inverse model, consistent in boundary and electrode position with the forward model.

5.2.3 Analysis of Conductivity Variability

The simulations are analysed numerically and by visual inspection. All reconstructed images are plotted along with the forward model and a normalized conductivity scale. Highly conductive elements are shown in red, while poorly conductive elements are shown in blue. The position of each electrode is shown by a small green disc. The first electrode at the top of the model is shown in a lighter shade of green to track electrodes after large displacements; the other electrodes are numbered clockwise.

Reconstructions are analysed numerically by calculating a global measure of variation in conductivity, relative to the correct inverse model reconstruction. The variation between the incorrectly reconstructed image, with conductivity vector σ_{er} , and the correct reconstruction, with conductivity vector σ_{ref} , is given by the expression

$$\nu_{\sigma} = \frac{\sum_{i=1}^{N_k} |\sigma_{\text{er}}^{[i]} - \sigma_{\text{ref}}^{[i]}|}{\sum_{i=1}^{N_k} |\sigma_{\text{ref}}^{[i]}|}$$

where the denominator does not vanish. The braced superscripts represent the element index, and all N_k elements are summed. The ν_{σ} score is always a non-negative number. Images that resemble each other will have a smaller ν_{σ} value than those with less resemblance. This score is used to compare the variation of conductivity distributions resultant from different severities of electrode displacement.

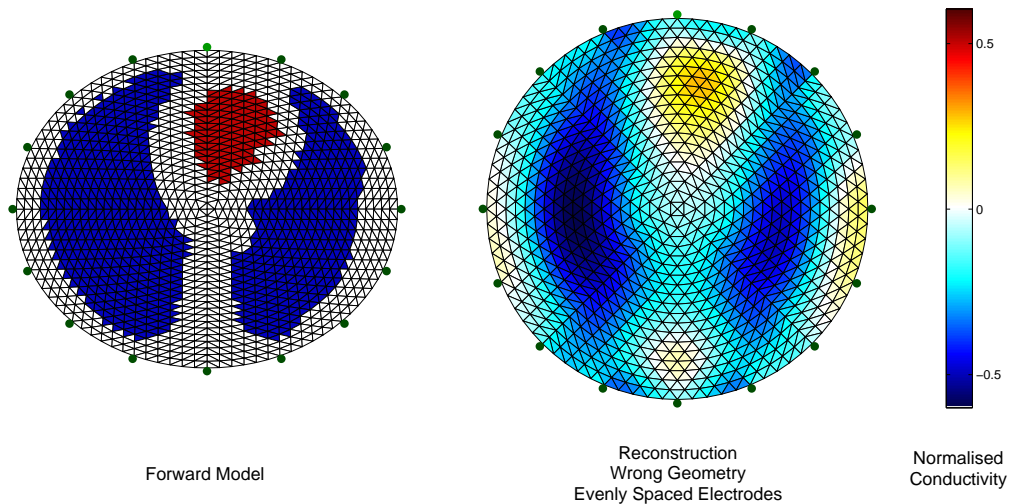


Figure 5.2: Circular, 30 cm diameter, inverse model reconstruction with no electrode displacement ($\lambda = 0.06$).

5.3 Image Reconstructions

The simulation results are illustrated and described below. Figures 5.1, 5.2, and 5.3 are regularized with hyperparameter $\lambda = 0.06$, while figures 5.4 and 5.5 use $\lambda = 0.03$ to compensate for severe distortions due to displacements. The reference reconstruction, computed over a correct inverse model, is shown in figure 5.1. The lung tissue appears to have a larger conductivity magnitude than the heart tissue, since the regularization algorithm gives more significance to larger inhomogeneities.

Figure 5.2 shows a reconstruction over the circular inverse model. The image appears to be stretched along the y -axis, and several small positive artefacts emerge in the posterior, subject-left, and subject-right boundary regions. Also, two pairs of negative artefacts appear to have disjoined the anterior and posterior extremities of the lung tissue and remain near the boundary. The electrodes have not been displaced relative to the FEM structure; however, the circular medium's elements have a slightly different shape than those of the elliptical

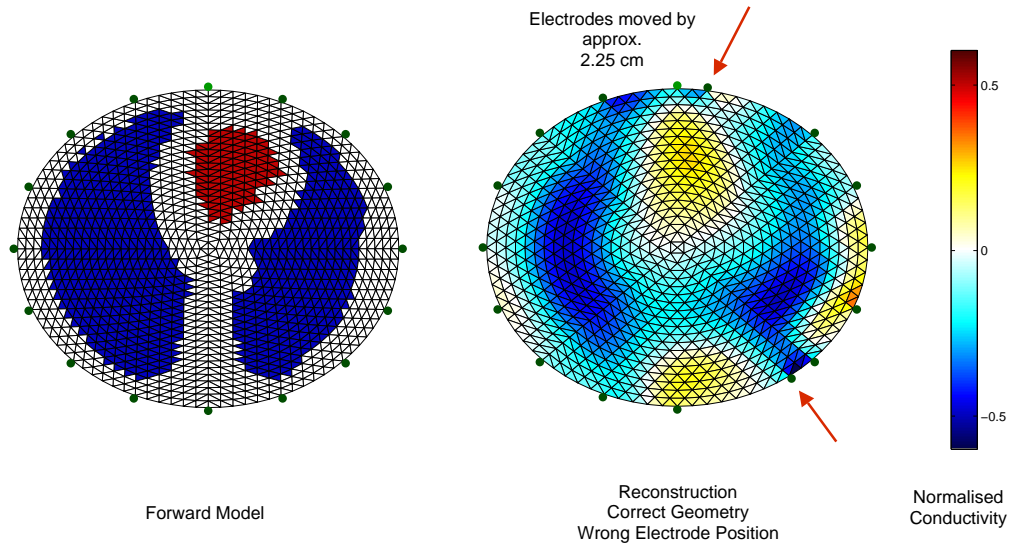


Figure 5.3: Elliptical boundary reconstruction with electrodes 2 and 8 displaced counter clockwise by 2.25 cm ($\lambda = 0.03$).

medium. The resulting conductivity distribution broadens with a larger statistical variance of 0.1362 compared to the reference distribution 0.1088, an increase of approximately 25%.

The following three figures are reconstructions over an inverse model with the correct boundary, but with displaced electrodes. Figure 5.3 shows the effect of two severely misplaced electrodes in the inverse model. Electrodes 2 and 8 are moved by 2.25 cm counter clockwise, and severely affect the reconstruction. The left lungs anterior lobe has strongly deteriorated. Large, positive artefacts appear in the posterior and subject-left boundaries; small, but strong, negative artefacts appear adjacent to the displaced electrodes. The subject-right semicircle remains relatively unaffected by these displacements.

In figures 5.4 and 5.5, all electrodes migrate by 1.50 cm towards the left-right and anterior-posterior directions, respectively. Both reconstructions exhibit severe deformations of the conductivity distribution. Strong contrasts in conductivity concentrate near the poles of migration; whereas, light contrasts in conductivity appear between the largest electrode

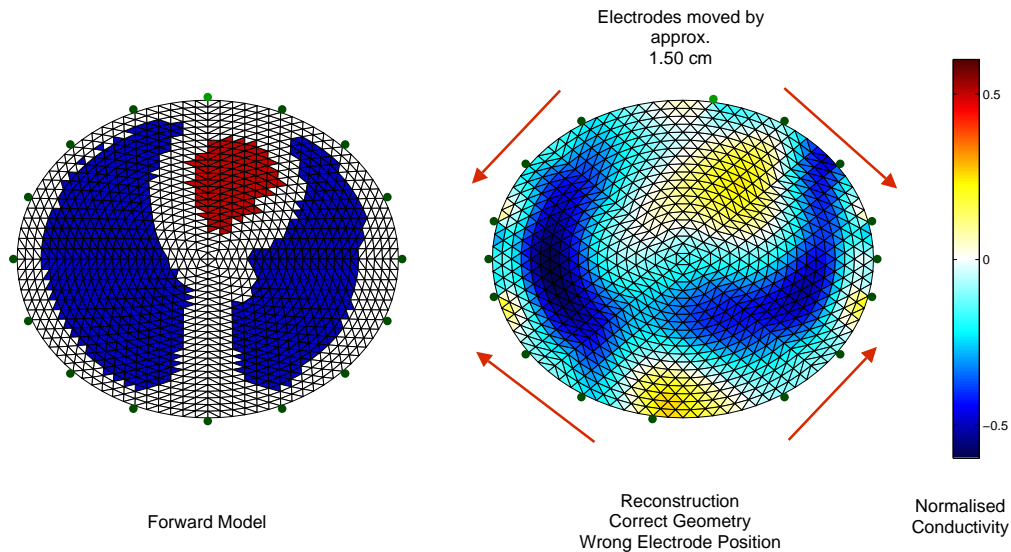


Figure 5.4: Elliptical boundary reconstruction with a 1.50 cm left-right migration of all electrodes ($\lambda = 0.03$).

gaps.

The global variation of the conductivity distribution for a series of reconstructions of electrode displacements is plotted in figure 5.6. A random permutation is made to select which electrodes are to be displaced clockwise. For each size category of displacements (i.e., 0.75, 1.50, 2.25, and 3.00 cm), sixteen reconstructions are calculated, each containing a different number of displaced electrodes. The plot reveals a positive, linear relationship between contrast variation and displacement size. The largest variation occurs in each category when five electrodes are displaced. Variability increases sharply as one to five electrodes are displaced. Beyond five electrodes, the variability steadily decreases towards zero. This is because selected electrodes are displaced by the same quantity in the same direction; thus, as more electrodes are moved together, the global variation returns towards zero and a rotated version of the reconstruction results.

Variations below 5% occur for displacements smaller than 0.75 cm of any number

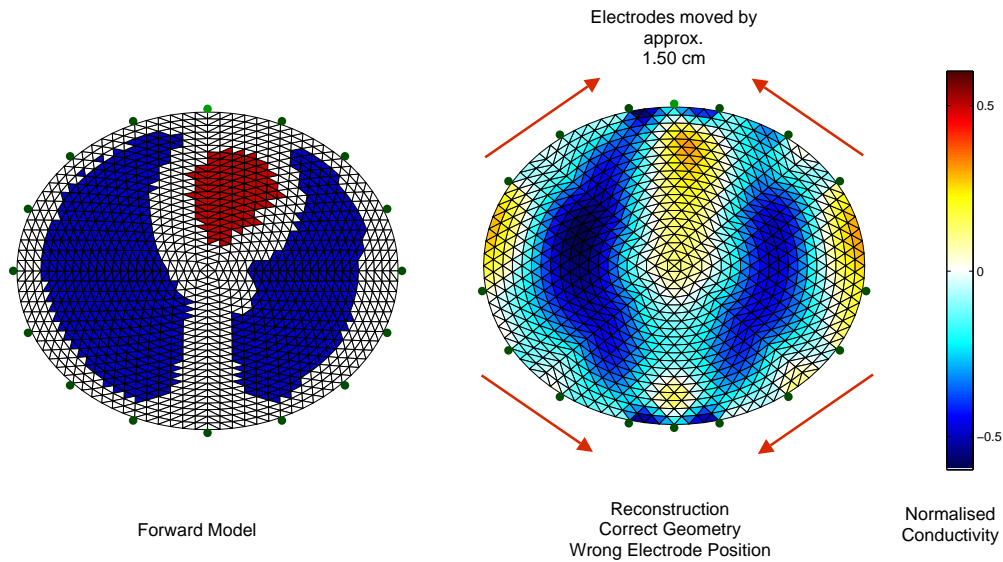


Figure 5.5: Elliptical boundary reconstruction with a 1.50 cm anterior-posterior migration of all electrodes ($\lambda = 0.03$).

of electrodes. The largest variations, of over 20%, occur when four to eight electrodes are displaced by more than 3.00 cm.

5.4 Discussion

Several important observations can be made based on these simulations. First, the effect of incorrect or unknown electrode position in the inverse model negatively influences the reconstructed conductivity distribution. By visual inspection, the effects cause a deterioration of true conductive regions and also produce false conductivity artefacts near the displaced electrodes. Second, the deterioration of these regions depends strongly on the proximity of the displaced electrodes to the inhomogeneous tissue. Electrodes near homogeneous tissue produce fewer artefacts, since only small changes in the potential measurements occur. A further investigation of a local measure of variability around each electrode would explain this effect further.

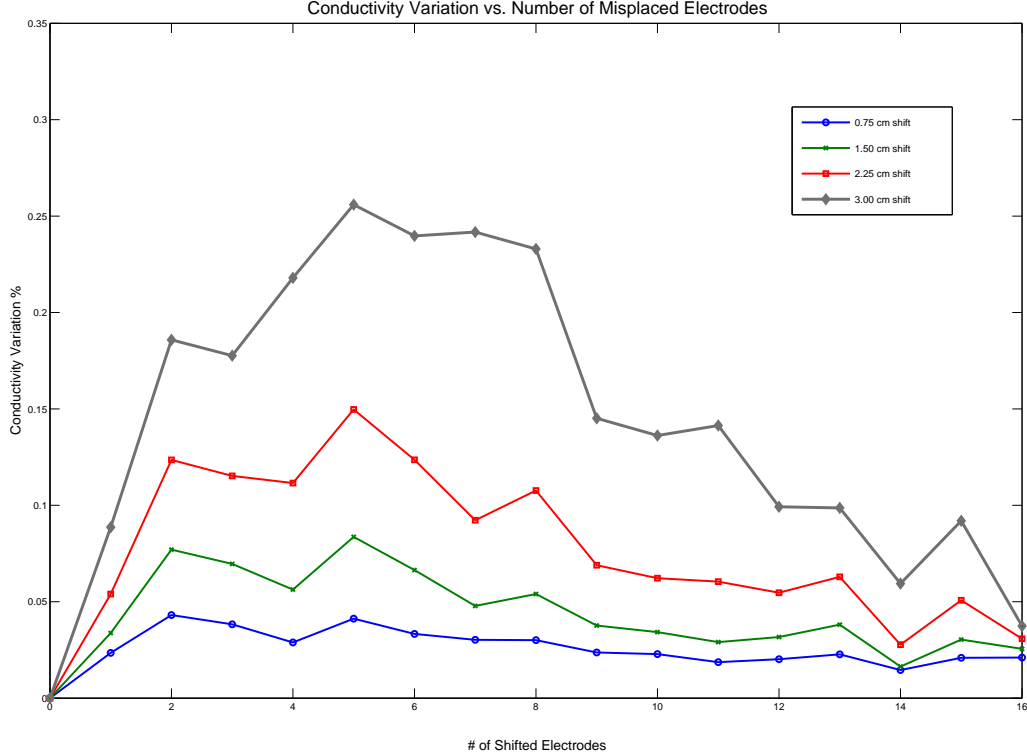


Figure 5.6: Conductivity variation ν_σ versus number of displaced electrodes plotted for four size categories of displacements: 0.75 cm (blue \circ), 1.50 cm (green \times), 2.25 cm (red \square) and 3.00 cm (grey \diamond). All reconstructions used a regularization hyperparameter of $\lambda = 0.03$.

In medical applications involving the EIT of soft tissue, the movement of electrodes during measurement is inevitable due to somatic and involuntary patient motion. Furthermore, the inverse models used in image reconstruction are typically simplified versions of the actual body being measured. Hence, the model only approximates the true electrode positions. Finally, it is expected that the placement of electrodes on the patient is subject to human error. In simulation, we observed that errors between 0.75 cm and 3.00 cm are capable of creating significant variability in the conductivity distribution that can lead to poorly understood images. Interestingly, Harris *et al.* (1988) suggested that image deterioration may be due to changes in distribution of ventilation with posture. The effect of ventilation distribution changes is not refuted in this thesis; however, the simulation results suggest that electrode movement produces a more significant effect.

Electrode movement is also the predominant factor in recent stimulation studies by

Zhang & Patterson (2005). Gersing *et al.* (1996) measured the effect of changes in medium geometry on EIT measurements. Kolehmainen *et al.* (1997) simulated the effect of errors in the boundary model for static imaging using an elliptical deformation of a circular boundary and showed significant errors for boundary model deformation magnitudes of 1% of the medium diameter.

The evidence from the literature strongly indicates significant EIT image reconstruction degradation from boundary deformation and electrode displacement. The simulations computed here confirm this degradation effect by showing that displacements as small as 0.75 cm can produce variations of approximately 5%, and that displacements larger than 1.50 cm introduce variations larger than 10%. These variations are mainly contrasting artefacts near the displaced electrodes and distortions of the conductivity distribution. The following chapter introduces a regularization method developed for this thesis, that augments the standard *maximum a posteriori* solution with electrode position data, to compensate for inter-measurement boundary deformations.

Chapter 6

Electrode Displacement

Regularization

This chapter is the core work of this thesis and builds on all previous material. The thesis objective, addressed in this chapter, is to implement a solution of the deformable media problem of EIT. A Tikhonov regularized, electrode displacement, *maximum a posteriori* (MAP) algorithm that was developed during this research is formulated here; it is referred to as the *proposed algorithm*. A performance analysis of the proposed algorithm is given in the second section, and discussion of the synthesis from this chapter forms the final section.

6.1 Electrode Displacement MAP Algorithm

In a situation where electrodes move, it would be possible to calculate both the conductivity change image and the electrode displacement. Lionheart (1998) showed that, for isotropic conductivity images in three dimensions, such a calculation is theoretically possible. Several groups have proposed algorithms to reconstruct electrode locations or boundary shape (Blott *et al.*, 1998), (Kiber *et al.*, 1990), and (Kolehmainen *et al.*, 2005). These approaches model the boundary in two dimensions, and iteratively fit the model parameters to the measurement data. This section develops a new algorithm to reconstruct both the conductivity change image and the electrode displacement from difference EIT measurement data. The

reconstruction problem is formulated in terms of a regularized inverse, in which an augmented Jacobian, sensitive to conductivity variation and electrode position, is computed.

6.1.1 System model

The algorithm is based on a Finite Element Method (FEM) model of a conductive medium discretized into N_k elements onto which N_e electrodes are attached on the FEM boundary. An adjacent excitation current and voltage difference measurement protocol is applied to obtain N_v independent measurements forming each frame. For difference EIT, voltage measurements V_{t_1} and V_{t_2} , each of length $[N_v]$, are acquired at frames t_1 and t_2 , respectively. Based on these frames, the difference measurement data are calculated and represented by a vector \mathbf{v} such that

$$\mathbf{v}_{t_1} = V_{t_2} - V_{t_1}.$$

Using this notation, we have N_k elements with conductivity vectors σ_{t_1} and σ_{t_2} of length $[N_k]$ taken at frames t_1 and t_2 , respectively. We write the conductivity change image $\Delta\sigma$ as

$$\Delta\sigma_{t_1} = \sigma_{t_2} - \sigma_{t_1}.$$

In this model, it is assumed that the difference measurement data \mathbf{v}_{t_i} depends only on the conductivity change image $\Delta\sigma_{t_i}$ of the current frame. The Complete Electrode Model (CEM) is used for many-node electrodes in 3D models, and the *point electrode model* (PEM) is used for single-node electrodes in 2D models. In each case, the electrodes are represented by nodes on the FEM boundary. The displacement of electrode E_j between frames t_1 and t_2 is described by the position vector

$$\mathbf{r}_{t_1}^j = \mathbf{i}(x_{t_2}^j - x_{t_1}^j) + \mathbf{j}(y_{t_2}^j - y_{t_1}^j) + \mathbf{k}(z_{t_2}^j - z_{t_1}^j)$$

where (x^j, y^j, z^j) represents the node coordinates of electrode E_j at the given frame. Based on the difference measurement data \mathbf{v} , we attempt to reconstruct an *image* written as the

FEM model	N_k	N_p	N_e	N_v	system matrix
Planar	576	313	16	104	A_α
Volumetric	828	252	32	464	A

Table 6.1: Finite element model parameters used in the forward problem.

vector $\mathbf{x} = [\sigma \mathbf{r}]^T$ of length $[N_k + 3N_e]$, which represents the conductivity change image and the electrode displacement between successive frames. Note that this requires that we rewrite \mathbf{r} as a single column vector of length $[3N_e]$ rather than in the triplet form. The first N_k entries represent the conductivity change image $\Delta\sigma$ for each element. The remaining $3N_e$ entries represent the displacement \mathbf{r} for each electrode. In two dimensions, there are only two Cartesian axes; therefore, \mathbf{x} has length $[N_k + 2N_e]$. In general, given the dimension N_d of the FEM, \mathbf{x} has length $[N_k + N_d N_e]$.

6.1.2 Forward calculations

We represent the forward solution as the computation of difference measurement data \mathbf{v} , from the conductivity change image and the electrode displacement \mathbf{x} . This is modelled by the EIT difference operator G based on the FEM and relative to a homogeneous conductivity image σ_h at t_1 . This is represented as

$$\mathbf{v} = G(\mathbf{x})|_{\sigma_h}.$$

The FEM model parameters used in the forward problem are described in table 6.1. The system matrices are implemented based on equation (4.10) for the CEM, and by the PEM model used by Adler & Guardo (1996). The forward calculations are computed based on the following pseudocode algorithm using EIDORS:

1. Create the EIDORS forward model object

```
f_obj = eidors_obj();
```

2. Solve homogeneous forward problem

```
sigma(:) = 1;
```

```
vh = fwd_solve( f_obj, sigma );
```

3. Simulate node movements from boundary deformation

```
new_node_coord = old_node_coord + move;
```

4. Solve inhomogeneous forward problem

```
sigma = conduct_image;
vi = fwd_solve( f_obj, sigma, new_node_coord );
```

5. Simulate additive noise

```
vi = vi + noise;
```

6. Take voltage difference

```
dv = vi - vh;
```

6.1.3 Inverse calculations

The inverse solution is derived from the regularized MAP framework using the Gaussian priors in equation (4.15). The inverse calculations are modified to account for electrode displacement. The Jacobian of G is assembled as two submatrices such that

$$J = [J_\sigma \ J_E] \quad (6.1)$$

where J_σ , of size $[N_v \times N_k]$, is calculated by the perturbation method based on equations (4.12) and (4.13) for 3D models. The submatrix J_E , of size $[N_v \times N_d N_e]$, is the sensitivity from electrode displacement, and written as

$$J_E = \begin{bmatrix} \frac{\partial V_1}{\partial E_1} & \cdots & \frac{\partial V_1}{\partial E_{N_d N_e}} \\ \vdots & \vdots & \vdots \\ \frac{\partial V_{N_v}}{\partial E_1} & \cdots & \frac{\partial V_{N_v}}{\partial E_{N_d N_e}} \end{bmatrix}$$

where $\partial E_{N_d N_e}$ represents an infinitesimal movement of electrode N_e along dimension N_d . Each element $[J_E]^{ij}$ represents the ratio of a change in measurement i for a small change in finite element j . This portion of the Jacobian is calculated using the simpler perturbation method based on $\mathbf{r} \rightarrow \mathbf{r} + \Delta \mathbf{r}$. In 2D models, the Jacobian is calculated from the perturbation

of the image $\mathbf{x} \rightarrow \mathbf{x} + \Delta\mathbf{x}$, where $\Delta\mathbf{x}$ is chosen to be sufficiently large to avoid numerical errors, but small enough that it accurately approximates the Jacobian. Thus, each element $[J]^{ij}$ is formulated by the forward problem taken from measurement i on element j such that

$$[J]^{ij} = \frac{G_i(\mathbf{x}_j + \Delta\mathbf{x}_j)}{\Delta\mathbf{x}_j}.$$

In order to validate the choice of $\Delta\mathbf{x}$, the change in the Jacobian as a function of $\Delta\mathbf{x}$ is evaluated. For calculations with double precision arithmetic, the relative variation is less than 10^{-6} for $\Delta\mathbf{x} = 10^{-6}$. The Jacobian is used as the linear approximation from equation (4.11); except we augment $\sigma \rightarrow \mathbf{x}$.

The regularized MAP framework using Gaussian priors from equation (4.15) is written here as

$$\mathbf{x}_{\text{MAP}} = (J^T \Sigma_n^{-1} J + \Sigma_{\mathbf{x}}^{-1})^{-1} (J^T \Sigma_n^{-1} V + \Sigma_{\mathbf{x}}^{-1} \mathbf{x}_{\text{prior}}). \quad (6.2)$$

The conductivity change image and the electrode displacement are assumed to be as likely positive or negative. Therefore, we choose to provide no *a priori* bias, i.e., $\mathbf{x}_{\text{prior}}$ is set to 0. The matrices $\Sigma_{\mathbf{x}}$ and Σ_n are the *a priori* covariance estimates of the image and measurement noise, respectively. The *a priori* noise is assumed to be an additive white Gaussian (AWGN) process. This assumption is made to simplify the analysis; it is the ideal case where electrode signals are independent. Furthermore, choosing a constant weight w_n means that the noise amplitude is equal across channels. Therefore, the noise vector $n \in \mathbb{R}^{N_v}$ has the statistical properties that $\mathcal{E}\{n\} = 0$ and $\mathcal{E}\{n n^T\} = \Sigma_n = w_n I$, where Σ_n is the covariance matrix of n , w_n is a scaling factor of the noise amplitude, and I is the identity matrix. Thus, the *a priori* image and noise covariances are modelled such that

$$\Sigma_{\mathbf{x}} = \mathcal{E}\{\mathbf{x}^2\}, \quad \Sigma_n = w_n I.$$

Hence, $[\Sigma_n]^{ii}$ can be thought of as the relative noise power for measurement i . Unnecessary computation is avoided by computing matrices R and W to represent $\Sigma_{\mathbf{x}}^{-1}$ and Σ_n^{-1} , respectively. Similar to the Jacobian in equation (6.1), the *a priori* image R is formed by two

submatrices such that

$$R = \begin{bmatrix} R'_\sigma & 0 \\ 0 & R'_E \end{bmatrix} \quad (6.3)$$

where R'_σ , of size $[N_k \times N_k]$, is the conductivity change image covariance, and R'_E , of size $[N_d N_e \times N_d N_e]$, is the electrode displacement covariance. The conductivity and displacement components are assumed to be uncorrelated; therefore, the cross-covariance of σ and \mathbf{r} is zero. For specific applications of EIT, such as for lung imaging, the conductivity change image may be correlated to the electrode displacements. However, in general, to impose such *a priori* information on the algorithm may introduce image artefacts when such correlations do not hold. Since this algorithm is not only applied to breathing data, uncorrelated priors is a reasonable choice. Based on these assumptions, the image covariance is modelled as

$$\Sigma_{\mathbf{x}}^{-1} = \frac{1}{w_\sigma^2} R_\sigma + \frac{1}{w_E^2} R_E$$

where w_σ and w_E represent the *a priori* amplitude of conductivity change image and electrode displacement, respectively. Note that R_σ and R_E are padded by zeros such that they both have size $[(N_k + N_d N_e) \times (N_k + N_d N_e)]$ and can be added to achieve equation (6.3). That is,

$$R_\sigma = \begin{bmatrix} R'_\sigma & 0 \\ 0 & 0 \end{bmatrix}, \quad R_E = \begin{bmatrix} 0 & 0 \\ 0 & R'_E \end{bmatrix}.$$

In order to model the expected smoothness of actual conductivity change images, R'_σ should be a spatial high pass filter (Adler & Guardo, 1996). The inter-element conductivity correlation is modelled using a discrete Laplacian filter, so that the diagonal elements $[R'_\sigma]^{ii} = N_d + 1$. The off-diagonal elements $[R'_\sigma]^{ij}$ are set to -1 if finite elements i and j are adjacent, i.e., share at least N_d nodes, and are otherwise set to zero. Within the electrode displacement model R'_E , it is again reasonable to expect a non-zero inter-element correlation; because as the boundary deforms smoothly, the adjacent electrodes may be expected to move similarly. The inter-element displacement correlation is also modelled using a discrete Laplacian filter,

with the diagonal elements $[R'_E]^{ii}$ set to 2.1. Hence, the off-diagonal elements $[R'_E]^{ij}$ are set to -1 for adjacent electrodes i and j . In order to impose a non-zero penalty for global displacement of all electrodes, $[R'_E]^{ii} = 2.1$ is chosen rather than 2. Since the *a priori* amplitudes w_σ and w_E are measured in different units, they may be of different orders of magnitude. Consequently, $\mu = w_\sigma/w_E$ is defined as the displacement hyperparameter to represent the compromise between model fidelity to the conductivity change image or electrode displacement.

The Tikhonov regularized MAP solution from equation (4.18) is implemented by applying the model formulated above in equations (6.1) and (6.3) to the MAP expression in equation (6.2).

$$\mathbf{x}_{\text{MAP}} = \left(J^T \frac{1}{w_n^2} W J + \frac{1}{w_\sigma^2} R_\sigma + \frac{1}{w_E^2} R_E \right)^{-1} J^T \frac{1}{w_n^2} W \mathbf{v} \quad (6.4)$$

The regularization matrix R_μ is defined in terms of μ^2 as

$$R_\mu = R_\sigma + \mu^2 R_E. \quad (6.5)$$

Now equation (6.4) can be rewritten in terms of the Tikhonov hyperparameter $\lambda^2 = w_n^2/w_E^2$ and the displacement hyperparameter $\mu^2 = w_\sigma^2/w_E^2$. From equations (6.1) and (6.3), an augmented linear inverse solution for the conductivity change image and electrode displacement $\mathbf{x}_{\lambda\mu}$ is obtained using the hyperparameters λ and μ . Given the measurement data \mathbf{v} , the inverse solution of the proposed algorithm is

$$\begin{aligned} \mathbf{x}_{\lambda\mu} &= \left(J^T W J + \frac{w_n^2}{w_\sigma^2} R_\sigma + \frac{w_n^2}{w_E^2} R_E \right)^{-1} J^T W \mathbf{v} \\ &= \left(J^T J + \lambda^2 (R_\sigma + \mu^2 R_E) \right)^{-1} J^T \mathbf{v} \\ &= \left(J^T J + \lambda^2 R_\mu \right)^{-1} J^T \mathbf{v}. \end{aligned} \quad (6.6)$$

From equation (6.5), the regularization matrix R_μ is defined element-wise in terms of the

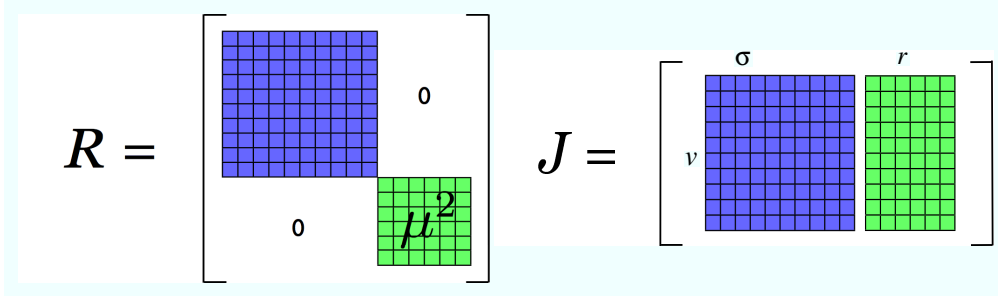


Figure 6.1: The regularization matrix R is assembled from two sub-matrices quantifying the inter-element conductivity correlation, or the inter-electrode displacement correlation. The electrode displacement correlation sub-matrix is scaled by the displacement hyperparameter μ^2 . The Jacobian matrix J is assembled similarly from sub-matrices quantifying the boundary voltage \mathbf{v} versus the conductivity distribution σ and the electrode displacements \mathbf{r} .

displacement hyperparameter μ as follows

$$[R_\mu]^{ij} = \begin{cases} N_d + 1 & \text{if } i = j, \text{ and } i \leq N_k \\ -1 & \text{if element } i \text{ is adjacent to } j, \text{ and } i \leq N_k \\ 2.1\mu^2 & \text{if } i = j, \text{ and } i > N_k \\ -\mu^2 & \text{if electrode } i \text{ is adjacent to } j, \text{ and } i > N_k \\ 0 & \text{otherwise.} \end{cases}$$

Figure 6.1 illustrates how R and J were implemented in the algorithm. The regularization matrix is composed of two sub-matrices. The upper-left sub-matrix quantifies the correlation between neighbouring elements, and the lower-right sub-matrix correlates neighbouring electrodes and is scaled by the displacement hyperparameter. Since no element-electrode correlations are modelled, the off-diagonal sub-matrices are zero. The Jacobian is also composed of two sub-matrices, each quantifying the boundary voltage sensitivity. Each element of the left sub-matrix is the change of a particular measurement v for a small change of conductivity σ in a particular element. The right sub-matrix is the change in v for a small displacement of an electrode along one of the axes. These sensitivities are calculated by using a homogeneous conductivity distribution σ_h and by perturbing either the element or the electrode corresponding to the matrix element value that is to be calculated.

6.1.4 Artefact amplitude measure

The reconstruction algorithm from equation (4.18), which does not calculate electrode displacement is referred as the *standard algorithm*. Images reconstructed with electrode movement compensated by the proposed algorithm appear to show reduced artefacts resulting from boundary deformation in comparison with the standard algorithm. To measure this effect, a *measure of reconstruction artefact amplitude* (AAM) is defined as follows. A reconstruction artefact is defined to be an element of non-zero conductivity variation, which is known *a priori* from the physical or simulation model. The AAM is defined by the expression

$$\text{AAM} \triangleq \sqrt{\frac{\sum_{i \in L} \Omega_i \mathbf{x}_i^2}{\sum_{i \in L} \Omega_i}}$$

where $\Omega_i \subset \Omega$ is the volume or area of element i , and L is a subset of elements selected. For simulated results, L includes all elements which do not overlap with any contrast element in the forward model. For phantom measurement data, L is defined to include elements in the two rings of finite elements closest to the boundary because this is the typical region where deformation artefacts occur.

6.2 Performance Analysis

The performance of the standard and the proposed algorithms is measured using three figures of merit that consider the image characteristics of the reconstructed conductivity change image. These are applied to a 2D, unit radius, circular FEM model containing a single conductivity contrast whose position varies radially inside the medium. The key functions of the software code used to generate these figures and results is printed in the second section of appendix C entitled “Performance Analysis”.

1. The *position error* measures the discrepancy of the contrast centre between the forward model and the inverse model images. This determines whether the algorithm shifts or warps the geometry of the conductivity change image. The *position error* was defined

by Adler & Guardo (1996).

2. The *blur radius* measures the radius of the disk, centred on the contrast, that encircles elements containing half of the total image intensity. The *blur radius* was defined by Adler & Guardo (1996). An overview of methods for the measurement of spatial resolution in 2D circular EIT images was presented by Wheeler *et al.* (2002).
3. The *artefact amplitude measure*, defined in section 6.1.4, is also used on the single contrast model after applying an elliptical deformation to the circular boundary.

The performance analysis routine begins with a contrast in the centre of the medium, corresponding to origin of the medium radius. The three figures of merit are applied and the analysis is repeated with the contrast repositioned at every 0.10 unit increments of the medium radius until the boundary is reached. This routine is repeated for hyperparameter values of $\lambda \in \{10^{-6}, 10^{-5}, \dots, 10^{-1}\}$ and $\mu \in \{1, 10\}$. Both algorithms produce nearly identical position error values. Results are only slightly affected by varying the contrast radial position; hence, the following figures show results for a fixed contrast placed along the 0.50 radial position. It is observed that image properties only vary slightly in function of μ , since these figures of merit examine the conductivity change image and not the electrode movements. Hence, the fixed value $\mu = 1$ is used for the following figures.

A comparison of blur radius results is shown in figure 6.2. The blur radius for different deformation magnitudes between 0–1% of the medium diameter are computed using the proposed algorithm. The standard algorithm could not reproduce the contrast due to strong deformation artefacts. Without deformation, the standard and proposed algorithms have the same blur radius. As deformation is introduced, the proposed algorithm's blur radius steadily increases until it can no longer reconstruct the contrast. Figure 6.3 illustrates the results comparing the standard (solid curve) and the proposed movement (dash-dot curve) algorithms for two cases of regularization. The left plot shows the slightly under-regularized case, using hyperparameter $\lambda = 5 * 10^{-4}$, where both algorithms behave similarly and incur large artefacts as the deformation progresses beyond 1–2%. The proposed algorithm always

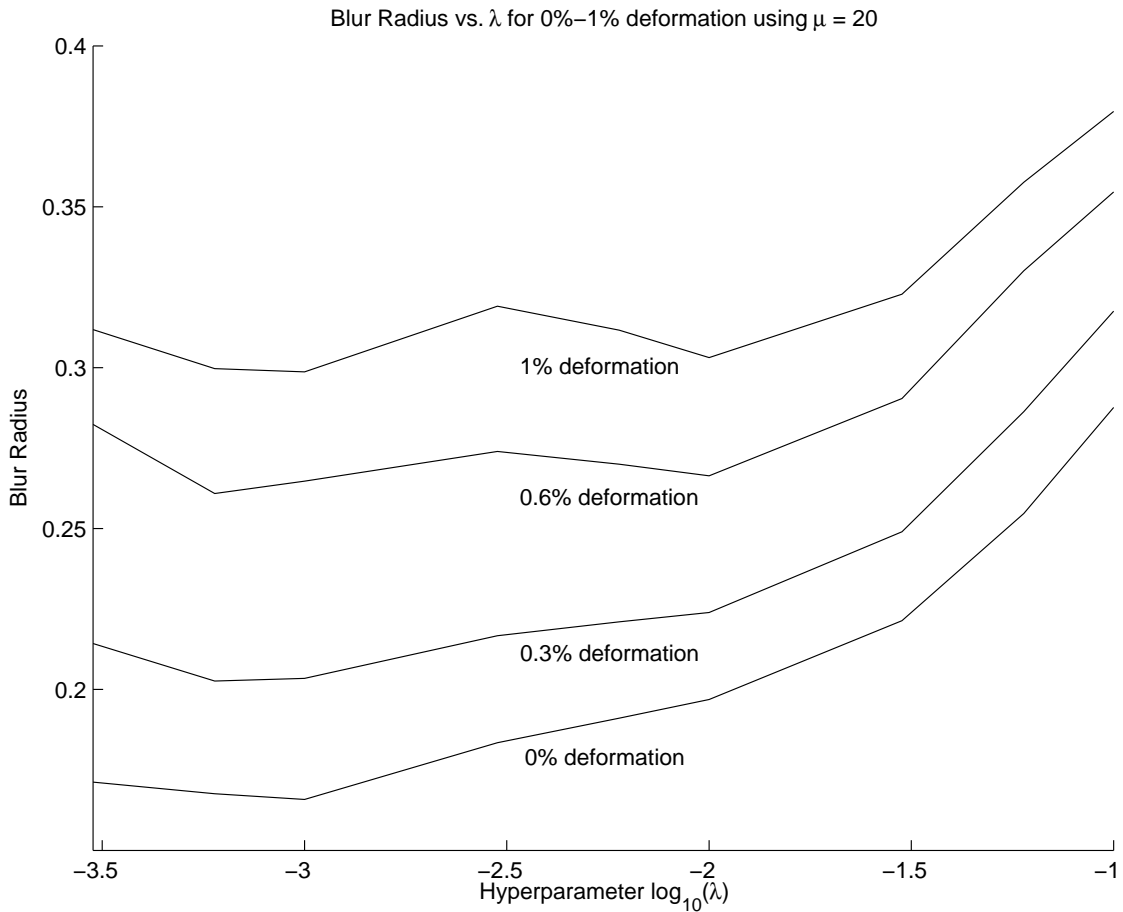


Figure 6.2: Plot of the blur radius, for deformations ranging between 0–1% of medium diameter, versus hyperparameter $\lambda \in \{5 * 10^{-3}, \dots, 10^{-1}\}$ with the proposed algorithm. The forward problem is a small contrast half way along the radius of a circular model.

has a marginally lower AAM. The right plot shows the AAM results corresponding to a reasonably regularized image using hyperparameter $\lambda = 10^{-2}$. The proposed algorithm is more tolerant to boundary deformations and has a much lower AAM than the standard algorithm. The convexity of the proposed curve indicates that its AAM value begins to rise quickly beyond 10% deformations. Figure 6.4 illustrates the AAM gain factor. This represents the reduction of the proposed algorithm’s AAM, relative to the standard algorithm’s AAM. For example, at 5% deformation the proposed algorithm’s AAM is approximately 0.6 the value of the standard algorithm’s AAM. The gain factor is given by the ratio $(AAM_s - AAM_p)/AAM_s$ where s and p refer to the standard and the proposed algorithms, respectively. It is calculated for each hyperparameter value $\{10^{-6}, \dots, 10^{-1}\}$ and the average gain is plotted versus the deformation magnitude. This figure shows that the proposed algorithm performs best over

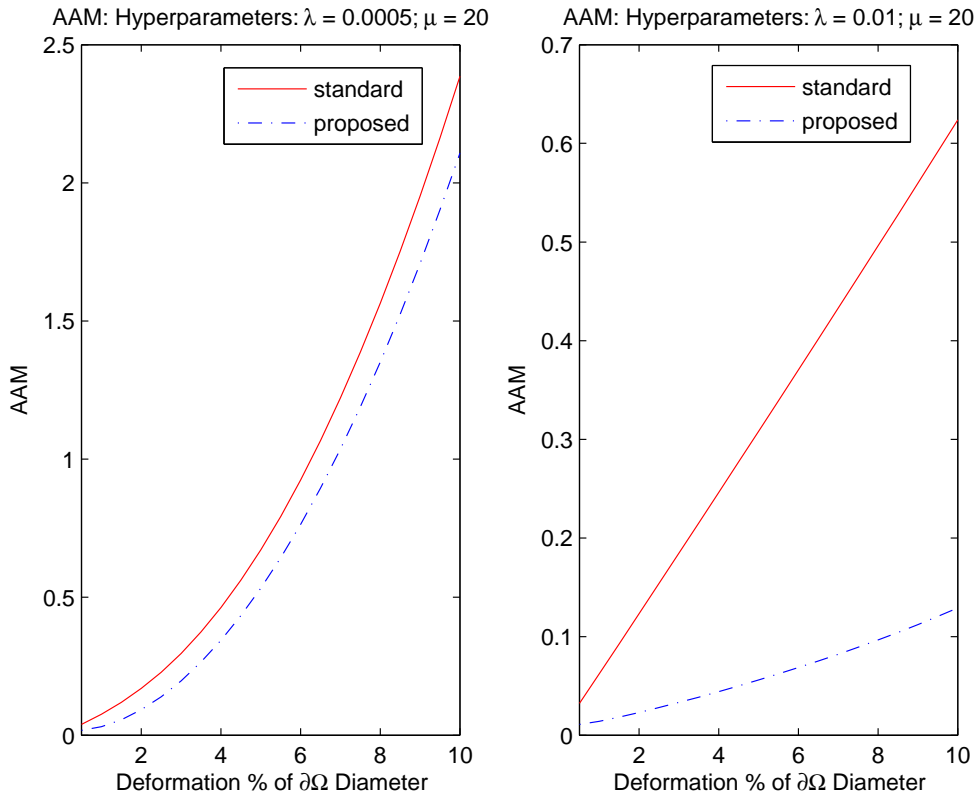


Figure 6.3: AAM plots versus deformation for standard (solid) and proposed (dash-dot) algorithms. Both plots use $\mu = 1$ and show AAM for deformations ranging from 0.5–10% of medium diameter. The forward problem is a small contrast half way along the radius of a circular model. *Left:* under-regularized solution with $\lambda = 5 * 10^{-4}$. *Right:* reasonably regularized solution with $\lambda = 10^{-2}$.

the standard algorithm in terms of artefact reduction.

6.3 Discussion

One of the main challenges in applications of EIT is compensating for image artefacts due to the uncertainty of electrode position. This chapter proposes a Tikhonov regularized, electrode displacement MAP algorithm to reconstruct both the conductivity change image and electrode displacement from difference EIT measurement data. Several groups have attempted to model the boundary shape from EIT measurements. Kiber *et al.* (1990) showed a way to estimate the shape of the boundary from electrical data using a two-dimensional model. Good results were reported for an elliptical tank and some success on data from a thorax. Blott *et al.* (1998) and Kolehmainen *et al.* (2005) developed algorithms to compensate for electrode

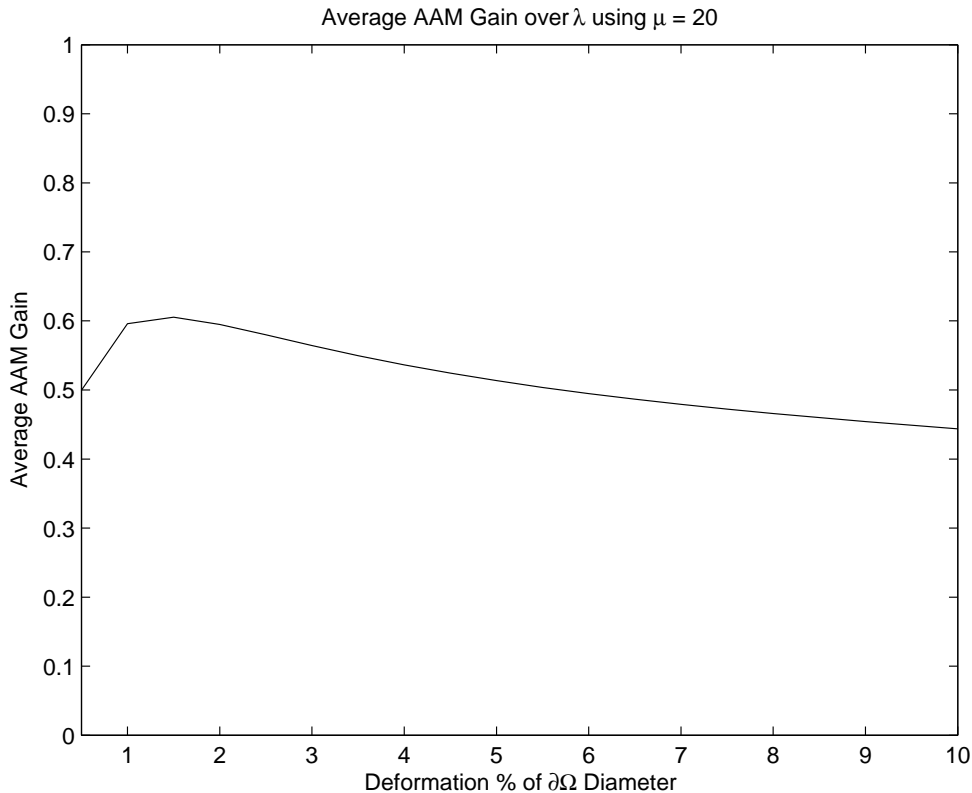


Figure 6.4: AAM gain factor averaged over hyperparameter values $\lambda \in \{10^{-6}, \dots, 10^{-1}\}$ and plotted versus deformation. The forward problem is a small contrast half way along the radius of a circular model.

position variations based on a perturbation of the Jacobian similar to that presented here. A regularized expression was developed and iteratively solved for the conductivity changes and electrode movements. This work differs from the algorithm proposed here, in that electrode displacement was not directly modelled as spatial coordinates, and only 2D simulations were presented.

The performance analysis, comparing the proposed and the standard algorithms, show that the proposed algorithm is better equipped to image deformable media. Even in the under-regularized case, the proposed algorithm maintains a lower AAM value. In this analysis, the proposed algorithm's AAM is 50–80% smaller than the standard algorithm's AAM for deformations between 0.5–10% of the medium diameter. Also, the proposed algorithm also produces a marginally smaller blur radius. The calculations require 10 ms per frame after the Jacobian is precalculated. Hence, the system described is suitable for real-time EIT

imaging of processes up to a highest frequency component of 500 Hz.

An important theoretical result was given by Lionheart (1998) who showed that, if the boundary shape is wrong in a 3D model, there will not generally be an isotropic conductivity which will fit the measured boundary data. Recall that anisotropic conductivity violates one of the main assumptions of the EIT inverse problem in section 4.1. Thus, in theory, both conductivity and correct boundary shape can be calculated from EIT measurement data. For 2D models, isotropic conductivity and boundary shape can be recovered up to a conformal mapping relation, i.e., only a smaller set of deformations can be correctly recovered.

The proposed algorithm, however, imposes limitations to the results. This study uses fixed electrode models, in which all nodes for each electrode translate uniformly, without distortion or rotation. However, real electrode displacements are far more complex. The electrode will turn as it moves, the skin under it will buckle, and the electrode itself may deform. Perhaps the performance differences observed from simulations and from phantom data are partially a result of this simplification. Moreover, boundary deformation is modelled by node displacement in the FEM. Thus, as the boundary is deformed, the element structure of the FEM changes and also modifies the measurement data. In this study, deformations on the order of 0.5–10% of the medium diameter are considered. However, for larger deformations, this model is expected to incur FEM-related artefacts. Finally, the result by Lionheart (1998) applied to this study is limited by the fact that difference measurement data are considered, and a limited number of electrode displacements, rather than complete boundary data, are available.

In addition to boundary deformation and electrode displacement, changes of electrode contact impedance are a significant issue in EIT applications, especially for monitoring applications (Lozano, 1997). While this is not considered here, it is interesting to note the approach taken by Heikkinen *et al.* (2002) that executed simultaneous reconstructions of the conductivity change image and electrode contact impedances. Similar to this work, a composite Jacobian was calculated based on changes in both parameters. Perhaps an improvement to the proposed algorithm would be the modelling of electrode impedance in this

way. Additionally, it may be possible to reconstruct the overall distortion of the boundary as well as the displacement of the electrodes.

Another valuable study is the development of equipment-specific noise models. This work models the noise as an AWGN process that has equal gain and SNR across electrode channels. EIT equipment, in general, may however produce correlated noise signals across channels, each with different gain and SNR. Moreover, the noise may not be ergodic. Such generalizations would complicate the calculation of the MAP solution, since equation (6.2) would not be valid and more effort would be required to calculate the posterior probability distribution.

Electrode displacement is a difficult problem to simulate. Since the discretization of the physical problem introduces assumptions and limits the validity of this model, the author feels that a demonstration of experimental results is also necessary to ensure this method is not only applicable to simulated data. Hence, this method is also tested on simulated, phantom, and *in vivo* measurement data for 2D and 3D media.

Chapter 7

Imaging of Deformable Media

This chapter presents the data acquired during this research and applies the proposed algorithm developed in this thesis. The first section describes the acquired EIT measurement data from simulation, phantom, and *in vivo* experiments. The second section presents the reconstructed conductivity change images of these data. The final section discusses the results concerning the material from this chapter.

7.1 Acquired EIT Data

EIT measurement data were acquired by numerical simulation, phantom experiments using a saline tank, and *in vivo* experiment. The measurement data from physical experiments were acquired by the Goe-MF II EIT instrument (Viasys Healthcare, Höchberg, Germany). A complete record of these experiments is found in appendix A.

Numerical simulations were conducted using 2D and 3D Finite Element Method (FEM) models in EIDORS, described in table 6.1. The methods of generating the measurement data are outlined in the forward calculations in section 6.1.2. The measurement data V_{t_1} are calculated for a homogeneous circular medium with conductivity σ_h , and V_{t_2} are calculated for a medium with two small inhomogeneities of conductivity $1.2 \times \sigma_h$ and $0.8 \times \sigma_h$. Between frames t_1 and t_2 the boundary is distorted into an elliptical shape with a 1% elongation vertically and a 1% compression horizontally. Additive white Gaussian noise

(AWGN) is added to measurements to give a signal-to-noise ratio (SNR) of 20 dB, with the signal defined as $\|\mathbf{v}\|^2$.

Saline phantom measurement data were acquired from a 30 cm diameter, 30 cm tall, cylindrical phantom, filled with 0.9% saline solution to the 20 cm mark. A similar phantom is shown in figure 7.1. Sixteen stainless steel electrodes were placed, equally spaced, around the circumference at a vertical position of 10 cm above the base of the tank. EIT measurement data were acquired using the adjacent excitation and measurement protocol. Measurement data \mathbf{v}_h from a homogeneous conductivity image were first acquired, and subsequently, small non-conductive spherical objects, of 2 cm radius, were introduced in the plane of the electrodes at various positions along the x and y axes. Electrode displacement was simulated by applying an elliptical deformation to the phantom such that the diameter of the top of the phantom on the x -axis was reduced by 5 cm. The electrode channel impedances were measured between 200–400 Ω according to the system’s calibration test, which considered these within the system’s acceptable limits.

The *in vivo* measurement data were acquired from one normal male subject. Research ethics approval was obtained (University of Ottawa research ethics certification file *H 05-04-02*). Seventeen (16 signal + 1 ground) Ag/AgCl ECG electrodes (Blue Sensor, Ambu+, Denmark) were placed on the thorax after the skin was prepped with isopropanol. All measurements were taken while the subject was supine. Two electrode placement strategies were used where the reference electrode was placed on the right side of the subject’s waist line.

1. Single plane, 16 electrodes aligned with the fifth rib directly below the nipple. Electrode 1 is in the centre of the sternum. The other electrodes are labelled moving towards the subject’s right side so that electrode 5 is under the right armpit, electrode 9 is on the spine, and electrode 13 is under the left armpit.
2. Two planes of 8 electrodes each. The upper plane is vertically aligned with the fifth rib directly below the nipple and the lower plane with the seventh rib directly below the nipple. Electrode 1 is on the upper plane in the centre of the sternum. Electrode 2



Figure 7.1: Saline plastic phantom (30 cm diameter; 30 cm height) with sixteen electrodes over two rings.

is on the lower plane but shifted to the right by half the inter-electrode distance of the upper plane. The other electrodes are labelled in a zigzag pattern, moving towards the subject's right side.

For each strategy, three breathing patterns were measured: *tidal breathing*, *residual capacity to total lung capacity* (TLC/RC), and *paradoxical breathing*. Tidal breathing are relaxed, normal breaths. The residual and total lung capacities are the minimum and maximum quantities of air the subject can contain in the lungs. Paradoxical breathing is when a fixed quantity of air is moved from the upper-thorax (by rib expansion) to the lower-thorax (by diaphragm yield), i.e, the subject is not really breathing. These patterns were repeated for the subject in a rest state (heart rate ≈ 60 bpm) and a stress state (heart rate ≈ 90 bpm).

7.2 Reconstructed Conductivity Images

Conductivity change images from the standard and the proposed algorithms are reconstructed in this section. The reconstructions are implemented in MATLAB (v.14 SP3) and tested using a Linux computer equipped with a 2.60 GHz, 32-bit AMD Opteron CPU. The calculation of the complete reconstruction of the 3D problem took 25.2 seconds, while the computation of an inverse solution required approximately 10 milliseconds. The key functions of the software code used to generate these results are printed in the first section of appendix C entitled "Electrode Displacement".

7.2.1 Simulated Reconstructions

Simulated 2D measurement data are generated using the circular FEM model shown in the top left part of figure 7.2. The conductivity change image is coloured with the blue-red spectrum shown to the right of the image. Each electrode is indicated by a green disk at the centre of the electrode position. Arrows indicate each electrode's displacement, and are scaled by 20. The top right part of figure 7.2 is an image reconstructed from these measurement data using the standard method with $\lambda = 10^{-2}$. The images reconstructed using the

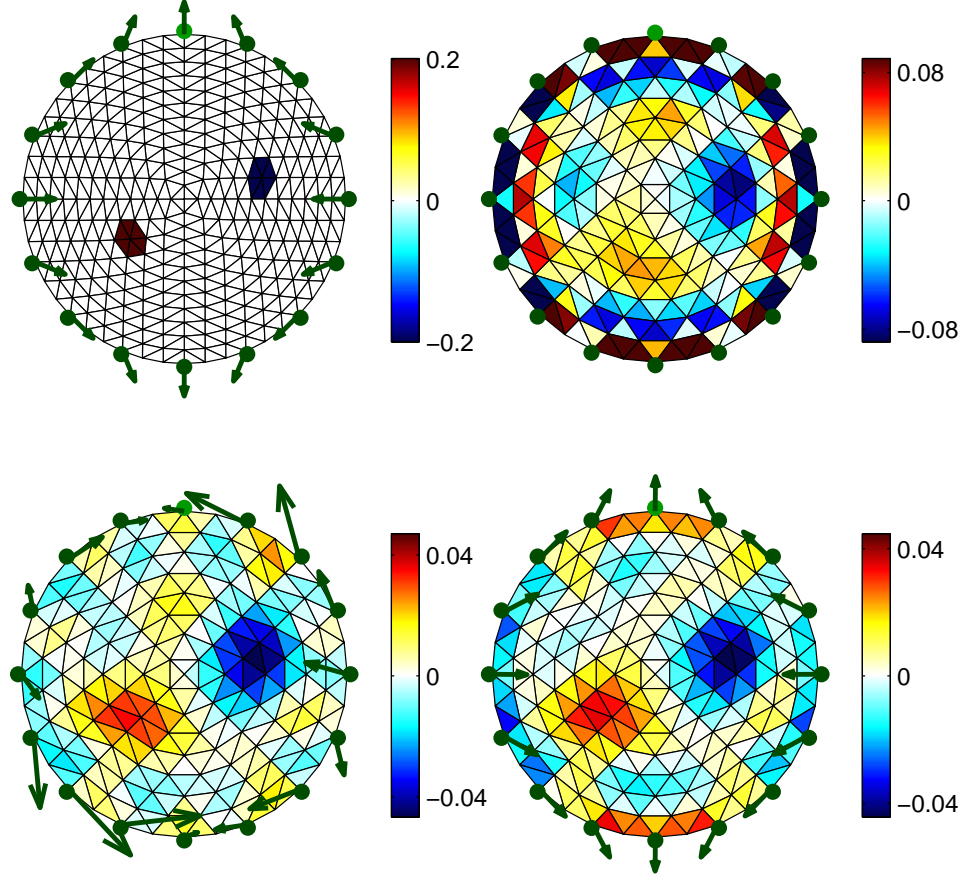


Figure 7.2: Simulated images of reconstructed conductivity change image and electrode displacement. Arrows indicate each electrode’s displacement, and are scaled by 20. *Top left:* 2D FEM ($N_k = 576$) for simulation of conductivity change image and electrode displacement from an elliptical deformation of 1% of medium diameter. AWGN of 20 dB SNR is added to simulated measurement data. *Top right:* reconstructed image ($N_k = 256$) using the standard algorithm with $\lambda = 10^{-2}$ (AAM = 0.0616). *Bottom left:* reconstructed image using the proposed algorithm with $\lambda = 10^{-2}$ and $\mu = 1$ (AAM = 0.0116). *Bottom right:* reconstructed image using the proposed algorithm using $\lambda = 10^{-2}$ and $\mu = 20$ (AAM = 0.0135).

standard method show a large level of artefacts around the medium boundary, as well as an incorrect position for the reconstructed contrasts, which appear to be pushed in the direction of boundary movement. Images reconstructed using the proposed algorithm, in the bottom row of figure 7.2, show dramatically reduced artefacts as well as more accurate contrast position. When μ is small, the penalty for movements is low, and the algorithm is able to make arbitrary electrode movements to satisfy the conductivity change constraints. This is observed in the bottom-left corner of figure 7.2 where $\mu = 1$. For this simulation, conductivity change images are expected to vary on the order of $1.0 \times \sigma_h$. Electrode displacements have

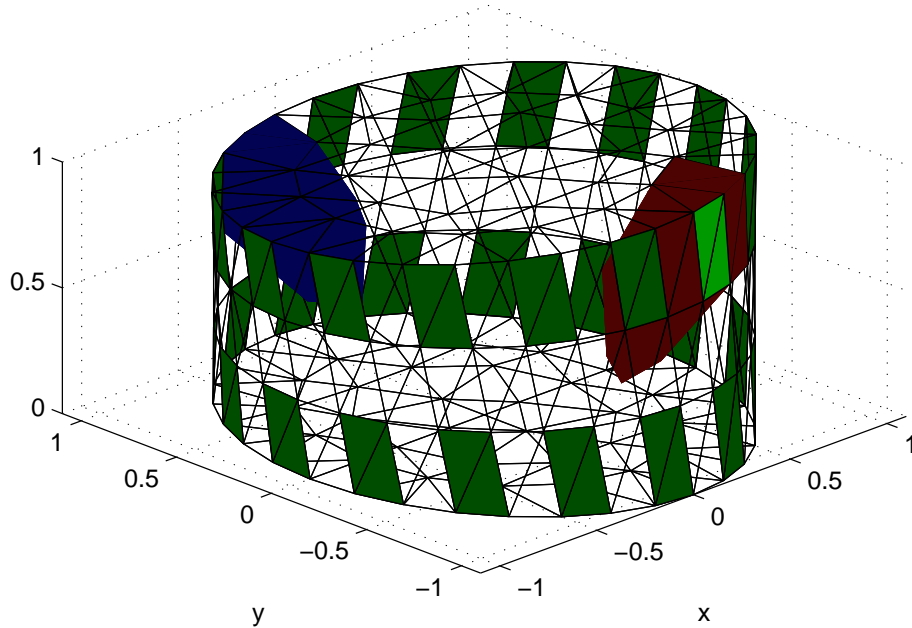


Figure 7.3: 3D FEM ($N_k = 828$) with two rings of 16 electrodes shown in green. The FEM incurs a geometrical distortion (exaggerated 10 times to clarify the geometry). Blue and red regions indicate contrasts being less conductive and more conductive, respectively, than the surrounding medium.

a magnitude of 5% of the medium diameter. Therefore, an estimate of $\mu = 1/0.05 = 20$ is reasonable. Using this value, $\mu = 20$, the image in the bottom-right corner of figure 7.2 shows a better reconstruction of conductivity and displacement. The Artefact Amplitude Measure (AAM) of the proposed algorithm with $\mu = 20$ is reduced by 78% compared to the standard algorithm. Note however, for specific experimental measurements, estimating μ correctly requires *a priori* knowledge of expected conductivity variations and boundary deformation. An analytical selection criterion, based on the work by Graham & Adler (2006b), for this parameter would be a useful improvement.

In order to test this method on 3D reconstructions, simulations are calculated using the cylindrical FEM model shown in figure 7.3. Difference measurement data are calculated due to the introduction of conductive and non-conductive contrasts and a complex 3D distortion. Reconstructed conductivity change images and electrode displacement are shown from

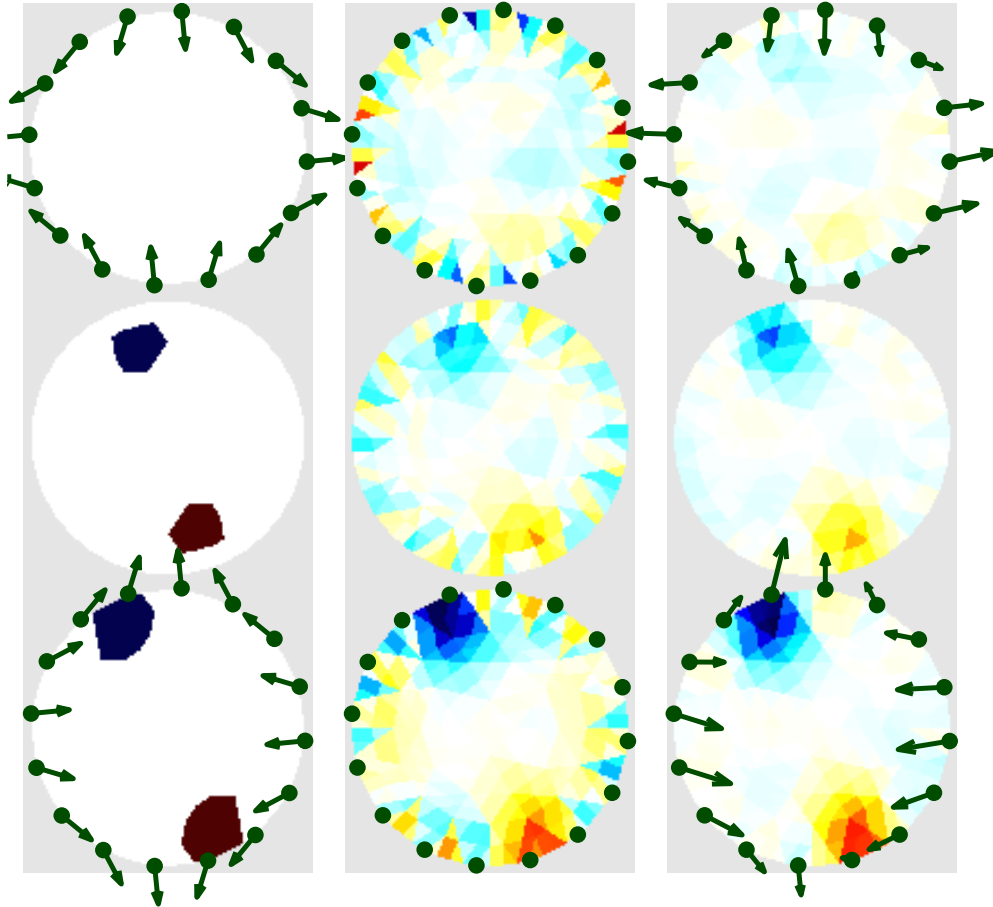


Figure 7.4: Reconstructed images and electrode displacement from simulated 3D measurement data with 20 dB SNR noise, using hyperparameters $\lambda = 3 \times 10^{-3}$ and $\mu = 20$. Each column shows three horizontal slices of the reconstructed image on a volumetric FEM ($N_k = 828$; top: $z = 0.167$; middle: $z = 0.500$; bottom: $z = 0.833$). Electrodes are indicated by green disks at the centre of their positions. Arrows indicate each electrode's displacement, and are scaled by 10. *Left:* simulated inhomogeneities and electrode displacement. *Middle:* reconstructed image using the standard algorithm (AAM = 0.0708). *Right:* reconstructed image using the proposed algorithm (AAM = 0.0190).

simulated 3D measurement data with 20 dB SNR noise, using hyperparameters $\lambda = 3 \times 10^{-3}$ and $\mu = 20$. The figure is divided into three columns. Each column shows a slice of the medium parallel to the z -axis. Conductivity change images and electrode displacement are represented as in figure 7.2, except that arrows are scaled by 10. The forward model, the standard algorithm result, and the proposed algorithm result are shown in the left, middle, and right columns, respectively. Images reconstructed from this FEM are shown in figure 7.4, using the standard algorithm and the proposed algorithm. The proposed algorithm is able to calculate electrode displacement, and it is also able to significantly reduce the level

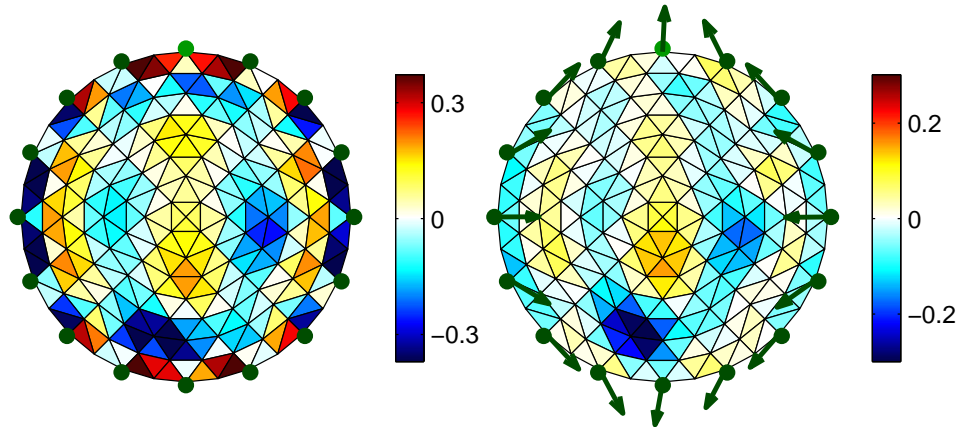


Figure 7.5: Reconstructed images ($N_k = 256$) for phantom measurement data with two non-conductive objects: one on the positive x -axis, the other on the negative y -axis. Arrows indicate each electrode's movement, and are scaled by 10. *Left:* reconstructed image with standard algorithm using $\lambda = 10^{-2}$ (AAM = 0.134). *Right:* reconstructed image with the proposed algorithm using $\lambda = 10^{-2}$ and $\mu = 10$ (AAM = 0.0273).

of image reconstruction artefacts. The proposed algorithm's AAM is 73% smaller than the standard algorithm's AAM.

7.2.2 Phantom Reconstructions

Reconstructed images for phantom measurement data are shown in figure 7.5. The phantom contained two non-conductive objects: one on the positive x -axis, the other on the negative y -axis. The phantom was compressed along the x -axis by 5 cm at the top of the tank. Since electrodes were placed at $1/3$ of the tank height, each electrode moved by 6.7% of the tank radius. The calculated displacements shown in figure 7.5, however, indicate the distortion was $2/3$ smaller. The contrasts are reconstructed at the correct locations in both the proposed and the standard algorithms, although artefacts in the standard algorithm are significantly larger. The proposed algorithm's AAM is 80% smaller than the standard algorithm's AAM. The used EIT instrument is capable of capturing 750 frames per second. The algorithm is applied to a breathing simulation of 60 seconds during which a series of elliptical boundary deformations were progressively introduced and relaxed as per experimental records in appendix A. Two contrasts were located inside the phantom at the positive x and negative y axes. Figure 7.6

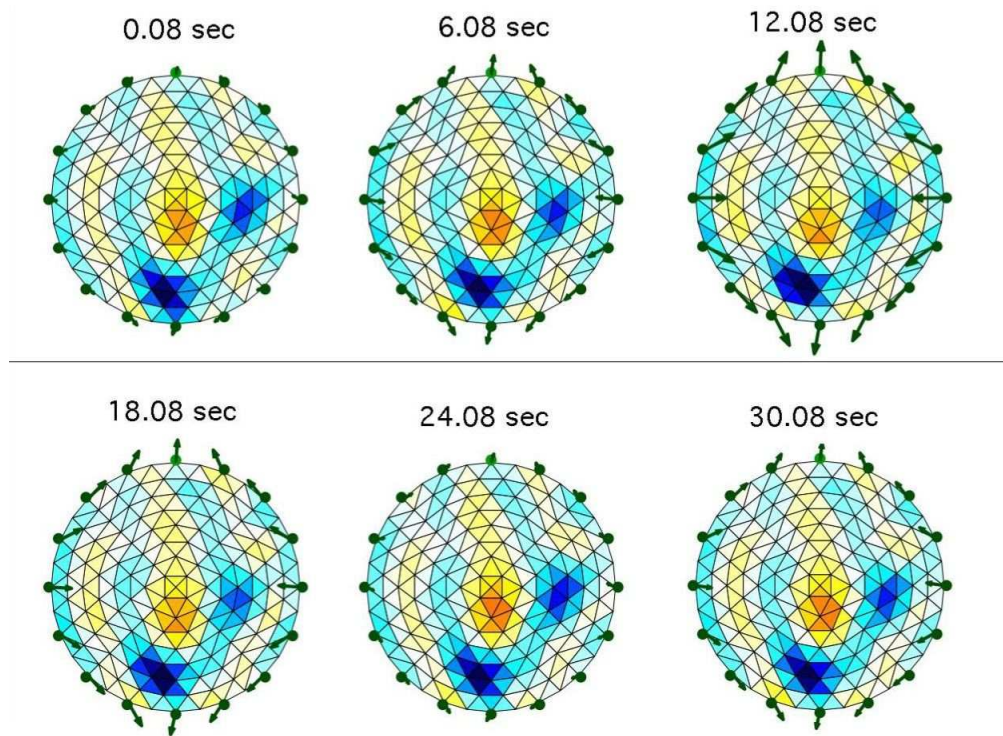


Figure 7.6: Reconstructed images ($N_k = 256$) for phantom measurement data with two non-conductive objects on the positive x and negative y axes. Arrows indicate each electrode's movement, and are scaled by 10. Frames shown are sampled in 6 second intervals. The phantom is progressively deformed and relaxed ten times sequentially over 60 seconds.

shows six reconstructed frames, beginning at 0.08 seconds in increments of 6.00 seconds, of simulated breathing deformations. Electrode displacements are correctly recovered using a single hyperparameter pair $\lambda = 10^{-2}$ and $\mu = 20$.

7.2.3 In Vivo Reconstructions

The three *in vivo* breathing patterns are imaged ($N_k = 256$) over 60 second measurement intervals for the rest and stress states. The details of the experiment are recorded in the second section of appendix A entitled “In Vivo Experiment”. All reconstructed images have a scaling factor of 20 on electrode displacement arrows. Figure 7.7 shows a time series, in increments of 0.56 seconds, of tidal breathing in the rest state. The top, bottom, left, and right of each image corresponds to the anterior, posterior, subject-left, and subject-right. This applies to all *in vivo* reconstructions presented. The hyperparameters chosen are $\lambda = 3 \times 10^{-2}$ and $\mu = 5$. Since the breathing is quiet, boundary deformation and conductivity changes are both small. Consequently, a small displacement hyperparameter leads to reasonable electrode displacements. The conductivity change image is difficult to interpret and the lung regions are not very clear. However, breathing patterns are visible, since a rhythmic alternation of blue patterns (i.e., inspiration) and red patterns (i.e., expiration) are observed. Also, the reconstructed electrode displacements agree with the recorded respiration frequency and with the “inspiration at start of measurement” convention. Figure 7.8 shows a similar time series, also in increments of 0.56 seconds, of the repeated measurement while the subject is in a stress state. The same hyperparameters are used to reconstruct the EIT data. The image reconstructions show higher conductivity changes and electrode displacement, indicating the heavier breathing of the subject. The time series of images also show the accelerated respiratory rate. The lung regions are visible, particularly during inspiration where the right lung, i.e., the larger lung, is best recognized. Electrode displacements are reconstructed with reasonable direction; however, adjacent electrode displacements appear to have significantly differing magnitudes. This is visible in the inspiration frames.

The TLC/RC and paradoxical breathing patterns exhibit larger electrode displace-

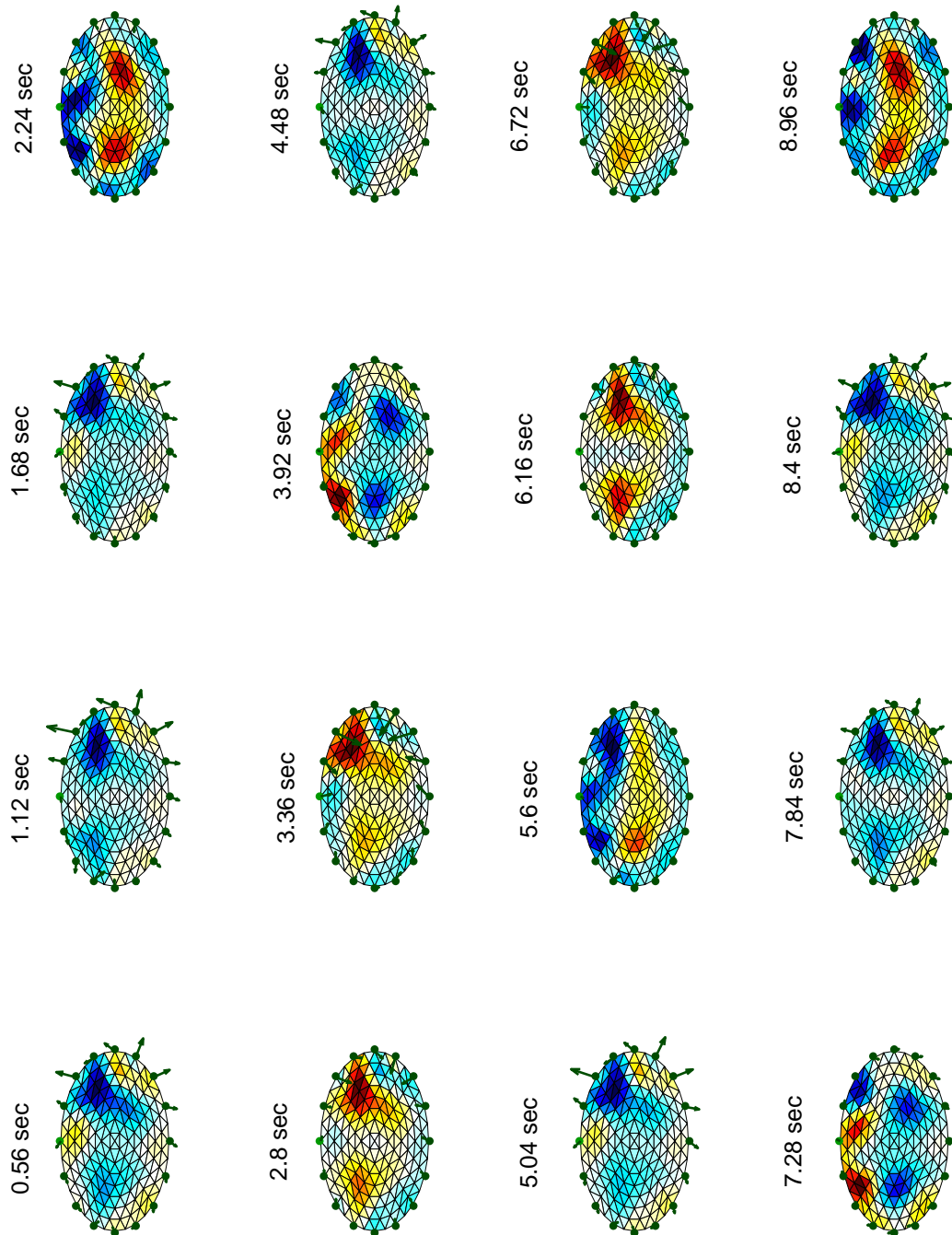


Figure 7.7: Tidal breathing in rest state. Time series of 16 images with 0.56 second increments. The hyperparameters used are $\lambda = 3 \times 10^{-2}$ and $\mu = 5$. Electrode displacements are scaled by $20\times$.

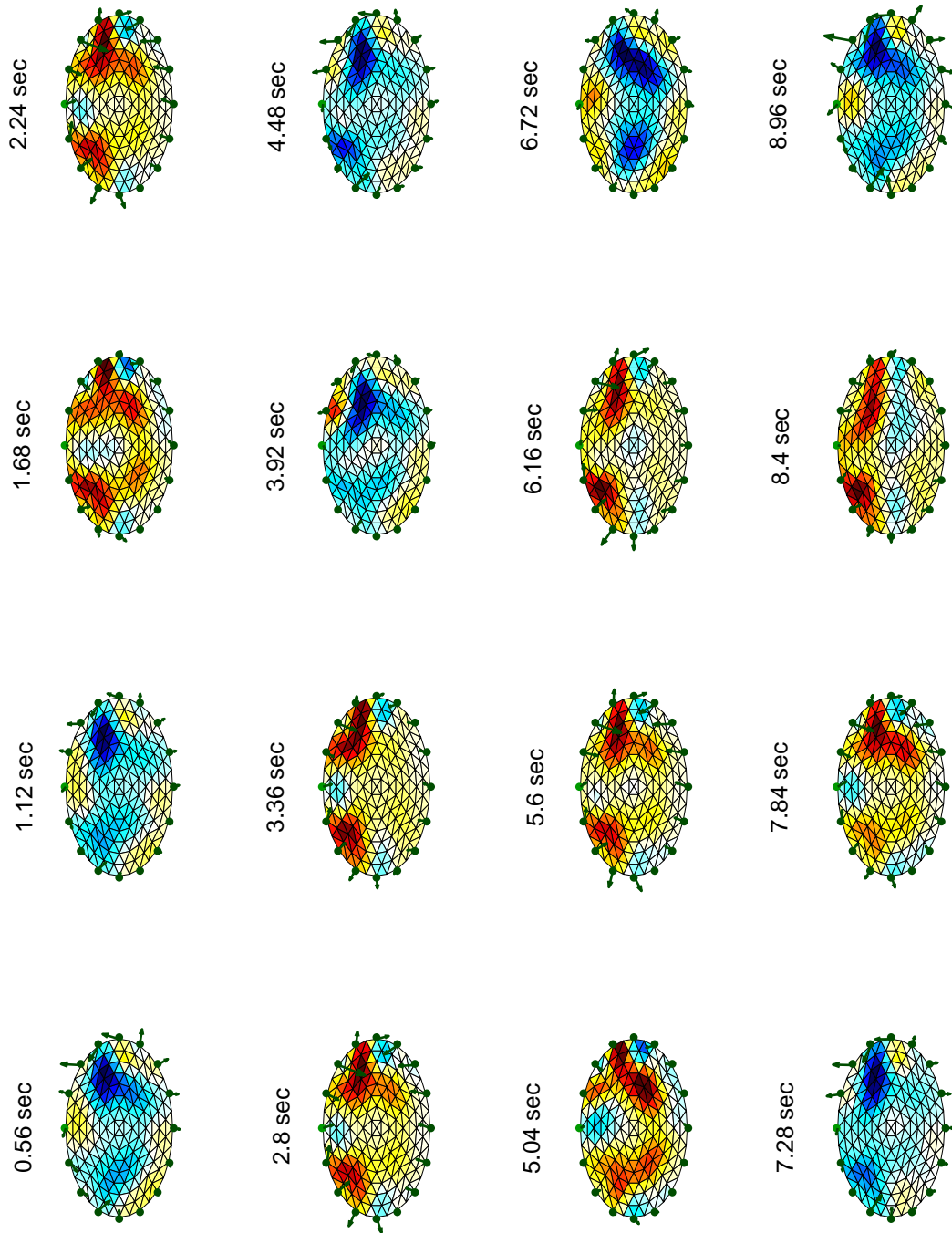


Figure 7.8: Tidal breathing in stress state. Time series of 16 images with 0.56 second increments. The hyperparameters used are $\lambda = 3 \times 10^{-2}$ and $\mu = 5$. Electrode displacements are scaled by 20.

ments than tidal breathing due to the maximum voluntary rib cage expansion by the subject. Correspondingly, reconstructions are shown with a larger displacement hyperparameter of $\mu = 40$ for TLC/RC and $\mu = 20$ for paradoxical breathing. Figures 7.9 and 7.10 show a time series, in increments of 1.20 seconds, for TLC/RC in the rest and stress states, respectively. The breathing patterns and lung regions are clearly recognized, and few artefacts are visible. The electrode displacements are also well structured and correspond with the recorded respiration frequency and conventions used in the experiment. Perhaps these indicate the performance limits of the algorithm when facing large deformations as those shown in figure 6.3. It is interesting to note the better performance of the proposed algorithm using TLC/RC data. Perhaps the weaker conductivity and displacement fluctuations seen in the tidal breathing data indicate the equipment's sensitivity limitations. Figures 7.11 and 7.12 show a time series, also in increments of 1.20 seconds, for paradoxical breathing in the rest and stress states, respectively. The conductivity change images and electrode displacements illustrate this different breathing pattern. Large electrode displacements are observed during rib cage expansion and contraction that correspond to the recorded respiratory frequency in experiment. However, the conductivity changes during inspiration are located in central region of the medium, rather than in the expected anterior region. Furthermore, the increasing conductivity pattern, usually seen during expiration, is not consistent between different phases of the series. This may be indicative of the non-communicating air held in the lungs while the rib cage and the diaphragm deform. Perhaps this variability suggests the difficulty of breathing this way; the subject was not able to perform this manoeuvre consistently.

7.3 Discussion

The proposed algorithm demonstrates the ability to reconstruct conductivity change images and electrode displacement in simulation, phantom, and *in vivo* experiment. Furthermore, the artefacts due to boundary deformation are significantly reduced in all cases. Simulated 2D and 3D data reconstructions performed best, since the data and the injected noise was well known. The algorithm demonstrates the ability to accurately reconstruct images in all

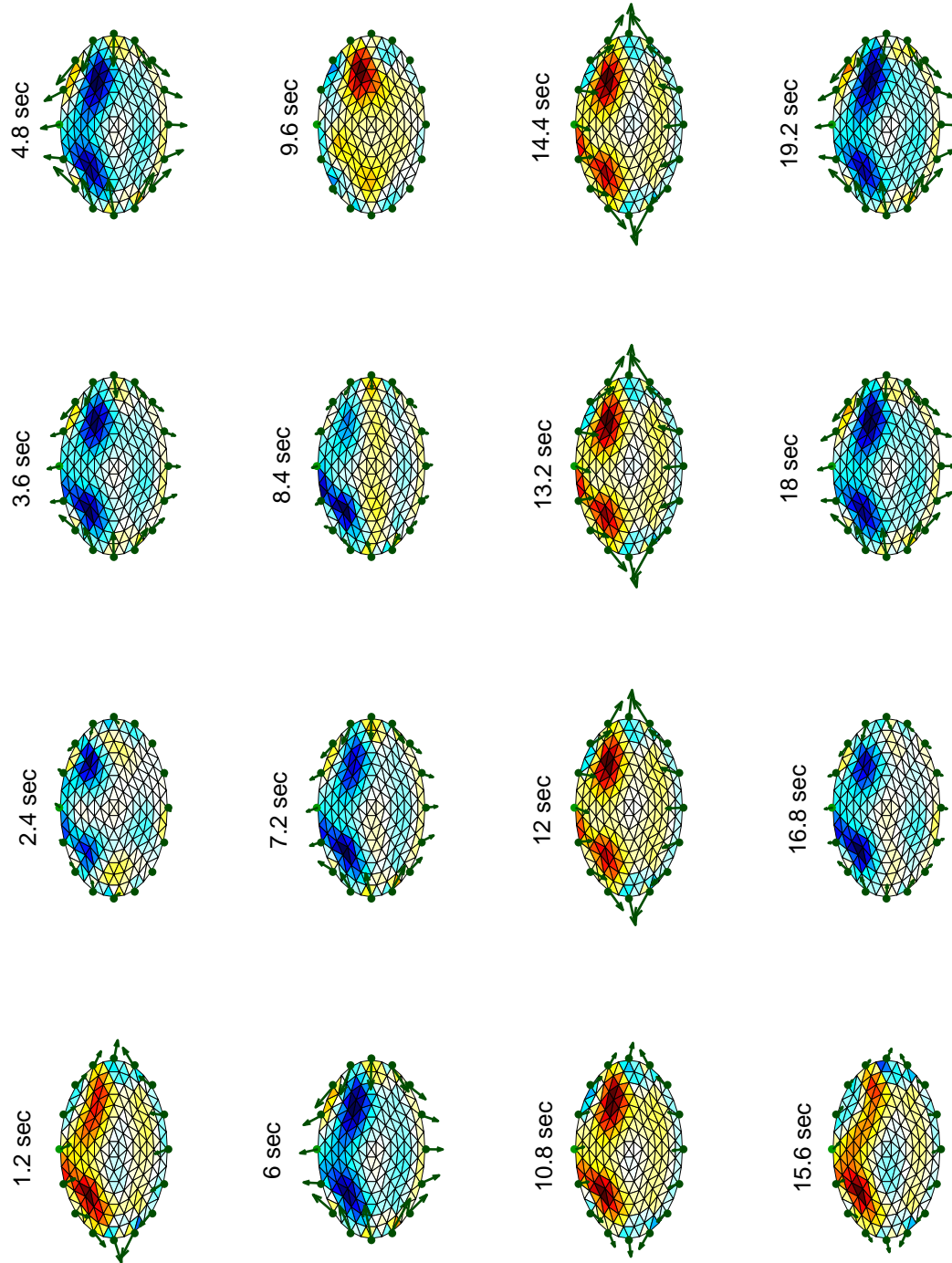


Figure 7.9: TLC/RC in rest state. Time series of 16 images with 1.20 second increments. The hyperparameters used are $\lambda = 5 \times 10^{-2}$ and $\mu = 40$. Electrode displacements are scaled by 20.

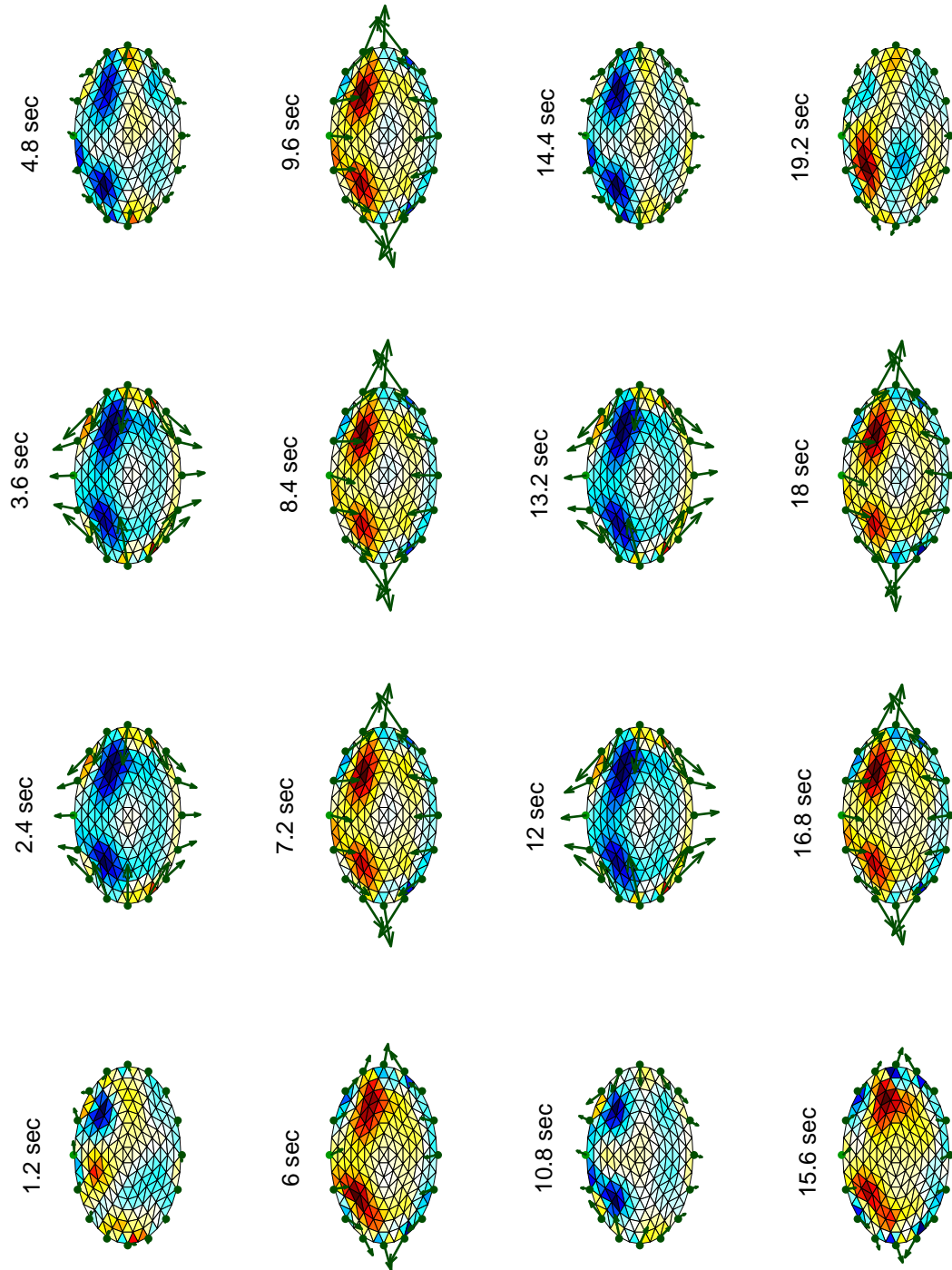


Figure 7.10: TLC/RC in stress state. Time series of 16 images with 1.20 second increments. The hyperparameters used are $\lambda = 5 \times 10^{-2}$ and $\mu = 40$. Electrode displacements are scaled by 20.

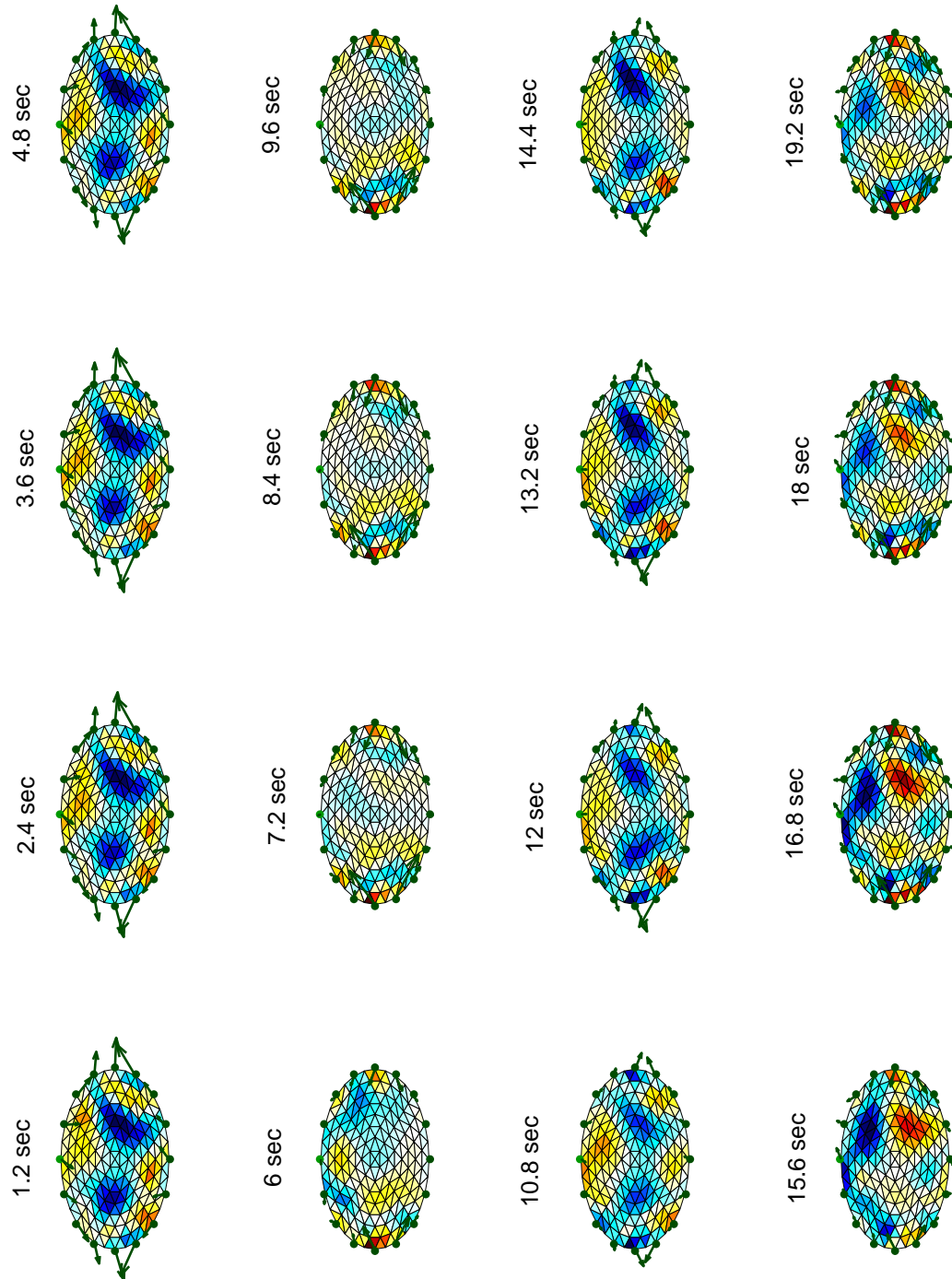


Figure 7.11: Paradoxical breathing in rest state. Time series of 16 images with 1.20 second increments. The hyperparameters used are $\lambda = 5 \times 10^{-2}$ and $\mu = 20$. Electrode displacements are scaled by 20.

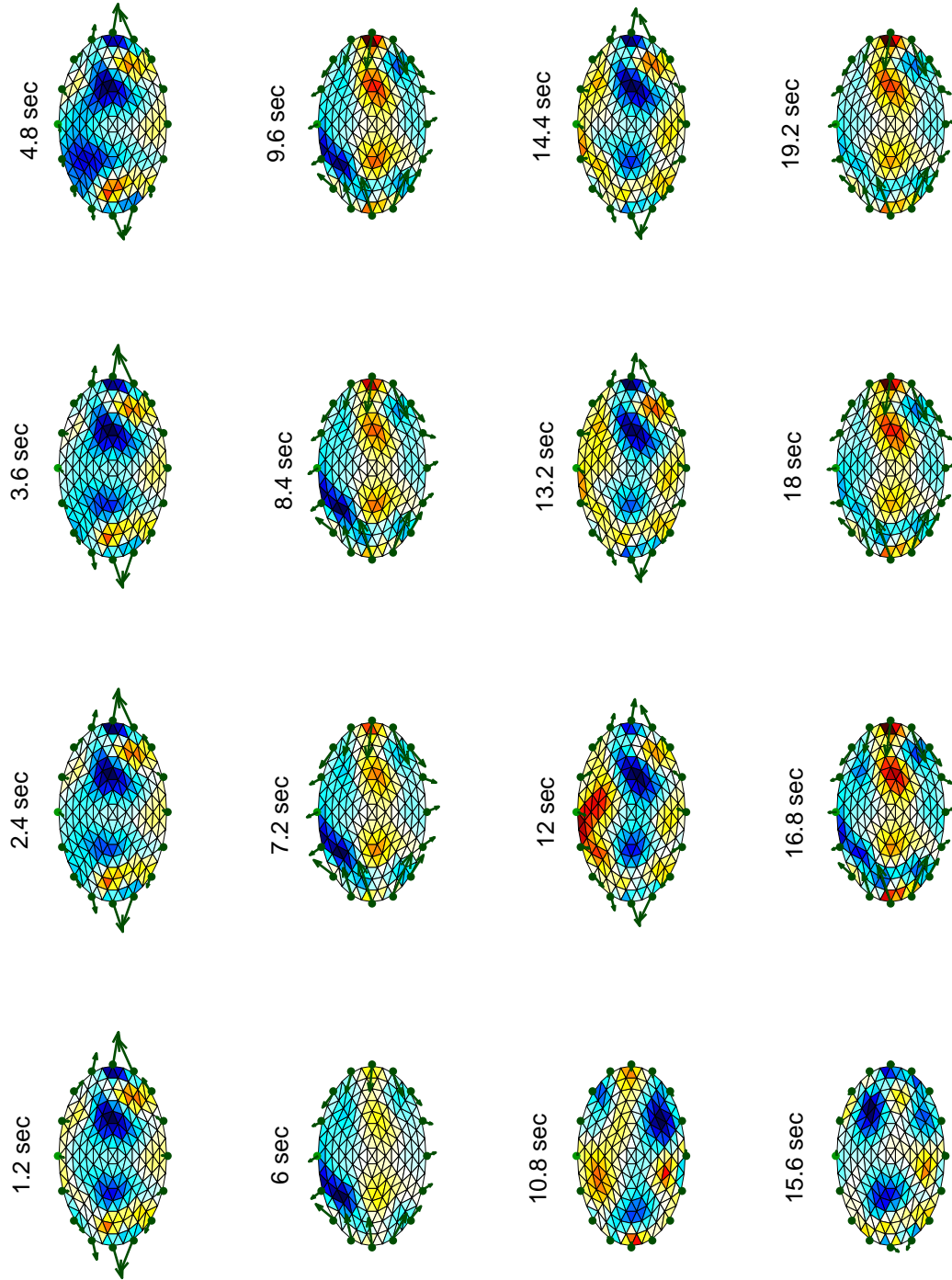


Figure 7.12: Paradoxical breathing in stress state. Time series of 16 images with 1.20 second increments. The hyperparameters used are $\lambda = 5 \times 10^{-2}$ and $\mu = 20$. Electrode displacements are scaled by 20.

simulations with reasonable electrode displacement results. In the worst case for simulated data, the proposed algorithm's AAM was 73% smaller than the standard algorithm's AAM. The phantom 2D data were correctly reconstructed; however, inconclusive results were observed for 3D data. The 2D data are reconstructed with acceptable noise reduction, due to boundary deformation, and produce reasonable electrode displacement results. The algorithm is also capable of reconstructing a time series of deformations, simulating those from breathing without the need of hyperparameter adjustment. In the worst case for phantom data, the proposed algorithm's AAM was 80% smaller than the standard algorithm's AAM. The *in vivo* 2D data were reasonably reconstructed, but showed limitations in tidal breathing. Respiration and rib cage deformations are recognizable in all three breathing patterns using the time series of 2D data. The patterns observed in the time series correspond well with the recorded respiration frequencies and conventions used in the experiments. The *in vivo* 3D data produced inconclusive results. Perhaps this was due to the lack of measurement data available from 16 electrodes, and the lower resolution in the z dimension since inter-ring excitations were not used.

In hindsight of the reconstructions from these acquired data, further limitations of the experiments and the proposed algorithm are considered. More independent measurement data are required when imaging complex volumetric media. Many irregularities are introduced in the acquired data since the fundamental EIT assumptions made in chapters 2 and 4 do not hold, but rather approximate the medium's true properties. That is, *in vivo* media is not linear, isotropic conductors, and the human body is an electrically active medium that can at best be approximated using a quasi-static system. Furthermore, since current diffusion is a non-local process, electrical energy off-plane of the electrode rings will contribute to the measurement data. This effect appears to reduce spatial resolution in the z dimension. These irregularities can possibly be identified and compensated by acquiring more measurement data per frame. This can be accomplished by using more electrodes, safely applying multi-frequency and multi-amplitude excitation currents, and applying different inter- and intra-ring excitation patterns per frame.

Addressing these limitations would likely improve the proposed algorithm's performance. However, the algorithm, "as is", is capable of reconstructing data from various sources. This demonstrates the proof-of-concept that the regularization of deformable media is realistic. The final chapter concludes the thesis by summarizing the results of the research presented, and by briefly discussing the pertinent directions for future work.

Chapter 8

Conclusion

In EIT, electrical energy is applied and measured at the boundary of a medium to produce an image of its internal conductivity distribution. The resulting image is obtained by the solution of a generalized Laplace partial differential equation. One of the most researched application of EIT is clinical diagnosis as a non-invasive functional imaging modality.

One major complication of EIT is the significant degradation of the conductivity distribution due to changes in boundary shape and, hence, electrode position during measurement. Similar to other modalities, EIT incurs artefacts in reconstructed images when patient movement disturbs the measurement environment. The occurrence of these errors leads to reduced repeatability and reliability in diagnostic imaging, which is unacceptable for clinical use.

In the examination of pulmonary ventilation, the expansion of the patient's rib cage is known to introduce severe artefacts in the reconstructed images. These are due to spatial inaccuracies in electrode position by consequence of breathing and change in body posture. Furthermore, the artefacts manifested by electrode position error are escalated due to the inherent non-linear inverse problem of EIT. The difficulty arises, since EIT measurements are projected onto a geometric reconstruction model that approximates the shape of the body being imaged. The displacement of the electrodes reduces the accuracy of the reconstruction model, producing misrepresentative images.

8.1 EIT for Deformable Media

This thesis synthesized aspects of the literature pertaining to the fundamentals of EIT and inverse problems. The objective was the assessment of solving the inverse conductivity problem over a deformable boundary, and the development of an implemented solution. Such a solution was then to be validated across various types of measurement data and performance-ranked with appropriate figures of merit (i.e., position error, blur radius, and artefact amplitude).

A study of image variability from boundary deformation positively verified that incorrect or unknown electrode position in the inverse model negatively influences the reconstructed conductivity distribution. These effects manifest deteriorations of true conductive regions and also produce false conductivity artefacts near the displacement electrodes. In simulation, we observed that errors between 0.75 cm and 3.00 cm are capable of creating significant variability from 5% to over 10% in the conductivity distribution that can lead to misunderstood images. Such error margins can materialize from three factors: *i*) boundary deformation due to involuntary patient motion and breathing, *ii*) the simplified geometry of inverse models used in image reconstruction, and *iii*) human error in electrode placement during clinical trials.

This thesis proposes a *maximum a posteriori* regularization algorithm that reconstructs the conductivity change image and electrode displacements as a solution of the EIT problem for deformable media. The problem is approached in terms of a regularized inverse, using an augmented Jacobian, sensitive to conductivity change and electrode displacement. A reconstruction *a priori* term is designed to impose a smoothness constraint on the conductivity spatial distribution and the electrode displacements. Then, a Tikhonov regularized algorithm is implemented based on the augmented Jacobian and the smoothness constraint. Performance figures of merit are applied to quantify the image resolution, the position accuracy, and the presence of artefacts. These measures were compared to a standard reconstruction algorithm subject to boundary deformation. The algorithm is applied to 2D and 3D models, subjected to boundary deformation using simulation, phantom, and *in vivo* acquired

data.

Results show good reconstructions for simulated, phantom, and *in vivo* measurements. The electrode displacement is faithfully reconstructed, and the conductivity change image shows dramatically less artefacts than the standard algorithm. The average image reconstruction artefact amplitude is reduced by more than 70% in both simulated and phantom data reconstructions. Moreover, the algorithm requires little additional computational time over the standard algorithm, once pre-calculations are done. Thus, the proposed algorithm is suitable for real-time monitoring. The implemented software code and standardized experimental data used in this study was contributed to the GNU public-licensed EIDORS collaboration. In conclusion, the results from this study support the feasibility of EIT for clinical diagnostics in presence of patient movement commonly observed during extended periods of monitoring. The author further anticipates that the techniques developed in this thesis will be useful to increase the accuracy and reliability of EIT in various clinical and experimental applications involving deformable media.

8.2 Future Directions

Many avenues of research have presented themselves during the study related to this thesis. Despite that most of these are mentioned throughout this thesis and directly applicable to the problem of deformable media, only the most significant issues concerning this research are suggested here for further study.

- *Further development of volumetric imaging of experimental phantom and in vivo data.*

Since EIT has excellent temporal resolution, the development of volumetric imaging will provide the capability of measuring volume and flow of internal fluids. This would be particularly useful in medical applications, since these data are typically used in clinical diagnostics. The research and development of excitation patterns and electrode configurations that yield more independent measurement data per frame would be a good initial study.

- *The development of complimentary instruments for the external acquisition of boundary geometry data.*

This information would drastically improve image reconstruction, since an accurate geometrical inverse model can be designed. Given these data, boundary deformation could be for the most part accounted prior to solving the inverse problem. The design of an EIT instrument with integrated machine vision equipment is needed to realize this.

- *The research and development of a reconstruction scheme with temporal modelling.*

Since EIT is a functional modality capable of monitoring physiological processes, a stronger temporal framework would be useful in the study of physiological processes in the time and frequency domains. This consists of the study of the dynamic generalized Laplace equation, if necessary without quasi-static EM field assumptions, and the development of temporal *a priori* models. Phantom experiments must be designed to analyse the temporal performance of the EIT instrument and the reconstruction algorithm quantitatively.

Bibliography

- (2003). *Medical Device Regulations: Global overview and guiding principles*. World Health Organization.
- Adler, A. & Guardo, R. (1996). Electrical impedance tomography: regularized imaging and contrast detection. *IEEE Trans. Med. Imag.*, **15**, 170–179.
- Adler, A. & Lionheart, W.R.B. (2006). Uses and abuses of EIDORS: an extensible software base for EIT. *Physiol. Meas.*, **27**, S25–S42.
- Adler, A., Guardo, R. & Berthiaume, Y. (1996). Impedance imaging of lung ventilation: do we need to account for chest expansion? *IEEE Trans. Biomed. Eng.*, **43**, 414–420.
- Asfaw, Y.W. (2005). *Automatic Detection of Detached and Erroneous Electrodes In Electrical Impedance Tomography*. M.a.sc. thesis, University of Ottawa, Ottawa, Canada.
- Aster, R.C., Borchers, B. & Thurber, C. (2005). *Parameter Estimation and Inverse Problems*. Elsevier, Burlington, USA.
- Barber, D.C. & Brown, B.H. (1998). Errors in reconstruction of resistivity images using a linear reconstruction technique. *Physiol. Meas.*, **9**, 101–104.
- Blott, B.H., Daniell, G.J. & Meeson, S. (1998). Electrical impedance tomography with compensation for electrode positioning variations. *Phys. Med. Biol.*, **43**, 1731–1739.
- Cheney, M., Isaacson, D. & Newell, J.C. (1999). Electrical impedance tomography. *SIAM Review*, **41**, 85–101.

- Cheng, K.S., Isaacson, D., Newell, J.C. & Gisser, D.G. (1989). Electrode models for electric current computed tomography. *36*, 918–924.
- Cherepenin, V.A., Karpov, A.Y., Korjenevsky, A.V., Kornienko, V.N., Kultiasov, Y.S., Ochapkin, M.B., Trochanova, O.V. & Meister, J.D. (2002). Three-dimensional EIT imaging of breast tissues: system design and clinical testing. *IEEE Trans. Med. Imag.*, **21**, 662–667.
- Coulombe, N., Gagnon, H., Marquis, F., Skrobik, Y. & Guardo, R. (2005). A parametric model of the relationship between EIT and total lung volume. *Physiol. Meas.*, **26**, 401–411.
- Frerichs, I. (2000). Electrical impedance tomography (EIT) in applications related to lung and ventilation: a review of experimental and clinical activities. *Physiol. Meas.*, **21**, R1–R21.
- Frerichs, I., Hinz, J., Herrmann, P., Weisser, G., Hahn, G., Quintel, M. & Hellige, G. (2002). Regional lung perfusion as determined by electrical impedance tomography in comparison with electron beam CT imaging. *IEEE Trans. Med. Imag.*, **21**, 646–652.
- Gersing, E., Hoffman, B. & Osypka, M. (1996). Influence of changing peripheral geometry on electrical impedance tomography measurements. *Med. Biol. Eng. Comput.*, **34**, 359–361.
- Geselowitz, D.B. (1971). An application of electrocardiographic lead theory to impedance plethysmography. *IEEE Trans. Biomed. Eng.*, 38–41.
- Gómez-Laberge, C. & Adler, A. (2006). Imaging of electrode movement and conductivity change simulations in electrical impedance tomography. In *Proc. IEEE Canadian Conference of Electrical and Computer Engineering (CCECE'06)*, 1–4, Ottawa, Canada.
- Graham, B. & Adler, A. (2006a). Electrode placement strategies for 3D EIT. In *Conf. 7th Biomed. Appl. of Electrical Impedance Tomography*, Seoul, South Korea.
- Graham, B.M. & Adler, A. (2006b). Objective selection of hyperparameter for EIT. *Physiol. Meas.*, **27**, S65–79.

- Hansen, P.C. (1998). *Rank-Deficient and Discrete Ill-Posed Problems: Numerical Aspects of Linear Inversion*. SIAM, Philadelphia.
- Harris, N.D., Suggett, A.J., Barber, D.C. & Brown, B.H. (1988). Applied potential tomography: a new technique for monitoring pulmonary function. *Physiol. Meas.*, **9**, 79–85.
- Heikkinen, L.M., Vilhunen, T., West, R.M. & Vauhkonen, M. (2002). Simultaneous reconstruction of electrode contact impedances and internal electrical properties, part ii: applications. *Meas. Sci. Technol.*, **13**, 1855–1861.
- Kaipio, J. & Somersalo, E. (2005). *Statistical and Computational Inverse Problems*. Springer, New York.
- Kiber, A., Barber, D.C. & Brown, B.H. (1990). Estimation of object boundary shape from the voltage gradient measurements. In *Proc. Meet. on Electrical Impedance Tomography*, 52–59, Copenhagen, Denmark.
- Kleinermann, F., Avis, N.J. & Alhargan, F.A. (2000). Analytical solution to the three-dimensional electrical forward problem for a circular cylinder. *Inv. Prob.*, **16**, 461–468.
- Kolehmainen, V., Vauhkonen, M., Karjalainen, P.A. & Kaipio, J. (1997). Assessment of errors in static electrical impedance tomography with adjacent and trigonometric current patterns. *Physiol. Meas.*, **18**, 289303.
- Kolehmainen, V., Lassas, M. & Ola, P. (2005). The inverse conductivity problem with an imperfectly known boundary. *SIAM J. Appl. Math.*, **66**, 365–383.
- Kunst, P.W.A., Noordegraaf, A.V., Hoekstra, O.S., Postmus, P.E. & de Vries, P.M.J.M. (1998). Ventilation and perfusion imaging by electrical impedance tomography: a comparison with radionuclide scanning. *Physiol. Meas.*, **19**, 481–490.
- Lionheart, W.R.B. (1997). Conformal uniqueness results in anisotropic electrical impedance imaging. *Inv. Prob.*, **13**, 125–134.

- Lionheart, W.R.B. (1998). Boundary shape and electrical impedance tomography. *Inv. Prob.*, **14**, 139–147.
- Lozano, A. (1997). Electrode errors in bioimpedance measurements for long-term applications. In *Proc. 16th Southern Eng. Conf.*, 3–6, Biloxi, USA.
- Lozano, A., Rosell, J. & Pallás-Areny, R. (1995). Errors in prolonged electrical impedance measurements due to electrode repositioning and postural changes. *Physiol. Meas.*, **16**, 121–130.
- McLeod, C., Gómez-Laberge, C. & Adler, A. (2006). Reduction of electrode position errors in clinical imaging. In *Conf. 7th Biomed. Appl. of Electrical Impedance Tomography*, Seoul, South Korea.
- Metherall, P. (1998). *Three Dimensional Electrical Impedance Tomography of the Human Thorax*. Ph.D. thesis, University of Sheffield, Sheffield, United Kingdom.
- Mueller, J.L., Siltanen, S. & Isaacson, D. (2002). A direct reconstruction algorithm for electrical impedance tomography. *IEEE Trans. Med. Imag.*, **21**, 555–559.
- Patterson, R.P., Zhang, J., Mason, L.I. & Jerosch-Herold, M. (2001). Variability in the cardiac EIT image as a function of electrode position, lung volume and body position. *Physiol. Meas.*, **22**, 159–166.
- Polydorides, N. (2002). *Image Reconstruction Algorithms for Soft-Field Tomography*. Ph.D. thesis, University of Manchester, Manchester, United Kingdom.
- Schöberl, J. (1997). An advancing front 2D/3D-mesh generator based on abstract rules. *Comput. Visual. Sci.*, 41–52.
- Siltanen, S., Mueller, J. & Isaacson, D. (2000). An implementation of the reconstruction algorithm of A Nachman for the 2D inverse conductivity problem. *Inv. Prob.*, **16**, 681–699.
- Soleimani, M., Gómez-Laberge, C. & Adler, A. (2006). Imaging of conductivity changes and electrode movement in EIT. *Physiol. Meas.*, **27**, S103–S113.

- Somersalo, E., Cheney, M. & Isaacson, D. (1992). Existence and uniqueness for electrode models for electric current computed tomography. *SIAM J. Appl. Math.*, **52**, 1023–1040.
- Tarantola, A. (2005). *Inverse Problem Theory and Methods for Parameter Estimation*. SIAM, Philadelphia.
- Unser, M. & Alroubi, A. (1996). A review of wavelets in biomedical applications. *Proc. IEEE*, **84**, 626–638.
- Webster, J.G., ed. (1998). *Medical Instrumentation: Application and Design*. John Wiley & Sons, New York, 3rd edn.
- West, R.M., Aykroyd, R.G., Meng, S. & Williams, R.A. (2004). Markov chain Monte Carlo techniques and spatial-temporal modelling for medical EIT. *Physiol. Meas.*, 181–194.
- Wheeler, J.L., Wang, W. & Tang, M. (2002). A comparison of methods for measurement of spatial resolution in two-dimensional circular EIT images. *Physiol. Meas.*, **23**, 169–176.
- Zhang, J. & Patterson, R. (2005). EIT images of ventilation: what contributes to the resistivity changes? *Physiol. Meas.*, **26**, S81S92.
- Zlochiver, S., Freimark, D., Arad, M., Adunsky, A. & Abboud, S. (2006). Parametric EIT for monitoring cardiac stroke volume. *Physiol. Meas.*, **27**, S139–S146.

Appendix A

Data Acquisition Records

This appendix contains the records taken during data acquisition in EIT experiment using the Goe-MF II EIT instrument (Viasys Healthcare, Höchberg, Germany). The first section contains the details of the saline phantom experiments, and the second section presents the details of the human *in vivo* experiments. These were carried out along the regulations of the Human Ethics body of the University of Ottawa under the certification file *H 05-04-02*.

A.1 Phantom Experiment

```
% *****  
% Electrical Impedance Tomography  
% VIASYS invitro data  
% University of Ottawa  
% Department of Electrical Engineering  
% Date:   October 14, 2005  
% Author: Camille Gomez-Laberge  
% *****
```

This README file is the documentation that accompanies the data collected in these directories: ph1t1/ ph2t1/ ph3t1/ ph3t2/

```
% *****  
% THE EXPERIMENT  
% *****  
Experimenter: Camille Gomez-Laberge  
Date Collected: October 4, 2005  
Locale: Research laboratory, University of Ottawa  
Equipment: EIT Viasys / University of Gottingen  
Phantoms: All phantoms used are polyethylene pails 30 cm in height and diameter.  
Electrodes: See individual phantom descriptions in each part of the experiment.  
Electrolytic solution: 0.9% saline solution  
Objects: 2 golf balls (non-conductive) 2 cm radius spheres suspended in
```

solution with 2.7 kg tension fishing line (nylon).

Measurement Procedure: Ambient temperature in room is 25 degrees Celsius.

Details for each part of the experiment follow:

PART I:

Directory: ph1t1/

Phantom description: Phantom 1 - Uses brass plated, steel thumb-tacs as electrodes. They are arranged in a 16 electrode plane 13 cm above the phantom bottom. The ground electrode is placed in the centre of the bottom. The solution is filled to the 26 cm mark. With time these electrodes became very corroded. The coordinate system to define the object positions in the phantom use the ground electrode as the origin. The x-axis is aligned with electrode 1 and the y-axis with electrode 5. The z-axis is aligned upwards.

Procedure: There are 5 different measurement setups. Each setup was measured 5 times. Objects are placed at the electrode plane level (i.e. we only vary the x and y coordinates).

Setup 1: No objects in phantom (just solution)

Data files: vitro200905_ph1t1_001.get - vitro200905_ph1t1_005.get

Setup 2: Object 1 in centre of electrode ring (0,0) cm

Data files: vitro200905_ph1t1_006.get - vitro200905_ph1t1_010.get

Setup 3: Object 1 at (0,7) cm

Data files: vitro200905_ph1t1_011.get - vitro200905_ph1t1_015.get

Setup 4: Object 1 at (0,7) cm and object 2 at (7,0) cm

Data files: vitro200905_ph1t1_016.get - vitro200905_ph1t1_020.get

Setup 5: Object 1 at (0,7) cm and object 2 at (7,0) cm and phantom is distorted into an elliptical shape by compressing the walls in the y-axis direction until the short axis measures 25 cm across.

Initially the phantom is circular, during the first 6 seconds it is gradually compressed into the elliptical shape and held like so for the remainder of the measurement.

Data files: vitro200905_ph1t1_021.get - vitro200905_ph1t1_025.get

Note: Object positions were measured before distorting the phantom.

Averaged data: The five measurements in each setup (1-4 only) have been read into Matlab and averaged. The average data is stored in the avgdata_ph1t1.mat file.

PART II:

Directory: ph2t1/

Phantom description: Phantom 2 - Uses brass plated, steel thumb-tacs as electrodes. They are arranged in two 8 electrode planes. The lower is at z = 10 cm level and the upper at z = 20 cm. The upper ring is offset by a small

rotation so that the electrodes between both planes form a zig-zag pattern (e.g. Charlie Brown's sweater). The ground electrode is placed in the centre of the bottom (0,0,0). The solution is filled to the 30 cm mark. With time these electrodes became very corroded. The coordinate system to define the object positions in the phantom use the ground electrode as the origin. The x-axis is aligned with electrode 1 (upper plane) and the y-axis with electrode 5 (upper). The upper plane has all odd numbered electrodes. The z-axis is aligned upwards.

Procedure: There are 6 different measurement setups. Each setup was measured 5 times. Objects are placed using (x,y,z) coordinates.

Setup 1: No objects in phantom (just solution)

Data files: vitro200905_ph2t1_002.get - vitro200905_ph2t1_006.get

Note: Measurement 001.get was discarded.

Setup 2: Object 1 in centre of electrode ring (0,0,15) cm

Data files: vitro200905_ph2t1_007.get - vitro200905_ph2t1_011.get

Setup 3: Object 1 at (0,7,10) cm; object 2 (0,7,20) cm

Data files: vitro200905_ph1t1_012.get - vitro200905_ph1t1_016.get

Setup 4: Object 1 at (7,0,10) cm and object 2 at (0,7,10) cm

Data files: vitro200905_ph2t1_017.get - vitro200905_ph2t1_021.get

Setup 5: Object 1 at (7,0,10) cm and object 2 at (0,7,20) cm

Data files: vitro200905_ph2t1_022.get - vitro200905_ph2t1_026.get

Setup 6: Object 1 at (7,0,10) cm and object 2 at (0,7,20) cm and phantom is distorted into an elliptical shape by compression. See PART I setup 5.

Data files: vitro200905_ph2t1_027.get - vitro200905_ph2t1_031.get

Note: Object positions were measured before distorting the phantom.

Averaged data: The five measurements in each setup (1-5 only) have been read into Matlab and averaged. The average data is stored in the avgdata_p2t1.mat file.

PART III:

Directory: ph3t1/

Phantom description: Phantom 3 - Uses stainless-steel screws as electrodes. They are arranged in two 16 electrode planes. The lower is at z = 10 cm level and the upper at z = 20 cm. The electrodes between rings are aligned vertically. The ground electrode is placed in the centre of the bottom (0,0,0). The solution is filled to the 30 cm mark. The coordinate system to define the object positions in the phantom use the ground electrode as the origin. The x-axis is aligned with electrode 1 (upper plane) and the y-axis with electrode 5 (upper). The upper plane has electrodes 1-16 and lower 17-32. The z-axis is aligned upwards.

Procedure: Only 16 electrodes were used (the entire bottom ring). There is only one measurement here as it was used as a proof of concept test. The single object is moved around in a circular motion during the entire measurement.

Data file: vitro200905_ph3t1_001.get

Note: Electrodes were found to have varying impedances between 200 and 400 Ohms according to the system's calibration test. These values are all within the system's acceptable limits.

PART IV:

Directory: ph3t2/

Phantom description: Phantom 3 - see PART III.

Procedure: Only 16 electrodes were used (the entire bottom ring).

The first 5 setups are almost as in PART I. A sixth setup is also added.

Setup 1: No objects in phantom (just solution)

Data files: vitro200905_ph3t2_001.get - vitro200905_ph3t2_005.get

Setup 2: Object 1 in centre of electrode ring (0,0) cm

Data files: vitro200905_ph3t2_006.get - vitro200905_ph3t2_010.get

Setup 3: Object 1 at (0,7) cm

Data files: vitro200905_ph3t2_011.get - vitro200905_ph3t2_015.get

Setup 4: Object 1 at (0,7) cm and object 2 at (-7,0) cm

Data files: vitro200905_ph3t2_016.get - vitro200905_ph3t2_020.get

Setup 5: Object 1 at (0,7) cm and object 2 at (7,0) cm and phantom is distorted into an elliptical shape by compression. See PART I setup 5.

Data files: vitro200905_ph1t1_021.get - vitro200905_ph1t1_025.get

Note: Object positions were measured before distorting the phantom.

Setup 6: Object 1 at (0,7) cm and object 2 at (-7,0) cm and phantom is distorted into an elliptical shape by compressing the walls in the y-axis direction until the short axis measures 25 cm across.

Initially the phantom is circular, during the first 6 seconds it is gradually compressed into the elliptical shape. Then for the next 6 seconds it is slowly restored to original shape. This is repeated to simulate periodic motion (as in chest wall expansion during breathing) until measurement is complete (60 seconds).

Data files: vitro200905_ph3t2_026.get

Note: Object positions were measured before distorting the phantom.

Averaged data: The five measurements in each setup (1-4 only) have been read into Matlab and averaged. The average data is stored in the avgdata_p3t2.mat file.

% END OF EXPERIMENT

A.2 In Vivo Experiment

```
% *****  
% Electrical Impedance Tomography  
% VIASYS invivo data  
% University of Ottawa  
% Department of Electrical Engineering  
% Date: September 21, 2005  
% Author: Camille Gomez-Laberge  
% *****
```

This README file is the documentation that accompanies the data collected in these directories: cgomez-1pl/ cgomez-2pl/

The rest and stress directories contain the actual measurement data corresponding to each sample taken.

```
% *****  
% THE EXPERIMENT  
% *****  
Male subject  
Age: 25  
Health: Normal  
Experimenter: Li Peng Xie  
Date Collected: September 15, 2005  
Locale: Research laboratory  
Equipment: EIT Viasys / University of Gottingen  
Electrodes: 17 EKG Blue Sensor Ag/Ag-Cl electrodes (16 + reference)  
Skin Preparation: Rubbing alcohol  
Measurement Procedure: All measurements are taken while the subject is supine.  
Ambient temperature in room is 25 degrees Celcius. Details for each part of  
the experiment follow.
```

PART I:

Directory: cgomez-1pl/
Placement: Single plane 16 electrodes aligned with the fifth rib directly below the nipple. Electrode 1 is in the centre of the sternum. The other electrodes are labelled moving towards the subject's right side so that electrode 5 is under the right armpit, electrode 9 on the spine and electrode 13 under the left armpit. The reference electrode is placed on the right side of the subject's waist line.

Subject is rested - in normal state

1. Tidal breathing

Heart rate: 62 bpm

Data file: vivo150905_t1_001.get

Note: Measurement begins when lungs are at functional residual capacity.

2. Total Lung Capacity - Residual Capacity (TLC-RC)

Heart rate: 62 bpm

Data file: vivo150905_t1_002.get

Note: Measurement begins when lungs are at residual capacity.

3. Volume transfer

Heart rate: 62 bpm

Data file: vivo150905_t1_003.get

Note: Subject is holding breath and transferring air across thorax by expanding the rib cage and then expanding the abdomen. This is repeated every 5 seconds for the duration of the sample.

Subject induces stress on the cardiovascular system by lower-body exercise (e.g running, climbing stairs).

Subject ran until heartrate exceeded 90 bpm (approx. 6 minutes in this case).

NOTE: The electrodes are not removed during exercise.

4. Tidal breathing

Heart rate: 92 bpm

Data file: vivo150905_t1_004.get

Note: Measurement begins when lungs are at functional residual capacity.

5. TLC-RC

Heart rate: 90 bpm

Data file: vivo150905_t1_005.get

Note: Measurement begins when lungs are at residual capacity.

6. Volume transfer

Heart rate: 84 bpm

Data file: vivo150905_t1_006.get

Note: Subject is holding breath and transferring air across thorax by expanding the rib cage and then expanding the abdomen. This is repeated every 5 seconds for the duration of the sample.

PART II:

Directory: cgomez-2pl/

Placement: Two planes of 8 electrodes each. The upper plane is vertically aligned with the fifth (5) rib directly below the nipple and the lower plane with the seventh (7) rib directly below the nipple. Electrode 1 is on the upper plane in the centre of the sternum. Electrode 2 is on the lower plane but shifted to the right by half the inter-electrode distance on the upper plane. The other electrodes are labelled in a zig-zag pattern, moving towards the subject's right side. The reference electrode is placed on the right side of the subject's waist line.

Subject is rested - in normal state

1. Tidal breathing

Heart rate: 58 bpm

Data file: vivo150905_t2_001.get

Note: Measurement begins when lungs are at functional residual capacity.

2. Total Lung Capacity - Residual Capacity (TLC-RC)

Heart rate: 64 bpm

Data file: vivo150905_t2_002.get

Note: Measurement begins when lungs are at residual capacity.

3. Volume transfer

Heart rate: 60 bpm

Data file: vivo150905_t2_003.get

Note: Subject is holding breath and transferring air across thorax by expanding the rib cage and then expanding the abdomen. This is repeated every 5 seconds for the duration of the sample. Measurement begins with abdomen expanded.

Subject induces stress on the cardiovascular system by lower-body exercise (e.g running, climbing stairs).

Subject ran until heartrate exceeded 90 bpm (approx. 6 minutes in this case).

NOTE: The electrodes are not removed during exercise.

4. Tidal breathing

Heart rate: 102 bpm

Data file: vivo150905_t2_004.get

Note: Measurement begins when lungs are at functional residual capacity.

5. TLC-RC

Heart rate: 96 bpm

Data file: vivo150905_t2_005.get

Note: Measurement begins when lungs are at residual capacity.

6. Volume transfer

Heart rate: 76 bpm

Data file: vivo150905_t2_006.get

Note: Subject is holding breath and transferring air across thorax by expanding the rib cage and then expanding the abdomen. This is repeated every 5 seconds for the duration of the sample. Measurement begins with abdomen expanded.

% END OF EXPERIMENT

Appendix B

Underdamped Reconstruction Artefact

Another important characteristic of the regularization algorithm is the artefact introduced by consequence of regularization of the conductivity change image. This artefact is systematic and can be seen as the characteristic “footprint” of the inverted operator G^{-1} . In image processing, the blur effect observed by passing a single point image through a degradation process is modelled as the *point spread function* (PSF). This function uniquely characterizes any linear space-invariant process and therefore is a useful representation. Recall that section 4.3 establishes the duality between the *maximum a posteriori* regularization algorithm and the Wiener filter. From this duality, it is reasonable to expect that this regularization process can be modelled as some sort of degradation process (i.e. a filter). Indeed, when a forward model with a single contrast in the centre of the medium is used to reconstruct the inverse solution conductivity change image, an underdamped sinusoidal response is observed and shown in figure B.2. This figure shows the forward model on the left with a single contrast. The right side of the figure shows the reconstructed image, which was chromatically adjusted to illustrate the undulations propagating radially away from the contrast position. Without image enhancement, the undulations appear fainter since they are smaller than the central contrast.

The single contrast forward model is reconstructed with several hyperparameter values $\lambda = \{10^{-1}, 10^{-2}, \dots, 10^{-8}\}$ and is fitted to the underdamped second order function

$$y(x) = \frac{e^{-\zeta\omega_n x}}{\sqrt{1-\zeta^2}} \sin(\sqrt{1-\zeta^2}\omega_n x + \theta) \quad (\text{B.1})$$

where ω_n and ζ are the natural frequency and damping ratio parameters, respectively. Figure B.2 shows four plots of the normalized reconstructed image versus the medium’s radial axis. Superimposed is the second order function $y(x)$ that is fitted using the “multidimensional unconstrained non-linear minimization algorithm” implemented as the `fminsearch` function in MATLAB. The plots are shown, as indicated in the figure, for hyperparameter λ set to 10^{-2} , 10^{-5} , 10^{-7} , and 10^{-8} . We observe the trend of decreasing ω_n and increasing ζ with increasing λ . That is, as more regularization is applied, the solution becomes blurred and smooth. The familiar Gibbs phenomenon, particular to cut-off filters, is also observed here.

The fitted parameters ω_n (solid blue curve) and ζ (dotted red curve) are plotted versus the hyperparameter λ in figure B.3. This graph reveals the logarithmic proportionality of

Forward Problem with single contrast

Reconstructed contrast showing wave artefact

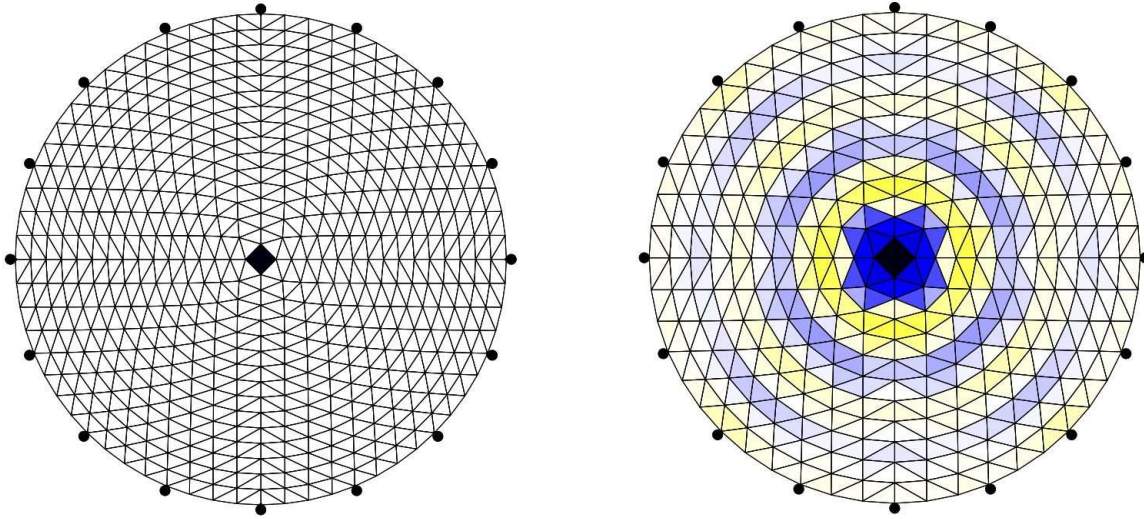


Figure B.1: Illustration of the underdamped artefact during image reconstruction. *Left:* The forward model with a single contrast. *Right:* The standard reconstructed image with $\lambda = 10^{-6}$. The image was chromatically adjusted to accentuate the undulations.

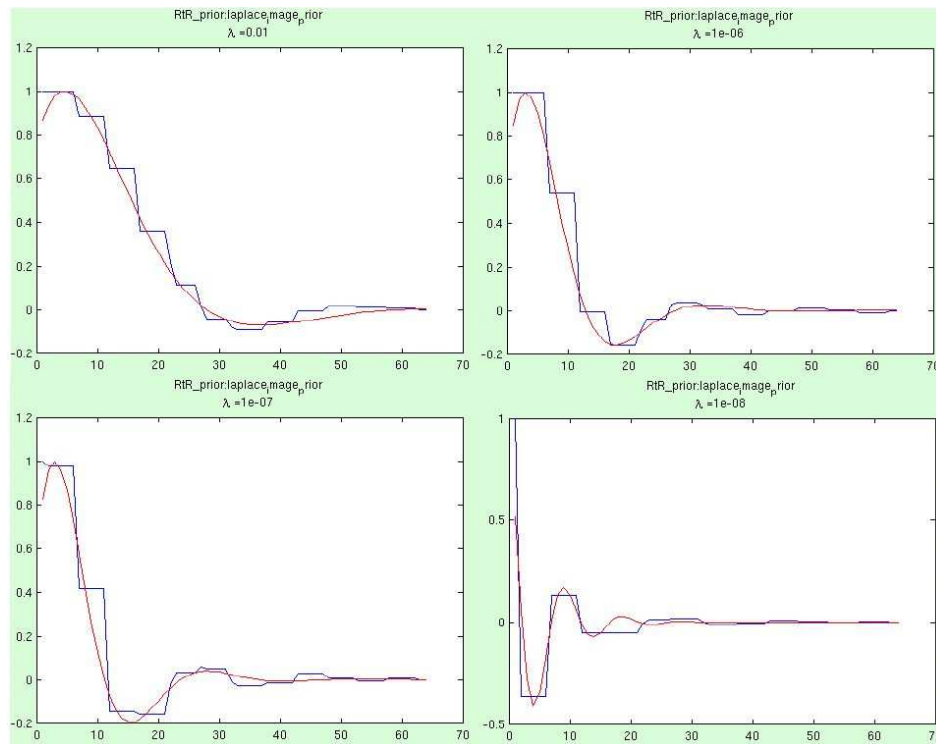


Figure B.2: Superposition of normalized reconstructed images and second order response plots for varying λ . Plots are shown for $\lambda = 10^{-2}, 10^{-5}, 10^{-7}, 10^{-8}$, as indicated above each graph.

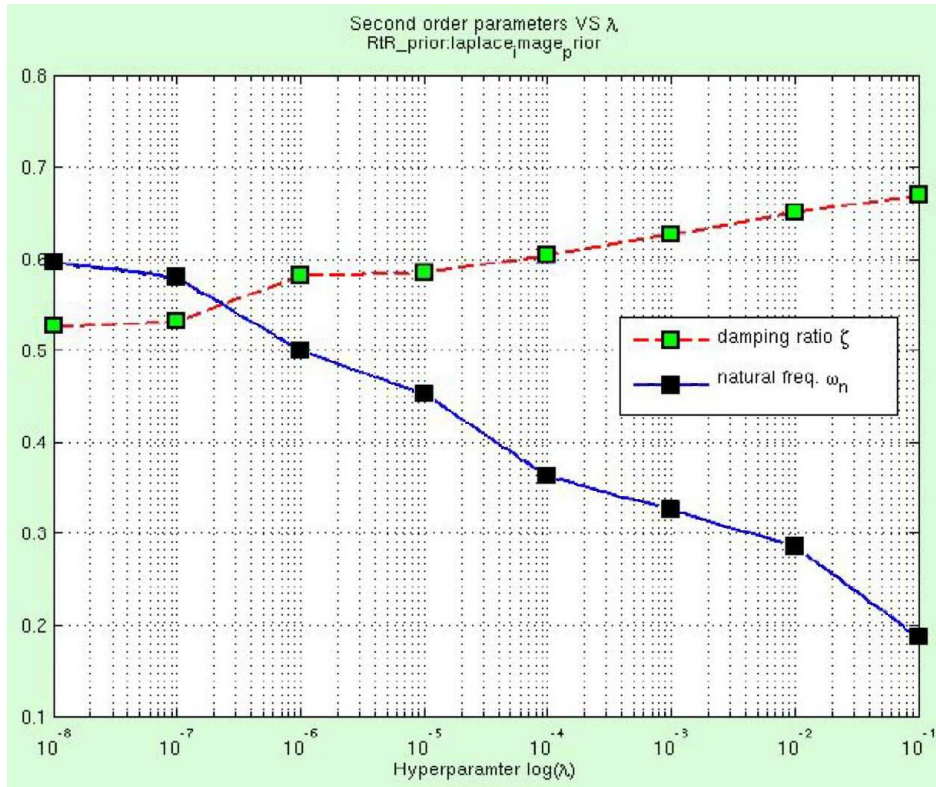


Figure B.3: Semi-logarithmic plot of fitted second order function parameters ω_n (solid blue) and ζ (dotted red) from equation (B.1) vs. $\log \lambda$.

these parameters to λ . This suggests that the reconstruction artefact observed is systematic and can be modelled and accounted for during post-processing of images. Some limitations however must be addressed in these results. First and foremost, the EIT inverse operator G^{-1} is non-linear and space-variant. Therefore, G^{-1} cannot be completely characterized by a single PSF as it will vary with contrast location and will violate the superposition principle of linear systems. Second, the implementation of G^{-1} presented here is a linearization of the problem and can at best approximate the actual solution. Hence, the underdamped sinusoid response observed is a simplification of the actual response. A closer look at figure B.2 reveals that equation (B.1) does not fit the reconstructed image response well. It is found that the response is better described in two distinct parts which require different parameter values. The first part is the initial descent of the curve and the second part is the subsequent oscillations. The descent always has a larger damping ratio and smaller natural frequency than the secondary oscillations. We hypothesize that factors that may cause this behaviour are due to *i*) the approximation of point contrast using finite elements, and *ii*) possible interference of the conductivity change image with the finite medium. Although a systematic response is demonstrated here, a closer look at these factors is required to model the reconstruction artefact further. The key functions of the software code used for this analysis are printed in the third section of appendix C entitled “Artefact Analysis”.

Appendix C

Software Code

This appendix is a printout of the MATLAB code used to implement and analyse the material from this thesis. Unfortunately, only the key components of the code are printed since the entire solution would require too much space. The appendix is divided into three sections. The first section shows the actual electrode displacement regularization code. The second section shows the code written for the performance analysis of the image reconstruction algorithms. The third section shows the code written to research the conductivity and displacement artefacts. All code from this appendix works in conjunction with the EIDORS suite.

C.1 Electrode Displacement

```
function elect_move(fig_num)
% ELECT_MOVE Electrode movement mainline for Physiol. Meas. publication:
% Soleimani et al. 2005. Generates the paper's results and plots its six
% figures.
% (C) 2006, Camille Gomez-Laberge & Andy Adler.
% Licenced under the GPL Version 2.
% $Id: elect_move.m,v 1.31 2006/05/29 18:11:11 cgomez Exp $

% Flag for printing EPS files (set to 1 for exporting results)
global PRINT_EPS
PRINT_EPS = 0;
% Add eidors3d/ to Matlab path if not present.
test_eidors_path();
% Set eidors default colours
calc_colours('mapped_colour',128);
calc_colours('backgnd',[.9,.9,.9]);
% Generate eidors planar finite element model
mdl2dim = mk_common_model('b2c');

% rotate mesh
rang= 45*pi/180; rotate= [cos(rang),-sin(rang);sin(rang),cos(rang)];
mdl2dim.fwd_model.nodes = (rotate*mdl2dim.fwd_model.nodes)';
mdl2dim.fwd_model.normalize_measurements= 0;
mdl2dim.fwd_model.electrode= mdl2dim.fwd_model.electrode([3:16,1,2]);
randn('state',2001); % use same noise for each try
clf;
switch fig_num
% Generate simulation data without noise and standard reconstruction
case 0
mysubplot(1,2,1);
[vh,vi] = sim_move_2d_data(0, 1);
mysubplot(1,2,2);
show_2d_stdsim(mdl2dim, 0.1, 0.01);
if PRINT_EPS printeps('fig-simulation.eps',1,2); end
```

```

% Inverse solution of simulated movement data (mu is 10 and 20)
case 1
mysubplot(1,2,1);
show_2d_sim mdl2dim, 0.1, 0.01, 1);
mysubplot(1,2,2);
show_2d_sim mdl2dim, 0.1, 0.01, 20);
if PRINT_EPS
    printeps('fig-noise=20dB-hp=1e-2-mu=1-20.eps',1,2);
end

% Same as case 1 except with other parameters (lambda is e-2 and e-3)
case 2
mysubplot(1,2,1);
show_2d_sim mdl2dim, 0.1, 0.01, 15);
mysubplot(1,2,2);
show_2d_sim mdl2dim, 0.1, 0.001, 15);
if PRINT_EPS
    printeps('fig-noise=20dB-hp=1e-2-1e-3-mu=15.eps',1,2);
end

% Same as case 1 except with other parameters (noise is 0.1 0.5)
case 3
mysubplot(1,2,1);
show_2d_sim mdl2dim, 0.1, 0.003, 10);
mysubplot(1,2,2);
show_2d_sim mdl2dim, 0.2, 0.003, 10);
if PRINT_EPS
    printeps('fig-noise=20dB-40dB-hp=5e-3-mu=10.eps',1,2);
end

% Apply movement algorithms to experimental data
case 4
% Extract measurements from EIT data files and set parameters and
% movement penalty (symbol mu in Soleimani paper).
[vh,vi] = meas_move_data(...
    '/home/cgomez/cvs-viva/data/eit/viasys/invitro/oct05/ph3t2/',...
    'vitro041005_ph3t2_001.get', 'vitro041005_ph3t2_026.get', 160);
hparameter = 1e-2;
move_vs_conduct = 20;

% Define a eidors_obj Movement model solved by electrode movement
% algorithms.
mdl2dim.hyperparameter.value= hparameter;
mdlM = mdl2dim;
mdlM.fwd_model.conductivity_jacobian = mdlM.fwd_model.jacobian;
mdlM.fwd_model.jacobian = 'aa_e_move_jacobian';
mdlM.RtR_prior = 'aa_e_move_image_prior';
mdlM.aa_e_move_image_prior.parameters = move_vs_conduct;

% Solve inverse problem for mdl2dim and mdlM eidors_obj models.
img2dim = inv_solve(mdl2dim, vi, vh); % solved no movement algorithms
imgM = inv_solve(mdlM, vi, vh); % solved with movement algorithms
ed= img2dim.elem_data;
lim= .37;
ed = ed.*(abs(ed)<=lim) + lim*sign(ed).*(abs(ed)>lim);
img2dim_scl= img2dim;
img2dim_scl.elem_data= ed;
mysubplot(1,2,1)
show_fem_move(img2dim_scl);
mysubplot(1,2,2)
show_fem_move(imgM, [], 10);

% Calculate artefact for each reconstruction
load ex_imask.mat;
e_space = calc_element_vol(img2dim);
artefacts = ~imask.*img2dim.elem_data;
amp = sqrt(sum( e_space.*artefacts.^2 ) / sum( e_space ));
fprintf('Standard method artefact power = %f \n',amp);
tmpM = imgM;
tmpM.elem_data = imgM.elem_data(1:256);

```

```

    artefacts = ~imask.*tmpM.elem_data;
    amp = sqrt(sum( e_space.*artefacts.^2 ) / sum( e_space ));
    fprintf('Movement method artefact power = %f \n',amp);
    if PRINT_EPS printeps('fig-tankdata2.eps',1,2); end

% Generate 3D simulation data with forward solution, show FEM geometry
case 5
    [mdl3dim, img3dim, vh, vi, move] = sim_move_3d_data(2, .1, 20, 1);
    if PRINT_EPS printeps('fig-3Dgeometry-10xExageration.eps',2,2); end

% Inverse solution of 3D simulated data
case 6
    % Generate 3D simulation data with forward solution
    [mdl3dim, img3dim, vh,vi, move] = sim_move_3d_data(2, .1, -2, 0);
    mdl3dim.RtR_prior = 'laplace_image_prior';
    mdl3dim.hyperparameter.value = 3e-3;

    % Show slices of 3D model with true movement vectors
    mysubplot(1,3,1);
    img3dim.elem_data = img3dim.elem_data - 1;
    show_slices_move( img3dim, move );

    % Inverse solution of data without movement consideration
    img3dim= inv_solve(mdl3dim, vi, vh);
    mysubplot(1,3,2)
    show_slices_move( img3dim );

    % Inverse solution of data with movement consideration
    move_vs_conduct = 20; % Movement penalty (symbol mu in paper)
    % Define a eidglobalors_obj Movement model solved by electrode movement
    % algorithms.
    mdlM = mdl3dim;
    mdlM.fwd_model.conductivity_jacobian = mdlM.fwd_model.jacobian;
    mdlM.fwd_model.jacobian = 'aa_e_move_jacobian';
    mdlM.RtR_prior = 'aa_e_move_image_prior';
    mdlM.aa_e_move_image_prior.parameters = move_vs_conduct;
    % Solve inversglobale problem and show slices
    imgM = inv_solve(mdlM, vi, vh);
    mysubplot(1,3,3)
    show_slices_move( imgM );

    % Calculate artefact for each reconstruction
    load('datacom.mat','A','B');
    imask = zeros(size(img3dim.elem_data));
    imask(A(:)) = 1;
    imask(B(:)) = 1;
    artefacts = ~imask.*img3dim.elem_data;
    e_space = calc_element_vol(img3dim);
    amp = sqrt(sum(e_space.*artefacts.^2)/sum(e_space));
    fprintf('Standard method artefact power = %f \n', amp);
    tmpM = imgM;
    tmpM.elem_data = imgM.elem_data(1:828);
    artefacts = ~imask.*tmpM.elem_data;
    amp = sqrt(sum(e_space.*artefacts.^2)/sum(e_space));
    fprintf('Movement method artefact power = %f \n', amp);
    if PRINT_EPS printeps('fig-3D-noise=20dB-hp=3e-3.eps',3,3); end

    otherwise
        error('elect_move(): Invalid argument.');
```

end

```

function [vh, vi, f_img, move]= sim_move_2d_data( noiselev, plot_out )
% SIM_MOVE_2D_DATA Forward problem simulation of electrode movement data.
% Args: noiselev - gain factor of normally distributed noise
%       plot_out - set to 1 to plot or 0 not to plot output
% Returns:  vh - voltage data for homogeneous conductivity
%           vi - voltage data for inhomogeneous conductivity
%           f_img - image object with forward problem parameters
%           move - position vector difference of nodes after movement
% (C) 2006, Camille Gomez-Laberge & Andy Adler.
```

```

% Licenced under the GPL Version 2.
% $Id: sim_move_2d_data.m,v 1.4 2006/02/16 22:04:18 cgomez Exp $

% Create circular FEM - creates a eidors_mdl type inv_model.
mdl = mk_common_model('c2c');
% Instantiate a homogeneous forward model.
% ref_level is 1 since we use ones( ).
sigma = ones( size(mdl.fwd_model.elems,1) ,1);
% Create the eidors_obj of type image.
f_img = eidors_obj('image', 'homogeneous image', ...
    'elem_data', sigma, ...
    'fwd_model', mdl.fwd_model,...
    'ref_level', 1);
% Solve homogeneous forward problem
vh = fwd_solve( f_img );

% Hard coded values here represent local inhomogeneities
sigma([75,93,94,113,114,136]) = 1.2;
sigma([105,125,126,149,150,174]) = 0.8;
f_img.elem_data = sigma;

% Simulate node movements - shrink x, stretch y
% node0 before, node1 after movement
movement = [0.99 0; 0 1.01];
%ff= .01/sqrt(2);
%movement = [1-ff, ff; ff, 1+ff];
node0 = f_img.fwd_model.nodes;
node1 = node0*movement;
f_img.fwd_model.nodes = node1;
% Solve inhomogeneous forward problem with movements and normal noise
vi = fwd_solve( f_img );
noise = noiselev*std( vh.meas - vi.meas )*randn( size(vi.meas) );
vi.meas = vi.meas + noise;
move = node1 - node0;
% Plot FEM with conductivities and movement vectors.
if plot_out
    show_fem_move( f_img, move, 20, []);
end

function [mdl3dim, img, vh, vi, move]= sim_move_3d_data(move_geo, ...
    noiselev, movement, plot_out)
% SIM_MOVE_3D_DATA Forward problem simulation of electrode movement data.
% Args: move_geo - boundary movement geometry (0, 1, 2)
%       noiselev - gain factor of normally distributed noise
%       movement - scale factor of movement of electrodes
%       plot_out - set to 1 to plot or 0 not to plot output
% Returns: mdl3dim - eidors_obj 3D finite element model
%          vh      - voltage data for homogeneous conductivity
%          vi      - voltage data for inhomogeneous conductivity
%          move    - position vector difference of nodes after movement
% (C) 2006, Camille Gomez-Laberge & Andy Adler.
% Licenced under the GPL Version 2.
% $Id: sim_move_3d_data.m,v 1.2 2006/05/29 18:11:11 cgomez Exp $

% Generate eidors 3D finite element model
mdl3dim = mk_common_model( 'n3r2' );
mdl3dim.fwd_model.nodes(:,3) = mdl3dim.fwd_model.nodes(:,3)/3;
% Instantiate a homogeneous forward model.
% ref_level is 1 since we use ones( ).
sigma = ones( size(mdl3dim.fwd_model.elems,1) ,1);
% Create eidors_obj type image
img = eidors_obj('image', 'homogeneous image', ...
    'elem_data', sigma, ...
    'fwd_model', mdl3dim.fwd_model, ...
    'ref_level', 1);
% Solve the homogeneous forward problem
vh = fwd_solve( img );

% Set local inhomogeneities using eidors 3D model
load('datacom.mat','A','B');
```

```

sigma(A) = 1.2;
sigma(B) = 0.8;
img.elem_data = sigma;
node0 = img.fwd_model.nodes; % Node variable before movement
node1 = node0; % Node variable after movement
z_axis = node1(:,3);

% Apply geometrical distortion of choice 0, 1 or 2 and scale by movement
% input parameter
switch move_geo
    % Cases 0-2 are 'twisted' elliptical deformations
    case 0
        node1(:,2) = node1(:,2).*(1 - 0.01*movement*z_axis);
        node1(:,1) = node1(:,1).*(1 - 0.01*movement*(1-z_axis));
    case 1
        node1(:,1) = node1(:,1).*(1 + 0.01*movement*z_axis);
        node1(:,2) = node1(:,2).*(1 + 0.01*movement*(1-z_axis));
    case 2
        node1(:,2) = node1(:,2).*(1 - 0.005*movement*z_axis) ...
            .*(1 + 0.005*movement*(1-z_axis));
        node1(:,1) = node1(:,1).*(1 - 0.005*movement*(1-z_axis)) ...
            .*(1 + 0.005*movement*z_axis);
    % Circular contraction along z-axis
    case 3
        node1(:,1) = node1(:,1).*(1 - 0.01*movement*z_axis);
        node1(:,2) = node1(:,2).*(1 - 0.01*movement*z_axis);
    case 4
        node1(:,1) = node1(:,1).*(1 - 0.01*movement*(1-z_axis));
        node1(:,2) = node1(:,2).*(1 - 0.01*movement*(1-z_axis));
    % Circular dilation along z-axis
    case 5
        node1(:,1) = node1(:,1).*(1 + 0.01*movement*z_axis);
        node1(:,2) = node1(:,2).*(1 + 0.01*movement*z_axis);
    case 6
        node1(:,1) = node1(:,1).*(1 + 0.01*movement*(1-z_axis));
        node1(:,2) = node1(:,2).*(1 + 0.01*movement*(1-z_axis));
    % Uniform contraction
    case 7
        node1 = node1.*(1 - 0.005*movement);
    % Uniform dilation
    case 8
        node1 = node1.*(1 + 0.005*movement);
    otherwise
        error('no movement specified');
end

% Solve inhomogeneous forward problem with movements and normal noise.
img.fwd_model.nodes = node1;
vi = fwd_solve( img );
noise = noiselev*std( vh.meas - vi.meas )*randn( size(vi.meas) );
vi.meas = vi.meas + noise;
move = node1 - node0;

% Plot distorted 3D FEM with conductivities.
if plot_out
    calc_colours('ref_level', img.ref_level);
    show_fem( img );
    xlabel('x');
    ylabel('y');
    view([ 1.4265 -1.4018 0 -0.0123;
          0.5251 0.5344 0.9272 -0.9933;
          1.2997 1.3226 -0.3746 13.8761;
          0 0 0 1.0000]);
end

function show_2d_stdsim mdl2dim, noise, hparam
% SHOW_2D_STDSIM Standard inverse solution of planar simulated movement
% data.
% Args: mdl2dim - planar common FEM model
% noise - normalized gain factor of noise

```

```

%      hparam          - regularization hyperparameter
% (C) 2006, Camille Gomez-Laberge & Andy Adler.
% Licenced under the GPL Version 2.
% $Id: show_2d_stdsim.m,v 1.3 2006/05/29 18:11:11 cgomez Exp $

% Flag for printing EPS files (initialized by elect_move).
global PRINT_EPS;
% Set DEBUG to 1 if artefact plots are to be shown.
DEBUG = 0;
% Set eidors_obj hyperparameter member.
mdl2dim.hyperparameter.value= hparam;
% Generate simulated forward problem movement data without plot.
[vh,vi,fwd_img]= sim_move_2d_data( noise, 0 );
% Solve inverse problem for mdl2dim eidors_obj model.
img2dim = inv_solve(mdl2dim, vi, vh);
ed= img2dim.elem_data;
lim= .088;
ed = ed.*(abs(ed)<=lim) + lim*sign(ed).*(abs(ed)>lim);
img2dim_scl= img2dim;
img2dim_scl.elem_data= ed;

% Plot results for each algorithm
calc_colours('ref_level', 0);
show_fem_move(img2dim_scl);

% Calculate standard artefact amplitude and plot its effects new figure
[art_img, amp] = calc_artefact( fwd_img, img2dim, [] );
if DEBUG
    figure;
    calc_colours();
    show_fem(art_img);
    axis('off'); axis('image'); axis(1.3*[-1,1,-1,1]);
    title(['Standard Artefacts: ', num2str(amp)]);
end
fprintf('Standard method artefact power = %f \n',amp);

function show_2d_sim(mdlM, noise, hparam, mv_conduct_ratio)
% SHOW_2D_SIM Inverse solution of planar simulated movement data.
% Args: mdl2dim          - planar common FEM model
%       noise           - normalized gain factor of noise
%       hparam          - regularization hyperparameter
%       mv_conduct_ratio - movement-conductance ratio

% (C) 2006, Camille Gomez-Laberge & Andy Adler.
% Licenced under the GPL Version 2.
% $Id: show_2d_sim.m,v 1.6 2006/02/13 15:44:48 cgomez Exp $

% Flag for printing EPS files (initialized by elect_move).
global PRINT_EPS;
% Set DEBUG to 1 if artefact plots are to be shown.
DEBUG = 0;

% Set eidors_obj hyperparameter member.
mdlM.hyperparameter.value= hparam;
% Place traditional jacobian in temporary member.
mdlM.fwd_model.conductivity_jacobian = mdlM.fwd_model.jacobian;
% Redefine jacobian member for movement & conductivity.
mdlM.fwd_model.jacobian = 'aa_e_move_jacobian';
mdlM.Rtr_prior = 'aa_e_move_image_prior';
mdlM.aa_e_move_image_prior.parameters = mv_conduct_ratio;

% Generate simulated forward problem movement data without plot.
[vh,vi,fwd_img]= sim_move_2d_data( noise, 0 );
% Solve inverse problem for mdlM eidors_obj model.
imgM = inv_solve(mdlM, vi, vh);
% Plot results for each algorithm
show_fem_move(imgM);

% Calculate movement artefact amplitude and plot its effects new figure
[art_img, amp] = calc_artefact( fwd_img, imgM );

```

```

if DEBUG
    figure;
    show_fem(art_img);
    axis('off'); axis('image'); axis(1.3*[-1,1,-1,1]);
    title(['Movement Artefacts: ', num2str(amp)]);
end
fprintf('Movement method artefact power = %f \n',amp);

function [vh,vi]= meas_move_data(fpath, hfile, ifile, frame)
% MEAS_MOVE_DATA Forward problem for measured of electrode movement data
% (i.e. Experimentally aquired EIT data from VIVA lab).
% Args:    fpath - full directory path (string)
%          hfile - homogeneous (reference) data file (string)
%          ifile - inhomogeneous (reference) data file (string)
%          frame - EIT data frame number
% Returns:  vh - voltage data for homogeneous conductivity
%           vi - voltage data for inhomogeneous conductivity
% (C) 2006, Camille Gomez-Laberge & Andy Adler.
% Licenced under the GPL Version 2.
% $Id: meas_move_data.m,v 1.2 2006/05/29 18:11:11 cgomez Exp $

% Data is collected from a phantom filled with saline only - a homogeneous
% medium.
vvmeas = eidors_readdata([fpath, hfile]);
% Compute homogeneous measurements as the average over all frames.
vh = mean(vvmeas,2);
% Data is collected from a distorted phantom filled with saline and two
% suspended inhomogeneities - an inhomogeneous medium.
vmove= eidors_readdata([fpath, ifile]);
% A frame of maximum distortion (electrode movement) found by plotting all
% frames and choosing the ones which correspond to highest tank
% compression.
vi = vmove(:, frame);

```

C.2 Performance Analysis

```

% TESTSCRIPT Algorithm performance currently being used for electrode
% movement. Compares Standard reconstruction with movement algorithm.
% (C) 2006, Camille Gomez-Laberge.
% $Id: Testscript.m,v 1.2 2006/05/29 18:11:11 cgomez Exp $

% Plot results?
RESULTS = 1;
% Standard reconstruction?
STANDARD = 1;
% Dense meshes?
DENSE = 0;

% Add eidors3d/ to Matlab path if not present.
test_eidors_path();
eidors_msg('log_level',0); % Keep eidors quiet
% Set eidors default colours
calc_colours('mapped_colour',128);
calc_colours('backgnd',[.9,.9,.9]);

% Adjustable parameters
mv_conduct_ratio = 1;
hyperparam = [0.5e-3 1e-3 0.5e-2 1e-2 0.5e-1 1e-1];
radius_percent = 0.5; % between 0.00 and 0.90
move=[0.5 1 1.5 2 2.5 3 3.5 4 4.5 5 5.5 6 6.5 7 7.5 8 8.5 9 9.5 10];

% Generate eidors planar finite forward and inverse meshes.
if DENSE
    fwd_mesh = mk_common_model('d2c'); % 1024 elements
    inv_md1 = mk_common_model('c2c'); % 576 elements
else
    fwd_mesh = mk_common_model('c2c'); % 576 elements
    inv_md1 = mk_common_model('b2c'); % 256 elements

```

```

end

% rotate mesh
rang= 45*pi/180; rotate= [cos(rang),-sin(rang);sin(rang),cos(rang)];
inv_mdl.fwd_model.nodes = (rotate*inv_mdl.fwd_model.nodes)';
inv_mdl.fwd_model.normalize_measurements= 0;
inv_mdl.fwd_model.electrode= inv_mdl.fwd_model.electrode([3:16,1,2]);
% Place traditional jacobian in temporary member.
inv_mdl.fwd_model.conductivity_jacobian = inv_mdl.fwd_model.jacobian;
% Redefine jacobian member for movement & conductivity.
inv_mdl.fwd_model.jacobian = 'aa_e_move_jacobian';
inv_mdl.RtR_prior = 'aa_e_move_image_prior';
inv_mdl.aa_e_move_image_prior.parameters = mv_conduct_ratio;

% Recreate mesh for standard model, with standard algs...
if DENSE
    inv_mdl_std = mk_common_model('c2c'); % 576 elements
else
    inv_mdl_std = mk_common_model('b2c'); % 256 elements
end
% Rotate inverse mesh as above in movement reconstruction
inv_mdl_std.fwd_model.nodes = (rotate*inv_mdl.fwd_model.nodes)';
inv_mdl_std.fwd_model.normalize_measurements= 0;
inv_mdl_std.fwd_model.electrode= inv_mdl_std.fwd_model.electrode([3:16,1,2]);

br = zeros(length(hyperparam),length(move));
amp = br;

% Calculate performance for various choices of hyperparameter
for i=1:length(hyperparam)
    inv_mdl.hyperparameter.value = hyperparam(i);
    inv_mdl_std.hyperparameter.value = hyperparam(i);
    hyperparam(i)
    % Collect measurements vs contrast radial position
    for j=1:length(move)
        % Get simulation model parameters
        [f_img, fe_ctr, fe_con, i_img] = ...
            get_model_params(fwd_mesh, inv_mdl, radius_percent, move(j));

        % Measure blur radius
        [br(i,j), b_elem] = meas_blur_radius(f_img, i_img, fe_con);

        % Measure conductivity artefacts
        [art_img, amp(i,j)] = calc_artefact(f_img, i_img, b_elem);
    end

    % Store movement results
    br1_data(i,:) = br(i,:);
    art1_data(i,:) = amp(i,:);

    if STANDARD
        % Redo simulation for standard reconstruction
        % Collect measurements vs contrast radial position
        for j=1:length(move)
            % Get simulation model parameters
            [f_img, fe_ctr, fe_con, i_img] = ...
                get_model_params(fwd_mesh, inv_mdl_std, radius_percent, move(j));
            % Measure blur radius
            [br(i,j), b_elem] = meas_blur_radius(f_img, i_img, fe_con);
            % Measure conductivity artefacts
            [art_img, amp(i,j)] = calc_artefact(f_img, i_img, b_elem);
        end

        % Store standard results
        br0_data(i,:) = br(i,:);
        art0_data(i,:) = amp(i,:);
    end
    % Proposed AMM gain factor
    pgain=(art0_data-art1_data)./art0_data;
end

```

```

% Show results
if RESULTS
    figure('Name','AAM Plots');
    subplot(1,2,1);
    plot(move, art0_data(1,:),'-r',move, art1_data(1,:), '-.b');
    xlim([0.5 10]);
    xlabel('Movement % of \partial\Omega Diameter');
    ylabel('AAM');
    legend('standard','movement');
    title(['AAM: Hyperparameters: \lambda = ', num2str(hyperparam(1)), ' ...
    \mu = ', num2str(mv_conduct_ratio)]);
    subplot(1,2,2);
    plot(move, art0_data(4,:),'-r',move, art1_data(4,:), '-.b');
    xlim([0.5 10]);
    xlabel('Movement % of \partial\Omega Diameter');
    ylabel('AAM');
    legend('standard','movement');
    title(['AAM: Hyperparameters: \lambda = ', num2str(hyperparam(4)), ' ...
    \mu = ', num2str(mv_conduct_ratio)]);

    figure('Name','Average Blur Radius over movement');
    hold on
    semilogx(hyperparam,mean(br0_data,2),'-rs');
    semilogx(hyperparam,mean(br1_data,2),'-bs');
    hold off
    xlim([0.5e-3 1e-1]);
    xlabel('Hyperparameter log_{10}(\lambda)');
    ylabel('Average Blur Radius');
    legend('standard','movement');
    title(['Average Blur Radius over movement using \mu = ', ...
    num2str(mv_conduct_ratio)]);

    figure('Name','Average AAM Gain over lambda');
    plot(move,mean(pgain),'-k');
    ylim([0 1]);
    xlim([0.5 10]);
    xlabel('Movement % of \partial\Omega Diameter');
    ylabel('Average AAM Gain');
    title(['Average AAM Gain over \lambda using \mu = ', ...
    num2str(mv_conduct_ratio)]);
end

function [fwd_img, fwd_elem_ctr, fwd_cntrst, inv_img] = ...
    get_model_params(fwd_mesh, inv mdl, rad_posn, movep)
% GET_MODEL_PARAMS Simulates a single element contrast model, calculates
% the difference inverse solution and returns model data and parameters.
% Args:      fwd_mesh - the forward model mesh object.
%            inv_mdl - the inverse model object set with reconstruction
%                  algorithms to be analyzed.
%            rad_posn - the percentage of radial distance of the contrast
%                  centre.
%            movep - movement in percentage of boundary diameter.
% Returns:   fwd_img - the simulated forward problem eidors image object.
%            fwd_elem_ctr - element-indexed coordinates of each element centre.
%            fwd_cntrst - element index used as the contrast element.
%            inv_img - the solved difference inverse problem eidors image
%                  object.
% (C) 2006, Camille Gomez-Laberge.
% $Id: get_model_params.m,v 1.6 2006/05/29 18:11:11 cgomez Exp $

% Debug variable
DEBUG = 1;
% Simulate movement
MOVE = 1;
% Scale standard alg images
STD_SCL = 0;
% Parameter used for movement artefact amplification
mm_scale = 100;

% Instantiate a homogeneous forward model (ref_level is 1)
sigma = ones( size(fwd_mesh.fwd_model.elems,1) ,1);

```

```

% Create the eidors_obj of type image.
fwd_img = eidors_obj('image', 'homogeneous image', ...
    'elem_data', sigma, ...
    'fwd_model', fwd_mesh.fwd_model,...
    'ref_level', 1);
vh = fwd_solve( fwd_img );

% Create a simulation object with single element contrast along 45 degree
fwd_elem_ctr = calc_element_centroid(fwd_img.fwd_model.elems, ...
    fwd_img.fwd_model.nodes);
f_ctr_dist = fwd_elem_ctr - 0.7071*rad_posn;
dist = zeros(length(f_ctr_dist),1);
for i=1:length(dist)
    dist(i) = norm(f_ctr_dist(i,:));
end
fwd_cntrst = find(dist == min(dist));
if length(fwd_cntrst) > 1
    fwd_cntrst = fwd_cntrst(1);
end

% Intensity of contrast
sigma(fwd_cntrst) = 0.01;
fwd_img.elem_data = sigma;

% Simulate node movements - shrink x, stretch y
% node0 before, node1 after movement
move = [];
movep = movep/100;
if MOVE
    movement = [1-movep 0; 0 1+movep]; % movement of 1%
    node0 = fwd_img.fwd_model.nodes;
    node1 = node0*movement;
    fwd_img.fwd_model.nodes = node1;
end

% Solve inhomogeneous forward problem
vi = fwd_solve(fwd_img);
if MOVE
    vi.meas = vi.meas;
    move = node1 - node0;
end
if DEBUG
    calc_colours('ref_level',1);
    figure;
    mysubplot(1,2,1);
    show_fem_move(fwd_img, move);
end

% Create a reconstruction image object.
inv_img = inv_solve(inv_mdl, vi, vh);
% If standard algorithm is used, try scaling the result to see better.
if ~strcmp(inv_mdl.fwd_model.jacobian,'aa_e_move_jacobian')*STD_SCL
    ed= inv_img.elem_data;
    lim= .08;
    ed = ed.*(abs(ed)<=lim) + lim*sign(ed).*(abs(ed)>lim);
    inv_img.elem_data= ed;
end
if DEBUG
    calc_colours('ref_level',0);
    mysubplot(1,2,2);
    show_fem_move(inv_img,[],mm_scale);
end

function [art_img, amplitude] = calc_artefact( fwd_img, inv_img, blur_elem )
% CALC_ARTEFACT Calculates the amplitude of artefact effects in the
% conductivity distribution of a reconstructed model.
% Args:      fwd_img - the forward problem as eidors_obj of type image
%            inv_img - the inverse problem as eidors_obj of type image
%            (blur_elem) - the indicies of elements in contrast blur area
% Returns:  art_img - the inverse image corresponding to artefacts only
%           amplitude - the total amplitude of the artefact conductivity

```

```

%                               elements.
% (C) 2006, Camille Gomez-Laberge.
% $Id: calc_artefact.m,v 1.5 2006/05/29 18:11:11 cgomez Exp $

% Debug variable
DEBUG = 0;
% Handle fewer argument calls.
if nargin < 3
    blur_elem = [];
end

% Define an eidors_obj image for artefacts only.
reference = fwd_img.ref_level;
% Determine whether inverse model has movement data.
n_inv_elem = size(inv_img.fwd_model.elems, 1);
if size(inv_img.elem_data, 1) > n_inv_elem
    inv_img.elem_data = inv_img.elem_data(1 : n_inv_elem);
end

% Create a mask vector so that only inhomogeneous elements are 1.
fmask = zeros(size(fwd_img.elem_data));
fmask(find(fwd_img.elem_data ~= reference)) = 1; %forward mesh mask

% Compare forward mesh with inverse mesh.
elem_map = compare_fem( fwd_img.fwd_model, inv_img.fwd_model );
% inverse mesh mask of true inhomogeneities
imask = zeros(n_inv_elem,1);
imask( elem_map( find(fmask) ) ) = 1;
if ~isempty(blur_elem)
    imask(blur_elem) = 1;
end

% Calculate artefact values of corresponding elements.
art_img = inv_img;
artefacts = ~imask.*inv_img.elem_data;
if DEBUG
    avg_val = mean(artefacts)
    artefacts(find(imask)) = avg_val;
end
art_img.elem_data = artefacts;
% Calculate area or volume of elements
e_space = calc_element_vol(inv_img);
% Calculate artefact signal power.
amplitude = sqrt(sum( e_space.*artefacts.^2 ) / sum( e_space ));

function [br, elem_idx] = meas_blur_radius(fwd_img, inv_img, fwd_cntrst)
% MEAS_BLUR_RADIUS Measures a resolution figure-of-merit called the
% blur radius from the single contrast element simulated eidors image
% objects FWD_IMG and INV_IMG solved by the algorithms to be analyzed.
% Args:      fwd_img - the simulated forward problem eidors image object.
%           inv_img - the solved difference inverse problem eidors image
%           object.
%           fwd_cntrst - the contrast element index.
% Returns:   br - the blur radius (see reference)
%           elem_idx - element indices that are part of the blurred area
%
% REFERENCE: A Adler, R Guardo, "Electrical Impedance Tomography:
% Regularized Imaging and Contrast Detection", IEEE Trans. Med. Imaging,
% vol 15(2), 1996.
% (C) 2006, Camille Gomez-Laberge.
% $Id: meas_blur_radius.m,v 1.3 2006/02/16 22:54:22 cgomez Exp $

% Calculate inverse element total area.
elem_area = calc_element_vol(inv_img);
area0 = sum(elem_area);

% Calculate the 1/2 image magnitude area.
i_elem_data = inv_img.elem_data(1:length(elem_area));;
elem_nodes = inv_img.fwd_model.elems;
pwr0_half = sum(abs(i_elem_data))/4;

```

```

elem_map = compare_fem(fwd_img.fwd_model, inv_img.fwd_model);
pwr_z = sum(abs(i_elem_data(elem_map(fwd_cntrst))));
elem_idx = elem_map(fwd_cntrst)';
while pwr_z < pwr0_half
    nhbrs = find_adjoin(elem_idx, elem_nodes');
    elem_idx = unique([elem_idx nhbrs]);
    pwr_z = sum(abs(i_elem_data(elem_idx)));
end
area_z = sum(elem_area(elem_idx));
% Calculate the blur radius.
br = sqrt(area_z/area0);

```

C.3 Artefact Analysis

```

% SecondOrderAnalysis script fits a second order system response parameters
% to a reconstructed contrast distribution.
% (C) 2006, Camille Gomez-Laberge
% $Id: SecondOrderAnalysis.m,v 1.3 2006/04/05 14:46:53 cgomez Exp $

% Set PLOT=1 to see fitted curves
PLOT = 1;
TREND = 0;
METHOD = 2;
% The reconstruction parameters used in the analysis
meshsize = {'a2c','b2c','c2c','d2c','e2c','f2c'};
priortype = {'laplace_image_prior', 'aa_calc_image_prior'};
hpvals = [1e-1, 1e-2, 1e-3, 1e-4, 1e-5, 1e-6, 1e-7, 1e-8];

% The collected second order response best-fit estimates
estimates = cell(1,length(priortype));
fiterror = estimates;

% Add eiders3d/ to Matlab path if not present.
test_eiders_path();
eiders_msg('log_level',0); % Keep eiders quiet
% Set eiders default colours
calc_colours('mapped_colour',128);
calc_colours('backgnd',[.9,.9,.9]);
calc_colours('ref_level',0);

% Generate eiders planar finite forward and inverse meshes.
fwd_mesh = mk_common_model(meshsize{6});
inv_mdl = mk_common_model(meshsize{5});

% Set regularization prior, jacobian and hyperparameter
inv_mdl.fwd_model.jacobian = 'aa_calc_jacobian';
for prior = 1 : length(priortype)
    inv_mdl.RtR_prior = priortype{prior};
    cumulest = [];
    cumulerr = [];
    for hp = 1 : length(hpvals)
        inv_mdl.hyperparameter.value = hpvals(hp);

        % Get simulation model parameters for-loop
        [f_img, fe_ctr, fe_con, i_img] = ...
            get_model_params(fwd_mesh, inv_mdl, 0, 0);

        % Convert inverse solution into pixel image data
        pi_img = cell2mat(show_slices(i_img));
        pi_img(isnan(pi_img))=0;

        % METHOD 1: Slice image along x-axis and model Edge Spread Function
        if METHOD == 1
            % Calculate image coordinates
            pi_yctr = floor(size(pi_img,1)/2);
            pi_xctr = floor(size(pi_img,2)/2);
            pi_xmax = size(pi_img,2) - 1;
            xdata = [0:pi_xctr-1];

```

```

% Sample data reflected along x-axis and normalized
pi_data = -pi_img(pi_yctr, pi_xctr:pi_xmax);
pi_data = pi_data/max(pi_data);

% Find edge of step input
input = max(find(pi_data > 0.95));

% Fit image data to a second order response curve for
% underdamped systems
[epara, model] = fitmodeltodata([0:pi_xctr-input],...
    pi_data(input:pi_xctr), [0.20, 0.4]);

% Store estimated parameters
cumulest = [cumulest; epara];
[error_val, model_curve] = model(epara);
cumulerr = [cumulerr; error_val];

% Plot results
if PLOT
    figure;
    plot(xdata, pi_data); hold on;
    plot(xdata, [ones(1,input-1) model_curve], 'r');
    title({strcat('RtR\prior: ', priortype{prior});...
        strcat('\lambda = ', num2str(hpvals(hp)))});
end

elseif METHOD == 2
% Collect all pixel data
[px,py] = meshgrid(linspace(-1,1,size(pi_img,1)),...
    linspace(-1,1,size(pi_img,2)));

% Convert data coords from rect to polar and build unit radius
% axis
[ptheta, prho] = cart2pol(px, py);
pr = unique(prho);
prmax_index = find(pr > 1,1);
pr = pr(1:prmax_index);
rlen = length(pr);

% Sum data as a function of radius
pr_data = zeros(rlen,1);
plen = length(pi_img);
for i = 1:rlen
    ind = find(prho == pr(i));
    pr_data(i) = trace( pi_img( mod(ind,plen)+1,...
        ceil(ind/plen)))/length(ind);
end
pr_data = pr_data./min(pr_data);

% Fit image data to a second order response curve for underdamp
% system. Unlike METHOD 1, we model a Point Spread Function
[epara, model] = fitmodeltodata(pr, pr_data, [0.40, 25, 0.1]);
[error_val, model_curve, xshift] = model(epara);
% Second level or parameter fitting

% Store estimated parameters
cumulest = [cumulest; epara];
cumulerr = [cumulerr; error_val];
xratio = rlen/65;
curve_shift = floor(xshift/xratio);
curve_x = [0:1/64:1];
epara(2)./xratio;
model_curve = underdamp(curve_x, epara);
if curve_shift > 0
    model_curve = [ones(1,curve_shift) ...
        model_curve(1:65-curve_shift)];
else
    model_curve = [model_curve(-curve_shift+1:65)...
        zeros(1,-curve_shift)];
end
% Plot results

```

```

    if PLOT
        figure;
        plot(pr, pr_data); hold on;
        plot(curve_x, model_curve, 'r');
        title({strcat('RtR\_prior: ', priortype{prior});...
                strcat('\lambda = ', num2str(hpvals(hp)))});
    end
else
    % Collect all pixel data
    [px,py] = meshgrid(linspace(-1,1,size(pi_img,1)),...
        linspace(-1,1,size(pi_img,2)));

    % Convert data coords from rect to polar and build unit radius
    % axis
    [ptheta, prho] = cart2pol(px, py);
    pr = unique(prho);
    prmax_index = find(pr > 1,1);
    pr = pr(1:prmax_index);
    rlen = length(pr);

    % Sum data as a function of radius
    pr_data = zeros(rlen,1);
    plen = length(pi_img);
    for i = 1:rlen
        ind = find(prho == pr(i));
        pr_data(i) = trace( pi_img( mod(ind,plen)+1,...
            ceil(ind/plen)))./length(ind);
    end
    pr_data = pr_data./min(pr_data);

    % sample data points
    pr_data = pr_data(1:20:length(pr_data));
    pr = pr(1:20:length(pr));

    % Fit image data to a second order response curve for underdamp
    % system.
    [epara, model] = fitmodeltodata(pr, pr_data, [0.40, 25]);
    cumulest = [cumulest; epara];
    [error_val, model_curve, xshift] = model(epara);
    cumulerr = [cumulerr; error_val];

    % Plot results
    if PLOT
        figure;
        plot(pr, pr_data); hold on;
        plot(pr, model_curve, 'r');
        title({strcat('RtR\_prior: ', priortype{prior});...
                strcat('\lambda = ', num2str(hpvals(hp)))});
    end
end % End METHOD loop
end % End hpvals loop
estimates{1,prior} = cumulest;
fiterror{1,prior} = cumulerr;
% Plot parameter values versus the hyperparameter
if TREND
    figure;
    semilogx(hpvals,cumulest(:,1),'--rs','LineWidth',2,...
        'MarkerEdgeColor','k',...
        'MarkerFaceColor','g',...
        'MarkerSize',10);
    grid on;
    hold on;
    semilogx(hpvals,cumulest(:,2)./xratio,'--bs','LineWidth',2,...
        'MarkerEdgeColor','k',...
        'MarkerFaceColor','g',...
        'MarkerSize',10);
    title({'Second order parameters VS \lambda';...
        strcat('RtR\_prior: ', priortype{prior})});
    legend('damping ratio \zeta','natural freq. \omega_n');
    xlabel('Hyperparameter log(\lambda)');
end

```

```

end % prior loop

function [mpara, mcurve] = fitmodeltodata(x, data, init)
% FITMODELTDATA fits a second order response model to data given.
% Args:      x - the length of the curve along x-axis
%            data - the data to fit response to
%            init - initial values of parameters
% Returns:   mpara - parameters for fitted model
%            mcurve - the fitted model curve
% (C) 2006, Camille Gomez-Laberge.
% $Id: fitmodeltodata.m,v 1.3 2006/04/05 14:46:54 cgomez Exp $

mcurve = @second_order;
mpara = fminsearch(@second_order, init);
function [fiterror, y, xshift] = second_order(para)
% SECOND_ORDER plots the response curve of a second order system with
% step input.
% para(1) - eta damping ratio
% para(2) - nf natural frequency
% para(3) - x-shift

y = underdamp(x,para);
% ***** THIS BLOCK USED FOR METHOD 2 ONLY *****
[ymin, yindex] = min(y);
[datamin, dataindex] = min(data);
xshift = dataindex - yindex;
if xshift >= 0
    y = [ones(xshift,1); y(1:length(y)-xshift)];
else
    y = [y(-xshift+1:length(y)); zeros(-xshift,1)];
% fprintf('WARNING: X-SHIFT WAS NEGATIVE: %d\n',xshift);
end
% ***** THIS BLOCK USED FOR METHOD 2 ONLY *****

fiterror = norm(x.^2.*(data-y),1);
end % End of second_order subfunction
end % End of fitmodeltodata function

function y = underdamp(x,params)
% SECOND_ORDER plots the response curve of a second order system with step
% input.
% params(1) - eta damping ratio
% params(2) - nf natural frequency
% params(3) - x-shift
eta = params(1);
nf = params(2);
xshift = params(3);
s_eta = sqrt(1-eta^2);
y = exp(-eta*nf*(x-xshift))/s_eta.*sin(s_eta*nf*(x-xshift) + asin(s_eta));
y = x.^(0.333).*y;
end

```